Abstract

Title of Thesis: Pressure-Temperature-time-Deformation (P-T-t-D) History of High-Grade Gneisses of the Port aux Basques Area, Southwest Newfoundland, Canada

Jerry Lee Burgess, Master of Science, 1994

Thesis directed by: Dr. Michael Brown
Professor
Department of Geology

A polyphase deformation history (D_1-D_4) and upper amphibolite facies metamorphism characterize the Port aux Basques Gneisses. Late-D_1 to early-D_2 kyanite porphyroblasts and early- to syn-D_2 staurolite and garnet porphyroblasts each contain inclusion trails that preserve S_1. Reaction out of muscovite, staurolite and kyanite in favor of sillimanite + garnet + alkali feldspar-bearing assemblages in the metapelitic gneisses record syn- to late- D_2 peak metamorphic conditions. Isograd surfaces related to syn-D_2 metamorphism were probably subhorizontal to inclined but now their map pattern reflects subsequent deformation by D_3. Fluid-present melting initiated in the kyanite zone and continued into the sillimanite zone. Metamorphic conditions increase to the southeast with 'peak' temperatures of *c.* 700-750°C at 8-9 kbar associated with the D_2/M_2 thermal regime.

A Pb^{207}/Pb^{206} date of *c.* 417 Ma was obtained from titanite in high-grade rocks of the Harbour le Cou Group. This date provides a minimum constraint for the M_2 event. Hornblende from a nearby amphibolite yields an $^{40}Ar/^{39}Ar$ isotope correlation date of c. 419

Ma. Muscovite at the same locality records a $^{40}Ar/^{39}Ar$ plateau date of 391 Ma. Hornblende and muscovite separates from rocks of the Port aux Basques Complex yield similar $^{40}Ar/^{39}Ar$ dates. Calculations indicate that post- D_3 cooling rates of approximately 8-1°C/Ma are required for the area. The kyanite to sillimanite transition and D_2 structures suggest a clockwise trajectory in P-T space as a result of Silurian orogenesis.

PRESSURE-TEMPERATURE-TIME-DEFORMATION (P-T-t-D) HISTORY OF HIGH-GRADE GNEISSES OF THE PORT AUX BASQUES AREA, SOUTHWEST NEWFOUNDLAND, CANADA

by

Jerry Lee Burgess

Thesis submitted to the Faculty of the Graduate School
of The University of Maryland in partial fulfillment
of the requirements for the degree of
Master of Science
1994

Advisory Committee:

Professor Michael Brown, Chairman/Advisor
Associate Professor Eileen McLellan
Adjunct Professor E-an Zen
Dr. Cees R. van Staal

ACKNOWLEDGMENTS

The following people have earned my respect and appreciation for their invaluable assistance in this endeavor:

Mike Brown
Jan Burgess
Dave Dallmeyer
Benoit Dubé
Lindsay Hall
Eddie Hull
Eirik Krogstad
Barry Lumpkin
Eileen McLellan
Phil Piccoli
Paul Tomascak
Skip Stoddard
Cees van Staal
John Winchester
E-an Zen
Rangers of Cheeseman Provincial Park
Folks from the town of Port aux Basques, Newfoundland.

Table of Contents

List of Tables

List of Figures

List of Photographs

Introduction

Preamble

In recent years, the burial and subsequent uplift of regional metamorphic terranes has been evaluated in terms of pressure-temperature-time (P-T-t) paths. These models for the metamorphic evolution of regions reflect the perturbation and subsequent thermal relaxation of the crustal geotherm during orogenesis. It is widely recognized that these perturbations result from either of two endmember processes: compressional thickening or lithospheric thinning. These endmember processes for orogenic belts can be characterized by clockwise P-T-t paths and counterclockwise P-T-t paths, respectively (e.g. Brown, M., 1993). In orogens characterized by clockwise P-T-t path, at least some deformation, in particular that related to thickening, precedes the metamorphic peak; whereas in orogenic belts characterized by counterclockwise P-T-t paths the bulk of the deformation commonly postdates the metamorphic peak. Even within this first order division of orogenic belts there are important distinctions to be made; for example, the different relations between deformation and mineral growth resulting from frontal *vs.* basal accretion in metamorphic thrust belts that generate clockwise P-T-t paths (van Gool and Cawood, 1994). Detailed characterization of orogenic belts through utilization of a variety of disciplines is vital to further progress in understanding the processes of orogenesis.

Goals of this Study

This thesis presents results of an integrated field, petrologic

and geochronologic study of the Port aux Basques Gneisses of southwest Newfoundland. This study is important because: 1) It will significantly increase knowledge of the Paleozoic orogenic processes involved in the tectonothermal evolution of the Central Mobile Belt in southwestern Newfoundland and in the Appalachians as a whole, 2) is the first such detailed approach for the Port aux Basques Gneisses, an area where metamorphic processes are poorly understood, and 3) It will provide information on spatial and timing relationships between tectonic blocks in an area of dynamic crustal evolution.

The structure of this thesis is built upon the idea that each concept or data set will lead toward another to finally come to some conclusions concerning the P-T-t-D history of these rocks. The first section of the thesis (Chapter 1) will present a basic tectonic framework which will be expanded upon in the regional implications section of Chapter 4. Chapter 2 will describe the appearance and basic mineralogy of the principal rock types found within the study area. These rock descriptions will be augmented by thin section petrography and phase assemblages in Chapter 3. Chapter 3 will provide a discussion concerning the metamorphic history of these rocks using porphyroblast/matrix relationships. Textures, mineral chemistry and phase assemblages will be used to decipher reactions among phases and provide qualitative and quantitative estimates concerning thermal and baric conditions during metamorphism. Chapter 4 will build upon the preceding two chapters by incorporating geochronologic data and finally by placing the Port aux Basques Gneisses within a regional context.

More detailed information on numbered samples mentioned in the body of this text are found in Appendix 3 with a brief sample description and any structural data obtained at that location. For reference, these samples have been plotted on a map contained in Appendix 2. All photographs are in Appendix 1.

Tectonic Framework

The Appalachian - Caledonian orogenic belt preserves the record of the evolution and destruction of the Early Paleozoic Iapetus Ocean and the collision of the ancient continents including Laurentia, Gondwana and Baltica (Soper and Hutton, 1984; Soper and Woodcock, 1990). Our understanding of the geologic history of the Northern Appalachians continues to evolve as new concepts, approaches and methods of analysis are applied. The long-established threefold division of Paleozoic orogenic episodes into the Ordovician Taconian event, the Devonian Acadian event and the Pennsylvanian-Permian Alleghanian event has become too restrictive given the availability of high-precision age dating of plutonic and thermal events. Classical interpretations of these three orogenic events led to the idea that they were temporally as well as geographically distinct. However, recent investigations have shown that previously unrecognized Silurian events are of major importance throughout much of the Northern Appalachians (Dunning et al., 1990a, b; van Staal and Fyffe, 1991; Sevigny and Hanson, 1993 and Greennough et al., 1993; van Staal, 1994; Cawood et al., 1994). This Silurian imprint appears to be present in much of southern Newfoundland.

Southwest Newfoundland, like much of the Canadian Appalachians, is divisible into a number of tectono-stratigraphic

zones. Once erected in a provincial area, extrapolation of these zones away from that local area enables the rocks to fit into a larger context. Understanding of how a tectono-stratigraphic zone correlates (or does not correlate) across strike allows a geometry to be established. These geometries can play an important role in understanding the tectonic framework of orogenic belts. For example, the Dunnage Zone wedges out across Newfoundland because of the southwestward convergence of the Humber and Gander Zones (Williams, 1979; Williams et al., 1988) (Fig. 1). In southwestern Newfoundland remnants of the Notre Dame arc or western part of the Dunnage Zone (Williams et al., 1988; van Staal, 1994) begin to converge with rocks of Avalonian or Gondwanan affinity to the east exposing a middle-crustal orogenic belt represented by the Port aux Basques Gneisses (Brown, 1973, 1976, 1977) (Fig. 1, 2). Thus, the Port aux Basques Gneisses comprise a part of the Central Mobile Belt (Dunnage Zone + Gander Zone). Separation of Gander Zone rocks, which represent the Paleozoic cover on the Avalon Zone basement, from rocks of the arc and back-arc eastern Dunnage Zone (Exploits Subzone), (van Staal and Williams, 1991; van Staal, 1994), unrelated to the western Dunnage Zone (Williams et al., 1988), has been difficult in this area because of the masking effects imposed by the intense deformation and metamorphism. Dunning et al. (1990a) report that rocks of the Central Mobile Belt that are exposed in southwest Newfoundland and on Cape Breton Island have undergone a strong Silurian syncollisional deformation and metamorphism which is uncharacteristically stronger than in other parts of the orogen. For instance, Silurian metamorphism rarely preserves

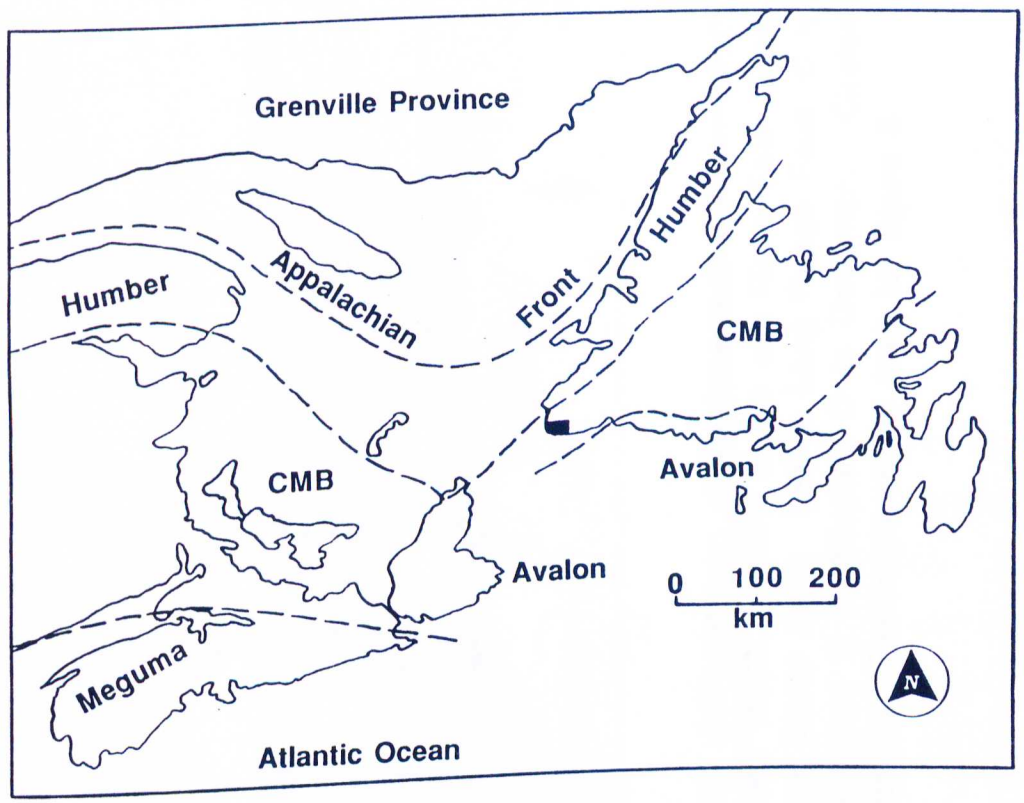

Figure 1. Northern Appalachian Area Map modified after Barr and Jamieson (1991). Humber, Meguma, CMB and Avalon each refer to zones or terranes which are fault bounded and belong to the same tectonostratigraphic grouping. CMB stands for Central Mobile Belt which is a composite of Gander and Dunnage zone rocks. Shaded area referred to in figure 2.

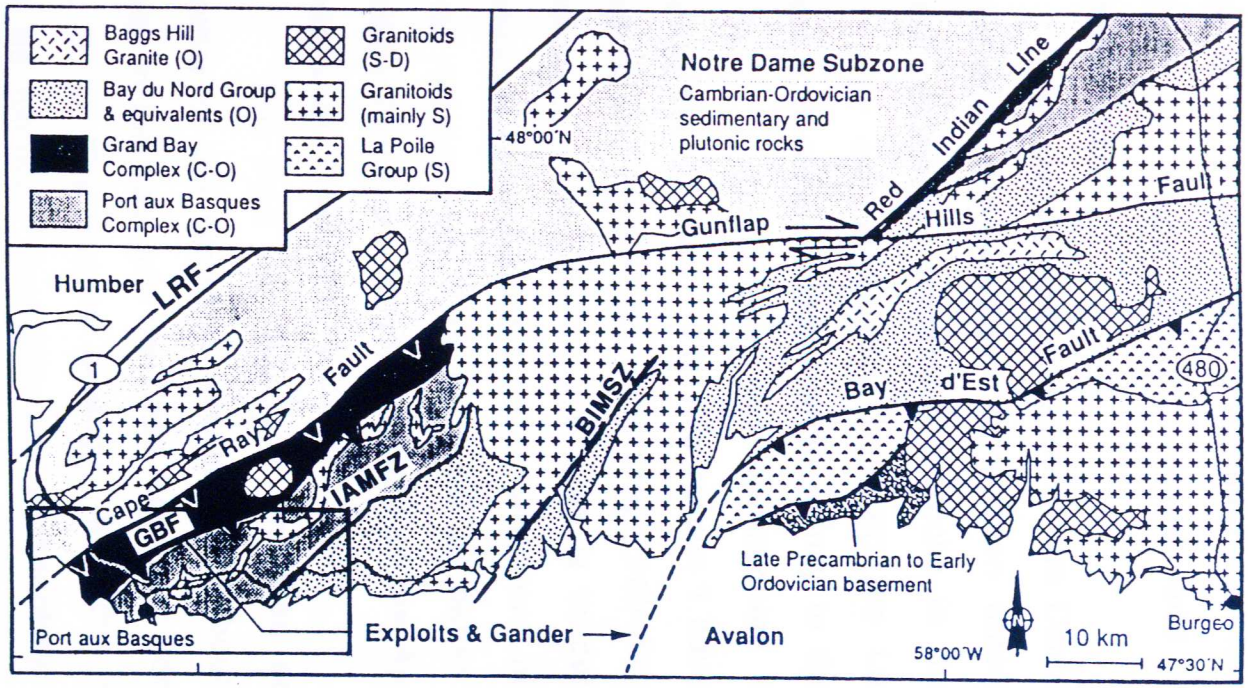

Figure 2. Generalized geologic map of southwestern Newfoundland; modified from Lin et al., 1994b. IAMFZ is Isle aux Morts Fault Zone; BIMSS is Bay le Moine Shear Zone; LRF is Long Range Fault; Є is Cambrian; O is Ordovician; S is Silurian; D is Devonian. Circled numbers indicate highways. Rectangle shows area for figure 3.

pressures over 5 kbar (van Staal and Lin, 1994). However, Plint and Jamieson (1989) record temperatures of ≈ 700-750°C at 8-10 kbar for metapelites on Cape Breton Island. Further, Lin et al. (1994) and Barr et al. (1992) have suggested correlations between these same rocks on Cape Breton Island and those of southwestern Newfoundland.

The schists and gneisses of the Central Mobile Belt exposed in southwest Newfoundland have been among the least studied and least understood metamorphic rocks in the Northern Appalachians, yet their central location between the Laurentian terranes to the west and rocks of Gondwanan affinity to the east makes them a key area in understanding the Appalachian tectono-thermal evolution during the Silurian. For this reason I have undertaken an integrated approach involving structure, petrology, geochronology and tectonics. The goal of this work is to determine a well-constrained pressure-temperature-time-deformation history for these rocks. This history can then be used to better understand the early to middle Paleozoic orogenic history of the Appalachian Orogen.

Regional Geologic Setting

The Port aux Basques Gneisses occur in the southwestern corner of the island of Newfoundland, bounded by the Bay le Moine fault in the east and the Cape Ray Fault Zone (CRFZ) in the west (Fig. 2, 3, 4). The general geology, from the northwest to the southeast, is as follows. Carboniferous sedimentary rocks are exposed in the Codroy Valley to the northwest of the Long Range Fault (LRF). The CRFZ lies south of the LRF. The LRF separates rocks of the Humber Zone from those of the western Dunnage Zone (Brown, 1977). The

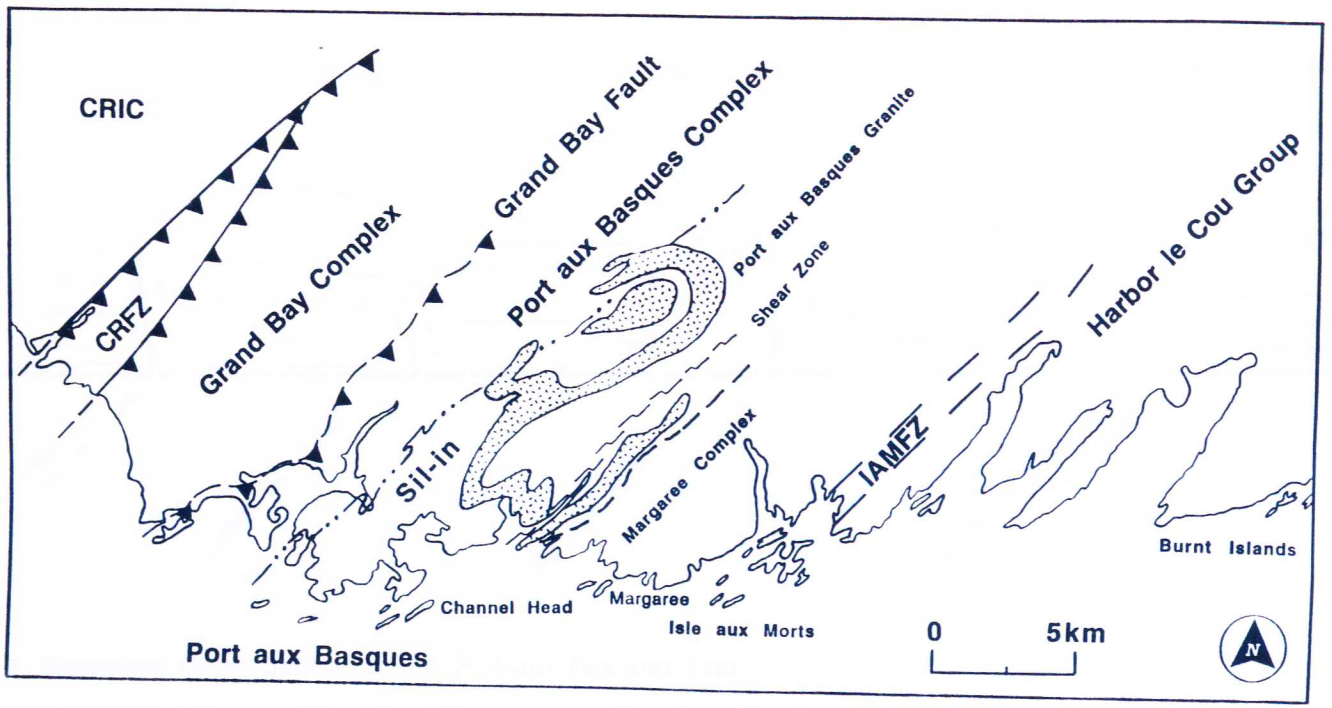

Figure 3. Local geologic map of the Port aux Basques are. Stippled unit is the Port aux Basques Granite. CRFZ is Cape Ray Fault Zone; IAMFZ is Isle aux Morts Fault Zone;CRIC is Cape Ray Igneous Complex; dashed line represents the Margaree Complex-PaBC boundary; the dash-dot-dot line is the Sillimanite-in (Sil-in) isograd.

Schematic Cross Section of the Port aux Basques Gneisses and Associated Areas

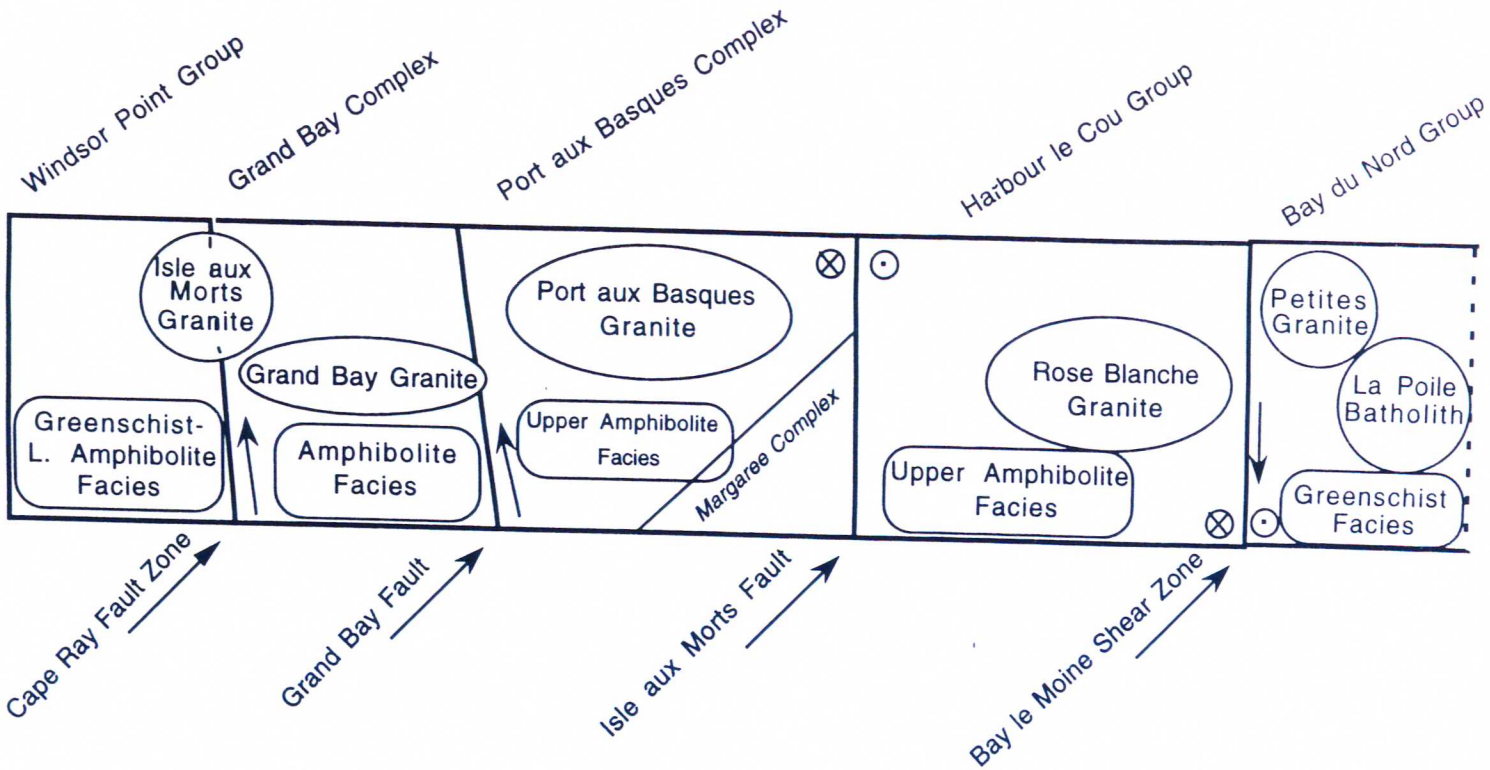

Figure 4. Schematic Cross Section of the Port aux Basques Area.

CRFZ separates two contrasting geologic domains and forms the northern boundary of the Hermitage Flexure (Williams, 1970: O'Brien et al., 1986). Northwest of the CRFZ lies the Cape Ray Igneous Complex (CRIC), which consists of variably deformed Ordovician and Silurian granitoid plutons (Dubé and Lauzière, 1993) and associated remnants of the ophiolitic Long Range Mafic-Ultramafic Complex (Brown, 1976, 1977; Wilton, 1983; Hall et al., 1994). The CRFZ stretches over *c.* 2 km at the coast and comprises a steeply-southeast-dipping mylonite zone, < 1 km wide, which extends along the northwestern margin of both the Port aux Basques Gneisses and > 1 km width into the Ordovician to Devonian volcanic and sedimentary rocks of the Windsor Point Group (WPG) (Dubé et al., 1991, 1993), which extends along the margin of the CRIC.

The Port aux Basques Gneisses have been subdivided into four main lithostratigraphic units (van Staal et al., 1992a,b; Lin et al., 1993) (Fig. 3). The most western of these units is the Grand Bay Complex (GBC) which consists of highly strained and metamorphosed thin sequence of shale-siltstone rhythmites and feldspathic sandstones in the amphibolite facies. These metasedimentary rocks are interlayered with abundant amphibolite and granite. To the east, the GBC is in fault contact with medium- to high-grade metamorphosed variably argillaceous sediments and sandstones. These metapelitic gneisses, metasemipelitic gneisses and quartzites comprise the Port aux Basques Complex (PaBC). The boundary between the GBC and the PaBC is the Grand Bay Fault (GBF), a steeply-southeast-dipping, dominantly reverse movement shear zone intruded by granitic sheets that are now mylonitic with steep

southeast plunging stretching lineations (van Staal et al., 1992b). The PaBC is dominated by a pervasive association between gneisses and amphibolites, the latter may comprise up to 40% of a given outcrop as deformed dikes and sills. Protoliths of the PaBC paragneisses change in composition eastwards from quartz arenites to more feldspathic sandstones, whereas true pelitic compositions become less common and are replaced by semipelitic compositions. Together the sedimentary and intrusive rocks were metamorphosed at upper-amphibolite facies conditions to be discussed in chapter 3. In the southeastern corner of the PaBC, bounded by the Atlantic Ocean to the south, lies the Margaree Complex (MC), a collection of dominantly migmatitic gneisses with metamorphosed ultramafic pods. These migmatitic gneisses occur in two main localities. The type locality is near the villages of Margaree and Fox Roost, the other lies just southwest of Port aux Basques where it is exposed on the island of Channel Head. The northwestern boundary of the MC is intrusive (see Fig. 3 & van Stall et al., 1992b).

The PaBC is separated from the Harbour Le Cou Group (HlCG) to the east by the Isle aux Morts Fault Zone (IAMFZ), which is a now nearly vertical shear zone with a dominantly transcurrent movement history (van Staal et al., 1992a). The HlCG is composed of a monotonous sequence of deformed and metamorphosed paragneisses whose protoliths were likely feldspathic sandstones and siltstones, with occasional shale-siltstone rhythmites (van Staal et al., 1992a; Lin et al., 1993). Amphibolite and granite form a minor constituent of the HlCG. Calc-silicate pods are abundant in the thicker metasandstone units and amphibolites. The Bay le Moine

Fault, which exhibits dominantly dextral displacement, separates the HICG from similar rocks of the Bay du Nord Group to the east. The Bay du Nord Group is interpreted to represent the low grade equivalent of the HICG (Lin et al. 1993). A schematic cross-section which graphically depicts the basic geometric relationship between these divisions is given in figure 4.

Deformational History

All of the divisions share a common polyphase deformational history associated with a progressive medium to high grade metamorphic event (van Staal et al., 1992a,b). The metamorphic evolution of the area can best be described by reference to the deformational sequence, using the deformation as a relative time marker, even though the deformation may likely have been diachronous over large areas (e.g. Patterson and Tobisch, 1992). The regional deformation can be explained in terms of three main phases of penetrative deformation (D_1-D_3) and one minor phase (D_4) (see van Staal et al., 1992a, 1992b). The fourth phase of deformation (D_4) is locally present near major shear zones. Much of the structural interpretation is taken from the work of van Staal et al., 1992a,b and Lin et al., 1993. However, larger scale D_3 structures in the Port aux Basques area were examined as part of this work, in conjunction with regional field mapping by van Staal et al., 1992b. For this study, structural data obtained at numbered sample locations are included with sample descriptions in Appendix 3. Additional data is presented in stereographic projections and in figure 7.

The first period of deformation (D_1) has been largely

obliterated by later folding events, but is best preserved in low strain areas such as the hinge areas of F_2 folds or in numerous fold interference patterns produced as a result of superposition of F_2 folds on F_1 folds. The most common interference patterns are Ramsay (1967) type 2 and type 3 patterns (Photograph 1a). F_1 folds are tight to isoclinal and have strongly differentiated axial planar layering (S_1) defined by micas and hornblende. Where seen, rare S_1 is parallel to S_0 in all units which may suggest large scale D_1 nappe structures throughout the area (van Staal et al., 1992b).

S_2 is the dominant planar fabric in the area (Photograph 1b, 1c). S_1 fabrics have been overprinted by tight to isoclinal F_2 folds producing either a differentiated crenulation cleavage, or a fully developed penetrative schistosity as a result of advanced transposition of S_1. The S_2 fabric dips consistently to the southeast at moderate to steep angles (Photograph 1c,f and Fig. 5). F_2 folds are generally reclined and in areas where later deformational events are weakly developed, F_2 folds are recumbent with shallowly dipping axial planes. Van Staal et al. (1992b) state that F_2 folds are demonstrably sheath folds and the F_2 hinge lines are commonly parallel to the L_2 stretching lineation indicating a structural regime characterized by overthrusting. Further, they state that the D_1-D_2 deformational events are thought to be part of a progressive sequence. The metamorphic history discussed in Chapter 3 should be reflective of this and indicate a progressive metamorphic event. As seen in figure 6 the parallelism of F_2 and L_2 is indeed the case in the

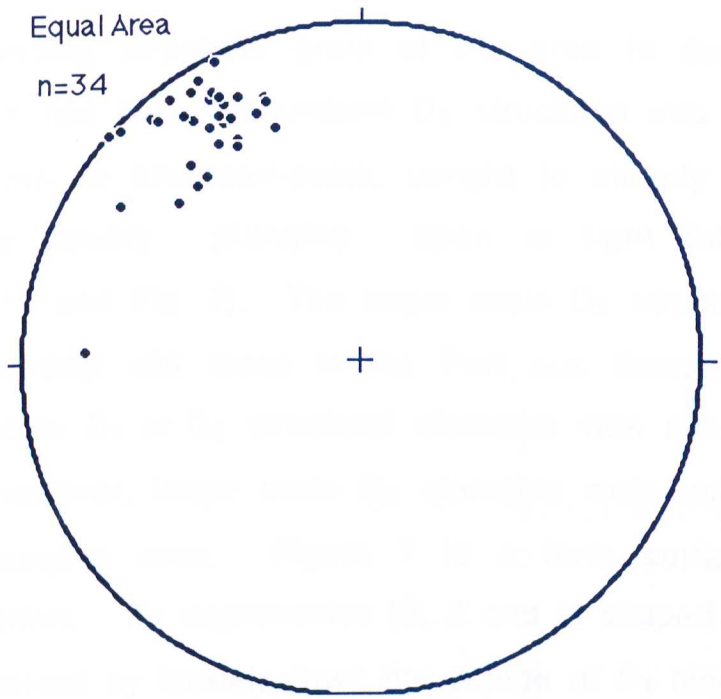

Figure 5. Stereographic projection showing poles to the S2 fabric. The S2 fabric consistently strikes to the northeast and dips steeply to the southeast.

Port aux Basques area where F_2 hinge lines generally have steep plunges and are often parallel to a mineral lineation. Larger scale D_2 structures could not be deciphered due to the intensity of later deformation.

The NE-trending structural grain of the area is due to D_3 deformation, which has folded recumbent D_2 structures into a series of large decameter- to kilometer-scale, upright to steeply inclined, commonly gently doubly plunging open to tight folds (F_3) (Photograph 1a, 1b and Fig. 7). The larger scale D_3 structures are easily seen in vertical cliff faces in the Port aux Basques area. Mapping large scale D_1 or D_2 structural elements was not feasible for this study. However, larger scale D_3 elements were mapped in the Port aux Basques area. Figure 7 is a form surface map illustrating this effort. F_3 asymmetries (S, Z and M shaped parasitic folds) were determined by looking down the plunge of F_3 hinge lines. All asymmetries and structural measurements plotted on figure 7 are in their actual locations. The intensity of D_3 varies throughout the area. In zones where D_3 is less pronounced, chevron type folds deform S_2 without the development of a penetrative S_3 foliation (Photograph 1a). In other areas, particularly where D_3 structures are more pronounced, F_2 and F_3 folds cannot be separated on the basis of style alone and F_3 is accompanied by a weak to strongly developed S_3 crenulation cleavage which is axial planar. The plunge of F_3 hinge lines varies from shallow to moderate, but are more commonly shallow, 10-20°, doubly plunging to the northeast or

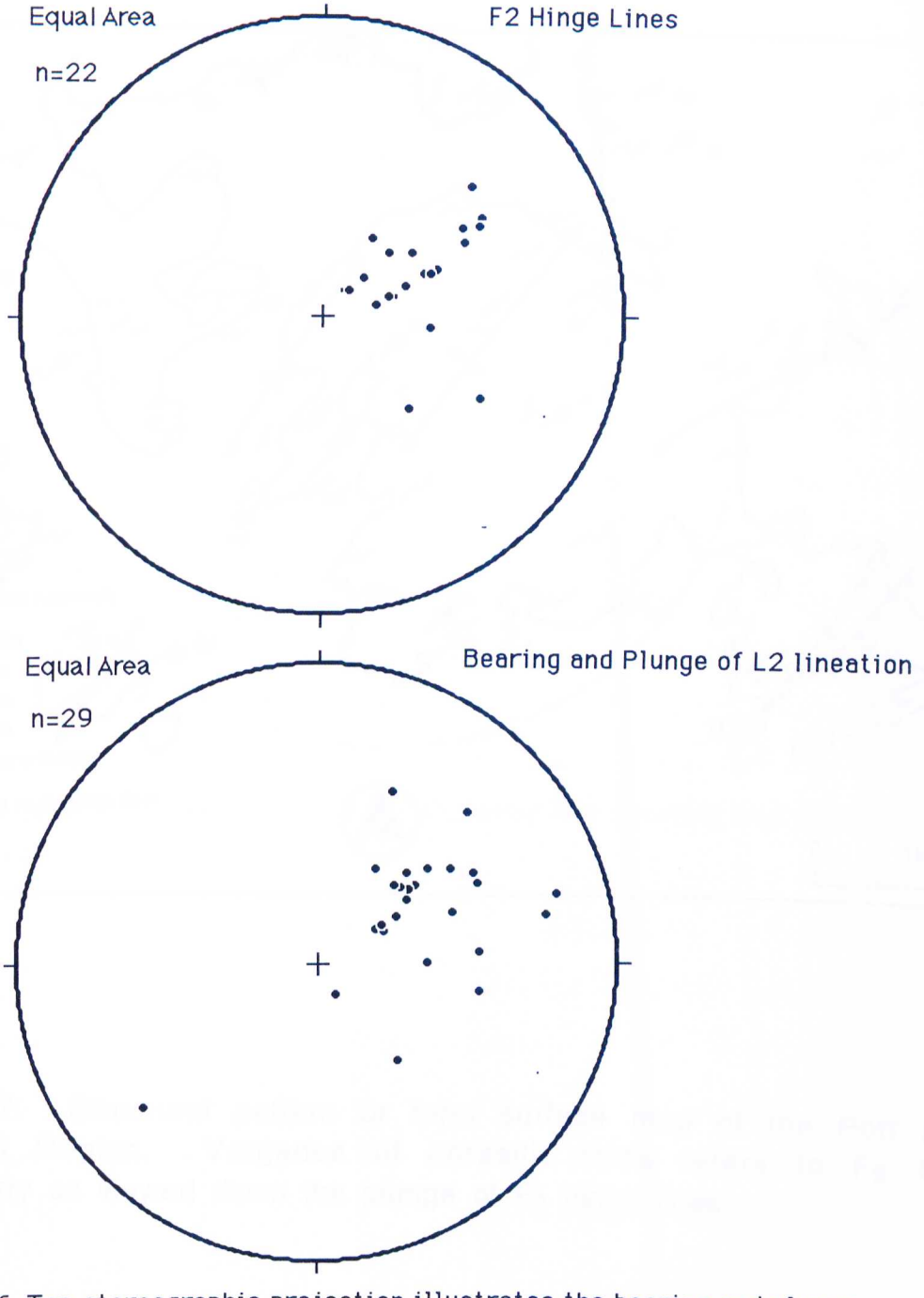

Figure 6. Top stereographic projection illustrates the bearing and plunge of F2 hinge lines, while the lower projection shows the bearing and plunge of the L2 mineral lineation. Note the similar orientation of the linear features.

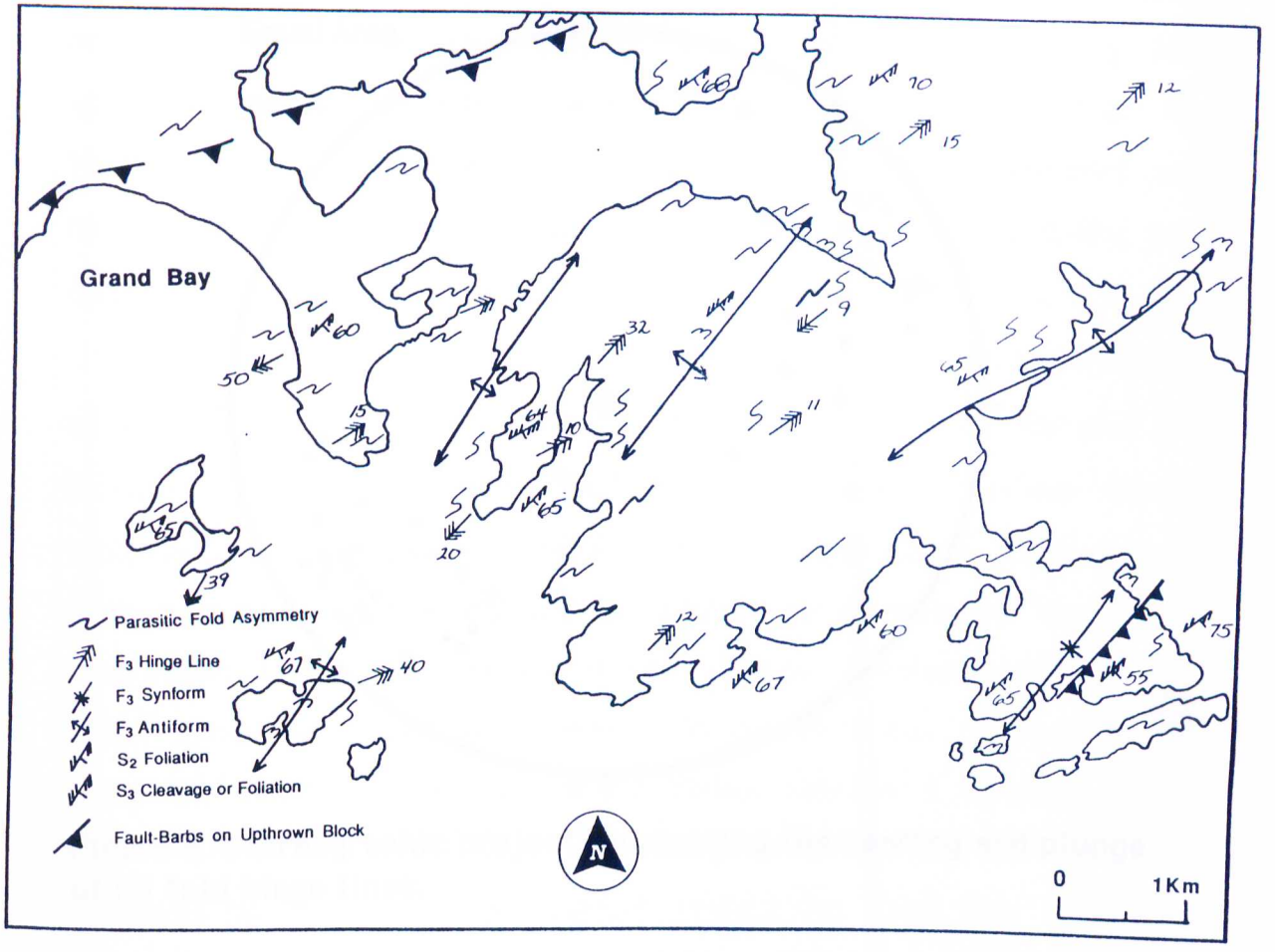

Figure 7. Structural pattern or form surface map of the Port aux Basques Region. Vergence of parasitic folds refers to F_3 fold asymmetry as viewed down the plunge of F_3 hinge lines.

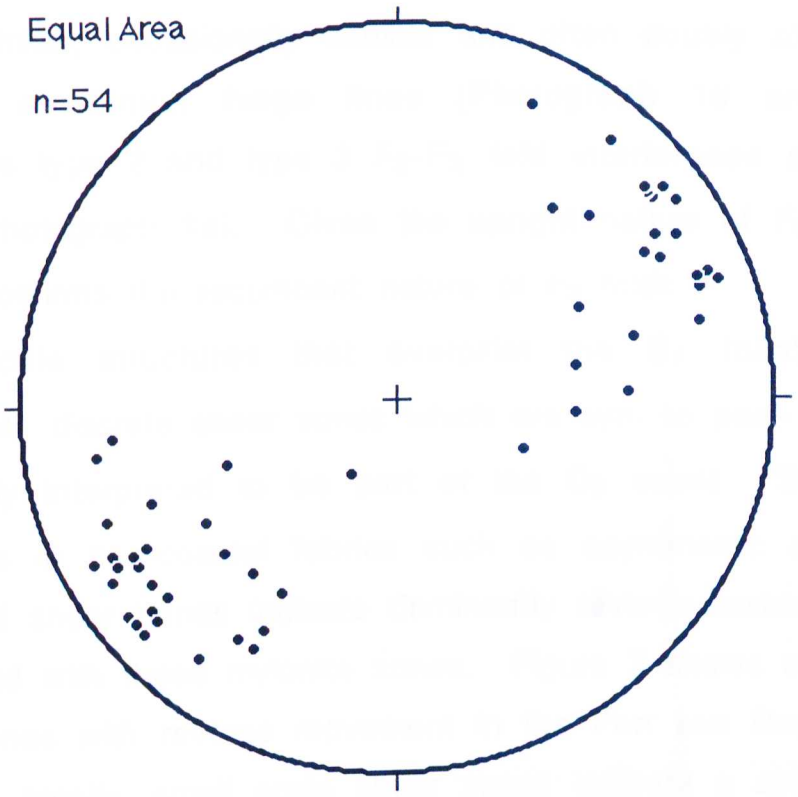

Figure 8. Stereographic projection showing the bearing and plunge of F3 fold hinge lines.

southwest (Fig 5, 6). In zones of penetrative D_3, F_3 folds are highly noncylindrical, occasionally conical and often doubly plunging with strongly curvilinear hinge lines (Photograph 1d and Fig. 8). Numerous type 2 and type 3 F_2-F_3 fold interference patterns are found (Photograph 1e). Given the upright nature of F_3 folds, this further confirms the recumbent nature of F_2 folds.

Ductile structures that overprint the S_2 foliation mainly consist of discrete shear zones which are syn- to post- D_2 and are tentatively interpreted to be part of the D_3 event. Shear sense indicators in non-coaxial fabrics such as asymmetric augen, drag folds and shear bands indicate dominantly reverse-dextral movement associated with these mylonite zones. Figure 7 shows one of these shear zones with reverse movement in the Port aux Basques area. However, locally, small scale shear zones indicate a sinistral sense of motion (Photograph 2a). Shearing in the Port aux Basques Gneisses becomes more pronounced toward the Cape Ray Fault and within the structurally lower WPG. Kinematic indicators in mylonitic rocks of the WPG reveal reverse-sinistral overthrusting, followed by reverse-dextral overthrusting (Dubé and Lauziere, 1993). Movement along the Isle aux Morts Fault and Bay le Moine Fault Zones display dominantly dextral transcurrent movement (Piasecki, 1991; Lin et al., 1993). F_3 fold asymmetries viewed down plunge are always 'Z' shaped in these two shear zone areas, probably as a result of dextral movement along the shear zones (Lin et al., 1993). However, in areas away from shear zones and in areas where a large three dimensional view of the outcrop is possible it can be

seen that small scale fold asymmetries accurately depict the larger scale structures. On the basis of shear zone kinematics and F_3 fold systematics, D_3 is interpreted to be the result of a regional transpressive deformational event (van Staal et al., 1992b; 1994).

A fourth deformation (D_4) is present in the Port aux Basques gneisses, but is localized, generally in areas near major shear zones. This event is generally characterized by large, open folds present in the Grand Bay Complex. Minor kink folding is also seen in the gneisses. Neither the large F_4 open folds or the smaller scale F_4 kink folds have an associated fabric. The kinematic implications of these folds are unknown but are almost certainly related to later movement along the Cape Ray Fault and Grand Bay Fault Zones.

Chapter Summary

The above discussion outlined the tectonic framework and regional geology surrounding the Port aux Basques Gneisses. It briefly reviewed the lithologic distinctions that were used to divide the Port aux Basques Gneisses into four distinct lithologic divisions each bound by major shear zones. These four divisions are: the Grand Bay Complex, the Port aux Basques Complex, the Margaree Complex and the Harbour le Cou Group. Structural evidence gathered during the process of this metamorphic study and by other co-workers reveal a deformational sequence consisting of four events (D_1-D_4). Structural analysis has shown that the structural histories are similar for each of the divisions. A more detailed description of the rock types will follow in Chapter 2.

Description of Stratigraphic Units

Grand Bay Complex

The GBC lies structurally beneath the PaBC and above the WPG. The GBC comprises a sequence of metamorphosed thin bedded shale-siltstone rythmites, feldspathic gneisses (mostly gneissic granite) and subordinate amphibolite units. The gneissic layering within the GBC is consistently oriented northeast-southwest and dips steeply to the southeast. Metamorphic grade for the unit as a whole is middle amphibolite facies as evidenced by the presence of hornblende in amphibolitic rocks and staurolite-kyanite-bearing assemblages in meta-pelitic units.

FELDSPATHIC GNEISSES

This unit comprises a sequence of predominantly leucocratic orthognesisses which weather tan to light pink. The thickness of the gneissic layers varies from a few meters to tens of meters. The rocks contain a strong foliation and a variable lineation which is usually S_2 and L_2, respectively. These rocks typically contain quartz (40-70%), plagioclase (20-40%) green-brown biotite (10-20%), muscovite (0-5%), garnet (0-<5%) and magnetite (0-2%). The grain size is .1 to 1mm. Although the rocks are now straight gneisses with a penetrative mylonitic fabric, a granitic (sensu lato) parent is inferred by the uniformity in texture and composition and by the presence of rare enclaves. Other thinner feldspathic gneisses may have a sedimentary protolith because individual layers fine upward on an individual outcrop scale, grading into semipelites

composed of fine grained muscovite, biotite, chlorite, quartz and plagioclase.

AMPHIBOLITIC UNITS

These rocks weather black with a light green tint and commonly have a schistose fabric. Metamafic layers may be up to 2 m thick with variable modal mineralogy. Due to intense deformation, most of the metabasic rocks are L-S tectonites, with a hornblende lineation. The rocks are medium grained and comprised of green-blue hornblende (30-60%), green-brown biotite (0-25%), variable amounts of quartz, plagioclase, ilmenite or rutile, and commonly subhedral dark red garnet porphyroblasts 1-5 mm in diameter. Garnet porphyroblasts generally occur near contacts with mica-rich gneisses, which suggests element mobility on a small scale. The green tint of these rocks is given by one or a combination of clinopyroxene, minor epidote and (or) Fe-rich chlorite. Minor ultramafic rocks are present, now partially altered to masses of chrysotile. All of the amphibolitic units have undergone strong transposition to give the appearance of parallel layering with the enclosing feldspathic gneisses; however, close inspection indicates that many of the amphibolites are discordant, and likely represent metamorphosed basaltic dikes.

METAPELITIC SCHISTS

In general, pelitic schists are uncommon (< 5% of total outcrop) in the GBC and usually do not exceed 2 m in thickness. In outcrop they may be recognized by their light green to silver sheen. The pelites are primarily fine- to medium-grained schists. Mineralogy varies but includes porphyroblasts of garnet (1-5%),

staurolite (1-5%), and kyanite (1-5%) in addition to green-brown biotite, chlorite, muscovite, plagioclase, quartz and ilmenite. A distinctive calc-pelite unit contains hornblende, kyanite and staurolite porphyroblasts with rare garnet. Green-brown pleochroic biotite, chlorite, white mica, plagioclase, quartz, ilmenite and rutile complete the mineralogy.

Port aux Basques Complex

The dominant rock types are felsic gneisses, metapelitic gneisses, amphibolitic units and minor metacalc-psammite horizons that as a unit structurally overlie the GBC along the Grand Bay Fault. The gneissic layering consistently strikes northeast-southwest and dips steeply to the southeast (Photograph 1c). Mineral lineations that likely indicate the stretching direction generally plunge to the southeast except near the Isle aux Morts fault zone where the rocks become mylonitic and develop a mineral lineation with a northeasterly plunge (Piasecki, 1990; Lin et al., 1993). These rocks were intruded by the syn-kinematic Port aux Basques Granite (Fig. 3). The PaBC contains upper amphibolite facies mineral assemblages evidenced by sillimanite-garnet-biotite-bearing gneisses. The PaBC also shows the development of leucosomes that may contain garnet and are often bounded by dark rims rich in biotite (Photograph 2b,2d). Leucosome/melanosome development is locally present in all rock types (Photograph 2c). The unit as a whole is characterized by the pervasive association of amphibolitic layers and pods with felsic gneisses and schists (Piasecki, 1991). This interlayering between amphibolites and felsic units is constant throughout the PaBC and is noticeably absent in both the GBC and the

HICG. On average, metabasic units comprise 30-35% of the outcrop, but may reach 50%.

FELSIC GNEISSES

The units are light grey to dark grey in color and have thicknesses that range from 1-3 m. The pervasive fabric is the S_2 foliation. A S_3 crenulation cleavage may also be present. The most conspicuous feature of the felsic gneisses is the development of leucocratic segregations. These rocks are migmatites and are characteristically medium grained biotite ± muscovite gneisses which contain elongate discontinuous leucocratic segregations of quartz and feldspar. These leucosomes commonly occur parallel to the main foliation as stromatic or occasionally schlieren structures. Although garnet is common in these gneisses it is often more concentrated and of a different morphology in the cores of the leucocratic material or leucosome (Photograph 2b,2d,2e). The leucosomes commonly abut thick biotite rich areas or melanosome at the interface between the leucosome and the paleosome or host gneiss (Photograph 2a,2b). The three parts of the migmatite described are inferred to form by metatexis and thus conform to the metatexites of M. Brown (1973). These medium grained gneisses include a range of rock compositions which contain variable proportions of quartz, plagioclase, green-brown to red-brown biotite ± muscovite, ± garnet, ± aluminum silicate. Most of these rocks are paragneisses with protoliths probably ranging from quartz arenites to greywackes. The gneisses become more feldspathic to the east. Orthogneisses also occur which show cross cutting

relations with the host gneiss and are extremely uniform in texture. Most of these orthogneisses probably represent melts associated with the Port aux Basques Granite due to the similarity of mineralogy between the two; close spatial relationship and common deformational fabrics (S_2, S_3) illustrating a common period of intrusion (see Intrusives below).

METAPELITIC GNEISSES

Metapelites are ubiquitous in the PaBC. The rocks are light tan when fresh and tend to muted oranges when weathered, often accompanied by a distinctive roughness due to differential weathering of the matrix around porphyroblasts. Average thickness of units rarely exceeds 1 m (Photograph 2f). Pelitic rocks are well foliated, medium- to coarse- grained, and often contain a mineral lineation defined by kyanite (L_2) or sillimanite (L_2 less commonly L_3). L_2 and L_3 are usually identified by overprinting relationships. Also on the limbs of F_3 folds, L_2 is usually recognized by its steep plunge. L_3 often has a very shallow plunge to the northeast or southwest. Locally in areas of lower D_2 strain such as F_2 hinge zones, S_2 is preserved as a differentiated crenulation cleavage and a composite S_0/S_1 schistosity is seen folded around the hinges of F_2 folds. However, the dominant penetrative foliation in the rocks is a composite $S_0/S_1/S_2$ fabric. The composite S_2 schistosity is defined by the three-dimensional orientation of micas and aluminum silicate minerals in schists and by hornblende in mafic rocks. As with the felsic gneisses, these rocks also contain discontinuous layer parallel, locally crosscutting, leucosomes surrounded by biotite-

rich melanosome. Leucosomes are composed of quartz and feldspar and may contain garnet or aluminum silicate (Photograph 3a). The mineralogy of these rocks consists of combinations of kyanite, and/or sillimanite, garnet, staurolite, biotite, muscovite, plagioclase, quartz and Fe-Ti oxides. In general, moving from west to east, kyanite is replaced by sillimanite as the stable aluminum silicate polymorph, staurolite and muscovite become absent and at the village of Margaree the assemblage includes alkali feldspar instead of muscovite. Kyanite and sillimanite can also be seen in leucocratic veins of quartz and plagioclase feldspar in the metapelites as well as in the host gneiss. In the metapelites, large (5-40 mm) porphyroblasts of pale blue to green kyanite, sometimes twinned, are generally well developed and may contain inclusions of garnet, staurolite and Fe-Ti oxides (Photograph 2f). Sillimanite occurs in both the fibrolitic and prismatic form. Crystals are large (5 mm to 10 cm). Fibrolite varieties generally form radiating masses partially pseudomorphed by muscovite or may form small faserkiesel aggregates. Garnets are usually pink and are of two varieties, small (2 mm) subhedral and larger (5 mm) grains commonly with inclusions of Fe-Ti oxides, biotite, kyanite, staurolite and quartz. Garnets range in modal percent from 2-5%. Poikiloblastic, subidioblastic staurolite is deep brown, up to 40mm in length, and may be twinned. The percentage of staurolite in a given outcrop may vary widely. Biotite in the western portion of the area is green-brown while biotite toward the east becomes red-brown and may be intergrown with sillimanite. Muscovite, plagioclase and quartz vary in abundance. Rutile and ilmenite occur

both as matrix minerals and as inclusions within porphyroblasts.

AMPHIBOLITES

Amphibolites within the PaBC are dark grey to black, often with a green tint. Unit thicknesses range from a few centimeters to 4 meters. These rocks all have a strong L>S fabric, with the lineation defined by hornblende. The lineation plunges steeply to the northeast. Many of the amphibolites also have a strong S fabric with the schistose fabric most strongly developed in biotite-bearing amphibolites. In biotite-absent amphibolites near shear zones, the rock is almost a pure L tectonite. Mineralogy consists of hornblende, plagioclase, quartz ± clinopyroxene ± garnet ± biotite ± titanite ± rutile ± ilmenite in variable modal proportions. Quartzo-feldspathic leucosomes with irregular biotite-rich selveges are locally present (Photograph 2c). Green epidosite nodules or veins are present in some of the units with mineralogy consisting of mostly epidote and minor calcite that has replaced the hornblende and plagioclase (Photograph 3b). Euhedral to subhedral hornblende is green-brown in the western part of the area and becomes brown to the east. Subhedral clinopyroxene is pale green in color, subhedral to euhedral poilkiloblasts of dark red garnet contain inclusions of quartz, plagioclase, hornblende and Fe-Ti oxides.

A discordant relationship between the host gneiss and some of the amphibolitic units is evident from the truncation of fine layers in the host. Amphibolite streaked out into layers, larger blocks of amphibolite deformed and flattened but showing less deformation internally and markedly different plunges of hinge lines of same generation folds in the gneisses and metabasic rocks all suggests

that some of the amphibolitic units were originally at angles to the layering in the host gneiss and thus likely were originally dikes. However, other amphibolites which are not discordant are interpreted to be metavolcanic tuffs, sills or flows (van Staal et al. 1992a).

METACALC-PSAMMITES

Grey metacalc-psammites with beds as much as 10 cm in thickness are a distinctive feature within the PaBC. The rocks contain a weak gneissic fabric (S_2). Mineralogy consists of poilkiloblasts of coarse (3-6 mm) green-brown hornblende and variable size orange garnets containing inclusions of plagioclase and quartz set in a plagioclase-quartz matrix. Epidote also may be present in the matrix or as inclusions surrounded by hornblende. These calc-psammites horizons are usually in contact with the felsic gneisses, but can be observed within conformable metabasic units, interpreted to represent metavolcanic tuffs or flows (van Staal et al., 1992).

Margaree Complex

The Margaree Complex lies to the south-southeast of the PaBC, separated from the latter by a northeast-southwest trending shear zone (van Staal et al., 1992b). This group is characterized as a migmatitic complex of strongly deformed heterogeneous, layered quartzo-feldspathic gneiss with dark and light components, containing partly fragmented amphibolitic units (Photograph 3c). Numerous structural types of migmatites occur in this area. Diktyonitic, stromatic and schollen migmatites all occur. Rock types are amphibolite, metaultramafics, and granites/granitic

gneisses. Garnet-sillimanite-biotite-alkali feldspar- bearing gneisses with stromatic migmatitic structures make up a minor portion of this unit. Feldspathic pegmatite veins cut across the tectonic layering.

AMPHIBOLITES

The dark grey to black amphibolites are strongly deformed often tightly folded and boudinaged (Photograph 3d). Quartzo-feldspathic material commonly fills the area between boudin necks. Folded amphibolites may have streaked out fold limbs, other amphibolites occur as enclaves within granitic gneisses. Rafts of amphibolitic gneiss occurs as disrupted blocks often surrouned by leucocratic material (Photograph 3d). Mineralogy consists of hornblende, plagioclase, ± quartz ± garnet ± clinopyroxene.

META ULTRAMAFICS

Ultamafic pods surrounded by high strain zones occur in the Margaree Complex. Exposures range in size up to 10-15 meters in length and 5 meters in width. These pods are essentially actinolite-spinel-clinopyroxene rocks. The clinopyroxene occurs as large (5-10mm) grains partially replaced by talc. The actinolite is medium grained and makes up the bulk of the rock. Spinel makes up around 2% of the rock and is partly replaced by an opaque mineral.

GRANITES/GRANITIC GNEISSES

Intercalated with the amphibolites are strongly deformed and migmatitic metadioritic rocks (Photograph 3c). These rocks are generally a pale grey on weathered surfaces. The mineral assemblages in these rocks are quartz and plagioclase ± biotite. Cross cutting relationships are abundant from a large volume of

granitic intrusives that have been injected into the amphibolites and metadiorites. The compositions of the intrusives range from plagioclase with lesser quartz tonolites to two feldspar granites. Many of the intrusives are deformed and may form augen gneisses. Porphyroclast tails from feldspar in these augen gneisses generally show a dextral sense of shear. Other intrusives are not deformed but may contain "ghost" layering that mimics the gneissic layering in the surrounding gneisses.

Harbour Le Cou Group

The HlCG lies to the east of the PaBC and is separated from the latter by a steeply northwest-dipping strike-slip shear zone, the Isle aux Morts Fault Zone. In contrast to the PaBC gneissic layering that consistently dips to the southeast, the HlCG often dips to the northwest. The HlCG is a lithologically distinct, monotonous group of paragneisses whose protoliths were likely sandstones, lithic arenites and occasional shale-siltstone rhythmites (Lin et al., 1993). Locally the units exhibit graded beds. Amphibolitic units are sparse and many appear to be intrusive. Calc-silicate pods are present in the thicker metasandstone units and in amphibolites. Field observations of the rock units in the vicinity of the Rose Blanche Granite (discussed below) reveal a gradual transition from the gneisses and schists which contain few migmatitic features to rocks with stromatic migmatitic structures, to rocks which resemble schollen migmatitic structures and finally the Rose Blanche Granite itself with numerous xenoliths of the surrounding country rock. This transition can be locally found near larger bodies of the Rose Blanche Granite. Sillimanite, garnet and biotite-

bearing assemblages indicate that metamorphic conditions are middle to upper amphibolite facies.

PARAGNEISSES

These gneisses are generally medium-grained and vary in color on weathered surfaces from light grey in the more quartz rich varieties, silver-orange in the more pelitic rocks, to orange-brown in units having a high sulphide content. Unit thicknesses are on the order of centimeters for the rhythmites but reach more than 10 m for some quartzites. The S_2 fabric is the dominant foliation in the rocks. In the more pelitic rocks a crenulation cleavage (S_3) is developed. The quartzites contain greater than 80% quartz and plagioclase with minor garnet, muscovite and biotite. The quartzites also locally show features interpreted as graded bedding. Some quartzites also contain lenses and pods of sillimanite-bearing pelites or calc-silicate nodules. Locally, sillimanite occurs in the pressure shadows of large (> 1 cm) pale purple garnets. The pelitic layers generally contain sillimanite-garnet bearing assemblages and a well developed schistosity defined by red-brown biotite. Pink garnets are generally large (> 5 mm) and contain numerous inclusions of sillimanite, quartz and occasional biotite. Large (4-7 mm) muscovite grains locally cut across the schistosity. Other matrix minerals include rutile, ilmenite, plagioclase and quartz.

AMPHIBOLITES

Amphibolites are rare in the HICG. They are dark grey to black in outcrop. Amphibolites show intrusive relationships and interlocking textures found in low strain zones confirm an igneous

protolith (van Staal et al., 1992a). The rocks are generally 2-3 m in thickness. Amphibolites located at Burnt Island and Isle aux Morts are as much as tens of meters thick with well preserved pillow structures and are interpreted as metabasalts (Lin et al., 1993). The rocks usually have a strong lineation (L_2) defined by hornblende and a well-defined schistosity which is more pronounced in biotite-bearing varieties. The rocks are plagioclase-hornblende gneisses and contain calc-silicate pods, which are interpreted as interpillow material (van Staal et al., 1992b; Lin et al., 1993). Accessory minerals include garnet, titanite, clinopyroxene and ilmenite.

CALCSILICATES

Calc-silicates in the HICG occur as small irregular shaped pods in quartzites and in amphibolites. These rocks differ from the metacalc-psammites of the PaBC in that the PaBC rocks have a much simpler mineralogy never having clinopyroxene or calcite. The PaBC calcareous units also occur as beds instead as pods as do those of the HICG.

Calc-silicate pods in amphibolite at Burnt Island are interpreted to represent interpillow material in metabasalts (Lin et al., 1993). They are cream colored with a weakly developed S_2 fabric. Grey reaction rims of plagioclase often surround the contacts with the host amphibolite. The rocks are medium to coarse-grained with distinctive orange poilkiloblasts of garnet and green subhedral porphyroblasts of clinopyroxene or hornblende. Accessory mineralogy and modal abundances vary widely, depending on locality and host rock. Plagioclase is consistently present with additional

minerals as follows: garnet, quartz, clinopyroxene, alkali feldspar, titanite, calcite, zoisite and biotite. The mineralogy of calc-silicates in the quartzites are generally simpler with garnet, quartz, plagioclase, clinopyroxene and hornblende.

Granitoids

Numerous syn- and postkinematic granitoids have intruded the area. The Grand Bay Granite is a highly deformed and in some places mylonitic rock, that has syn-kinematically intruded the GBC and the Grand Bay Fault (van Staal et al., 1992b). Its age and origin are otherwise unknown. The Port aux Basques Granite (PaBG) as defined by P. A. Brown (1973) is a pink, commonly two mica granite that intrudes the PaBC. Generally, it is a tonolite to diorite, in other parts it may contain abundant biotite and occasional garnet. More highly sheared versions are finer grained and contain muscovite and biotite along with garnet. This granitoid cuts S_1 but locally contains a S_1 foliation folded by F_2. It also contains a strong schistosity (S_2) and an overprinting weaker fabric (S_3). Given the structures present and the outcrop pattern of the PaBC, the granite was likely intruded as sheets within the PaBC syn-D_1 and was subsequently folded into upright, shallow plunging folds associated with D_3.

The Rose Blanche Granite (RBG) (Brown, 1976) is a syn-kinematic garnet bearing granite which intrudes the HICG. The RBG differs from the PaBG in that the later is an alkali feldspar granite while the former is a granite, sensu stricto. Benn et al. (1993) have interpreted this granite to be synkinematic and intruded along dilatational shear zones during the early stages of the third

deformation. Contacts with the HICG vary from sharp to gradational or migmatitic. Country rock near the contact with the granite becomes progressively more migmatitc and contains numerous xenolithic blocks of sillimanite-bearing paragneisses.

The Strawberry Hill and Isle aux Morts Brook Granites are undeformed post tectonic granitoids that intrude the Windsor Point Group, the GBC and the PaBC. Wilton (1985) describes a thermal aureole around the granites. He suggests an age of 362 ± 16 Ma (MSWD: 6.3) based upon a composite Rb/Sr whole rock isochron using samples from both the granites on the same isochron (Wilton, 1983).

Chapter Summary

In the preceding discussion, I outlined all of the major rock types within the Port aux Basques Gneisses. Basic textures, structural relations and outcrops patterns were identified. Important to note, is that the GBC does not contain migmatites or evidence for metatexis. However, examples of various migmatitic structures are present in the PaBC, MC and the HICG. Mineralogy changes systematically from west to east: metapelites of the GBC contain garnet and (or) staurolite and (or) kyanite bearing assemblages, whereas sillimanite appears in rocks of the PaBC, MC and the HICG and sillimanite plus alkali feldspar- bearing rocks occur in the MC. Numerous synkinematic granitoids are present within all the major divisions. The Strawberry Hill and Isle aux Morts granites are undeformed and display a thermal aureole.

Chapter 3 will discuss textural relations combined with structural data discussed earlier, in order to determine

porphyroblast/matrix relationships. Phase assemblages and mineral chemistry will be combined with field observations to determine reactions responsible for the changes in mineral assemblages seen in the metapelitic gneisses.

Metamorphic Evolution

Petrography of the Metapelites, Amphibolites and Metacalc-Silicate Rocks

Although the lithologic character is distinct for each of the divisions of the Port aux Basques Gneisses, textural and structural relations are similar. Metapelitic rocks are well foliated, medium- to coarse- grained, and often contain a mineral lineation defined by kyanite (L_2) or sillimanite (L_2 or less commonly L_3). The dominant penetrative foliation in the rocks is a composite $S_0/S_1/S_2$ fabric. The composite S_2 schistosity is defined by the three-dimensional orientation of micas and aluminum silicate minerals in metapelites and by hornblende in mafic rocks. Matrix quartz and plagioclase generally have straight rather than serrated grain boundaries. Subhedral porphyroblasts of coarse (> 2mm) garnet, staurolite, kyanite and sillimanite commonly lie in or are wrapped by the S_2 fabric. Metapelites of the GBC and western PaBC contain kyanite-staurolite-garnet-bearing assemblages which are replaced to the east by sillimanite-garnet-bearing assemblages.

Metapelites in areas of penetrative D_3 strucutures display a local well developed S_3 foliation locally accompanied by retrogressive effects such as embayed garnet grain boundaries. Areas of penetrative D_4 deformation display marked effects of retrogression: porphyroblasts of garnet display embayed grain boundaries and partial replacement by chlorite, biotite is replaced by chlorite along cleavage planes, and aluminum silicates are

partially replaced by white mica.

In amphibolites idioblastic hornblende prisms 1-4mm in length define a schistosity and steeply plunging lineation (L_2). Locally a second generation of hornblende obliquely overprints the L_2, S_2 fabric and define L_3. Hornblende in amphibolites of the GBC is blue-green, but in general, hornblende becomes more green-brown to the east and the hornblende from rare amphibolites of the HICG west of Burnt Island is brown. Garnet and clinopyroxene porphyroblasts commonly lie in or are wrapped by the S_2 fabric.

In the HICG, calc-silicate pods or nodules are abundant in metasandstones and amphibolites. These rocks are medium to coarse-grained with distinctive orange poilkiloblasts of garnet, and green subhedral porphyroblasts of clinopyroxene or hornblende. Plagioclase is consistently present with additional minerals as follows: garnet, quartz, clinopyroxene, alkali feldspar, titanite, calcite, zoisite and/or biotite.

Prograde Textures

Progressive metamorphism involves a complex structural and mineralogical history leading to the development of deformational fabrics such as crenulations and the growth of porphyroblasts. Porphyroblasts that grow at any particular stage of the structural development may preserve evidence of it in the form of inclusion trails or sets of inclusion trails. The actual geometry of the inclusion trails will depend on the exact timing and location of porphyroblast growth with respect to the developing fabric. In order

to relate thin section textures to structures identified on outcrop scale, thin sections for microstructural analysis were cut parallel to the rock lineation and perpendicular to the foliation; however, some thin sections were cut perpendicular to the hinge lines of crenulation microfolds.

The temporal connection between metamorphism and deformation is established by using porphyroblast-matrix foliation and porphyroblast-inclusion relations. Inclusion trail relations will be discussed with reference to Bell and Rubenach's (1983) six stages of crenulation cleavage development. This concept of porphyroblast growth requires that the deformation was heterogeneous and partitioned into noncoaxial, low strain zones and coaxial, high strain zones allowing the growing porphyroblast to successively include the relict fabric of a developing crenulation cleavage (e.g. Bell 1985, 1986). Bell's model has shown increasing applicability in amphibolite facies rocks (Vernon, 1989 and references therein). Regardless of whether the details of the Bell's model are accepted or not, curved inclusion trails are of great assistance in relating porphyroblast growth to generations and stages of crenulation development.

S_1 is recorded as inclusion trails in porphyroblasts and as a strongly differentiated layering defined by micas in the hinge zones of F_2 folds. The main fabric in these rocks is S_2, which is a composite fabric reflecting the transposition of S_0/S_1. Mineral growth during D_2 can be demonstrated because of the abundance of porphyroblasts with curved or slightly curving inclusion trails

combined with matrix foliation relationships. When compared to the inclusion trails in porphyroblasts, the S_2 fabric outside of these pophyroblasts generally displays evidence of recrystallization and grain coarsening that occurred later in the D_2 event.

Thin section 92-71 is interpreted as showing S_1 in the pressure shadows of a syn- D_1 garnet (Photograph 3e). Outside of the pressure shadows, the S_1 fabric is folded into F_2 microfolds and transposed into the S_2 fabric. Additionally, micas define a differentiated layering in the hinge areas of F_2 folds. D_2 growth of mica is evident in many samples as it in large part defines the main foliation S_2. D_3 growth of mica is typified in sample 91-77 which is a garnet-mica schist of the PaBC and is shown in photograph 3f. This is interpreted as showing that both muscovite and biotite have recrystallized into strain free grains around the hinge of a F_3 fold. In contrast, thin section 92-110 illustrates that conditions were not favorable for mica recrystallization during D_4 (Photograph 3g). In this sample mica has been bent around a F_4 crenulation. Extinction patterns of these micas, as observed under crossed nicols, suggests a lack of recrystallization in response to the folding event. Generally, muscovite and biotite appear to have grown during D_1 through D_2 and both have recrystallized as strain free grains around F_3 folds, indicating their stability during early D_3. Chlorite occurs as inclusions in garnet and as a late replacement of M_2 biotite and garnet in metapelitic gneisses. Thus, chlorite is inferred to have grown after D_2.

Evidence for porphyroblast growth during the early stages of metamorphism is lacking. However, thin section 92-71 may provide evidence of syn- D_1 growth of garnet. In this thin section, as discussed above, relict S_1 remains because of protection by a garnet. This garnet contains slightly curving inclusions in the core of the garnet which are parallel to the remnant S_1, to suggest growth during D_1 or early D_2, and this same garnet is now overgrown by a relatively inclusion free rim which is wrapped by the S_2 fabric. Additionally, some garnet porphyroblasts preserve sinuous inclusion trails in the core that are oblique to the S_2 matrix foliation. For example, sample 91-68 contains sigmoidal inclusion tails (S_1) in the core of a garnet which may represent more extensively developed crenulations which are oblique to the external S_2 fabric (Photograph 4a). A post-D_1 - pre-end D_2 garnet rim now separates the discordant core inclusion trails from the external S_2 fabric. This suggests that S_1 in this rock may be a crenulation cleavage of a pre-existing fabric. Garnets may contain crenulations defined by inclusions of opaque minerals that are interpreted to resemble stage 3 of Bell and Rubenach (1983) cleavage development. Other garnets display overgrowth of what is interpreted to be stage 5 or 6 wrapped by the foliation. An example of the former type (Stage 3) is provided by sample 91-52 (Photograph 4b). In this sample inclusions within the garnet preserve crenulations of an earlier fabric, likely S_1 captured during D_2 growth of the porphyroblast. An inclusion free rim now separates the porphyroblast from the external S_2 matrix. A further example where the crenulations are better preserved is in

photograph 4c. An example of later stage (5 or 6) growth of garnet is suggested in specimen 91-136C (Photograph 4d, 4e). The core of this garnet contains relatively straight inclusion tails (S_0/S_1) preserved during an early growth stage of the garnet. Inclusions of ilmenite suggest a later developing fabric has been flattened around the core. This fabric then merges with the current S_2 suggesting syn-D_2 growth of this stage of the crystal. An outer relatively inclusion free rim has overgrown the flattened fabric. The rim of this garnet likely represents syn to late-D_2 growth. More problematic is the age relationship of small idioblastic garnets that occur in the matrix. Commonly these garnets have inclusion-rich cores and inclusion-poor rims. In the cores of many of the above garnets the inclusions are small and randomly oriented indicating rapid growth at a time when the matrix grains had not coarsened to any significant extent. Garnets of comparable size and shape occur as inclusions in early-syn-D_2 kyanite or staurolite porphyroblasts to suggest that they grew before D_2. Some garnets in thin sections HLC-11b and 91-131A contain kyanite or sillimanite inclusions in their rims, indicating garnet growth concurrent with or after aluminum silicate growth (see below) (Photograph 4f).

From the above relationships garnet porphyroblasts appear to have grown during D_1 or between D_1 and D_2 and during D_2. These growth stages are not interpreted to represent temporally separate growth events but correspond to the production of garnet by different reactions during progressive metamorphism and continuing deformation.

Age relationships of staurolite with respect to kyanite are difficult to ascertain. Staurolite and kyanite may be intergrown or each may include the other; both minerals are seen to be wrapped by the S_2 schistosity. Staurolite may contain inclusion trails representative of stages 1, 2 or 3 of Bell and Rubenach (1983), that are oblique to the external fabric. Field relations show staurolite with an internal schistosity and wrapped by an external schistosity (S_2) (Photograph 5a). This suggests that the staurolite porphyroblast grew early syn-D_2 (Photograph 5a). Thin section 91-56B shows quartz and ilmenite inclusions in staurolite that are interpreted to preserve an earlier microfold (Photograph 5b). The limbs of this fold extend to the edge of the crystal where they are parallel to the surrounding S_2 fabric. This geometry suggests that the microfold is likely F_2 and represents a crenulation of S_1 preserved during growth of staurolite concurrent with transposition of the S_1 fabric into the current dominant S_2 fabric which now wraps the crystal. Thin section 92-87A also shows staurolite porphyroblasts containing inclusion trails outlining microfolds of what is interpreted to be F_2. Additionally sample 91-136 shows the S_2 schistosity to wrap around one end of a large (20 mm long) single staurolite porphyroblast (Photograph 5c). The staurolite, which could be pre- or early syn-D_2, includes an earlier kyanite. From the above relationships staurolite growth appears to have been restricted to early-syn D_2.

Determination of the timing of kyanite growth is more complicated. Kyanite is locally folded by F_3 crenulations

(Photograph 5d). Early D_2 growth of kyanite is indicated in sample 91-68 which shows quartz inclusion trails that resemble the early stages of crenulation cleavage development (stage 2 of Bell and Rubenach, 1983), i.e. S_i curves into the transposive S_2 fabric at the rims (Photograph 5e). Thus, S_i is interpreted to represent a progressively rotated S_1 fabric. This texture is consistent with early- syn-D_2 growth of kyanite. Also kyanite is locally folded by F_2 which suggests growth during early- D_2 or growth during D_1. Photograph 5f is interpreted to show syn- to late-D_1 kyanite preserved during the formation of the S_2 fabric. The kyanite at this outcrop is folded by small scale F_2 folds. D_1 or early-D_2 kyanite is also indicated by photograph 6a that shows a kyanite porphyroblast which grew during late D_1 or early during the D_2 folding and S_2 crenulation cleavage formation, which has been wrapped later by S_2 as the developing S_2 foliation transformed into a schistosity. The kyanite appears to have rotated during the development of S_2 and is now curved at each end by post-crystallization deformation.

Thus, some kyanite likely grew during D_1 but must have also grown during the early stages of D_2.

Textural relations of sillimanite are also complex. Sillimanite occurs as: 1) anastomosing folia defining the S_2 fabric; 2)radiating aggregates that partially pseudomorph after kyanite; and, 3)inclusions in syn-D_2 garnets and mica. In addition, sillimanite can be found as inclusions in large, late, cross muscovites that postdate the S_2 fabric. Many of these different modes of occurrence

of sillimanite can be found in the same rock. Rather than inferring separate growth stages for sillimanite in these rocks, which is not supported by microstructural relations, the sillimanite is interpreted to have grown syndeformationally during D_2. Following the suggestion of Vernon (1975, 1987), the deformation is interpreted to be partitioned into high and low strain zones even within an individual thin section. This partitioning effect can be seen in samples 92-74 and 91-70 where heterogeneities such as porphyroblasts create strain gradients in the rock which result in an overall noncoaxial deformation being partitioned into bulk zones of inhomogeneous shortening and highly noncoaxial shear strain. Because of the inhomogeneity, deformation partitioning occurs around quartz rich domains or porphyroblasts. In the sample 91-70, undeformed aggregates of sillimanite can be found to pseudomorph kyanite, while the enveloping matrix fabric has been flattened around these same crystals (Photo 6b). Additionally, other samples such as 92-74 show areas of low strain where microfolds of sillimanite are preserved which elsewhere in the rocks have been fully rotated into the transposed fabric.

Microstructural relations of sillimanite show that the mineral is consistently folded by F_3 (though mimetic growth after mica cannot be ruled out in all situations) but locally defines the L_3 lineation in S_3. As an example, sample HIC-4 shows S_0 layering and S_1 schistosity crenulated by S_2, all folded by F_3. Sillimanite lies in the schistosity and is folded by F_3 (Photograph 6c). Sample 91-150 is seen in photograph 6d showing S_2 sillimanite which has

recrystallized during folding by F_3. Photograph 6e shows S_2 sillimanite in a migmatitic gneiss virtually completely transposed into S_3, axial planar to F_3 folds. Photograph 6f shows sillimanite prisms that define the L_3 lineation.

From the above, sillimanite appears to have grown during syn- to late-D_2 and remained stable during the early stages of D_3. In many cases, sillimanite was replaced by muscovite after F_3 folding.

Alkali feldspar in sillimanite- bearing gneisses lies within the S_2 layering and forms leucosomes which are also parallel to the S_2 fabric.

Porphyroblast growth with respect to deformation is summarized in table 1.

Amphibolite may comprise up to 50% of some exposures. Early idioblastic hornblende prisms in the amphibolites define a LS fabric related to D_2 metamorphism and deformation. Hornblende in F_2 microlithons recrystallized during D_2 folding, to indicate either that hornblende was mimetic after the S_1 fabric or that growth of hornblende occurred during D_1 and D_2. Hornblende also has recrystallized around F_3 folds and defines the strong lineation seen in late- to post- D_2 mylonites that comprise the GBF. Clinopyroxene porphyroblasts are wrapped by the S_2 fabric.

Microstructural evidence indicates that the porphyroblasts characteristic of peak conditions grew early- to syn- D_2 with sillimanite dominantly growing later during D_2, and probably remaining stable during rotation into the S_3 fabric. Therefore, the

Style of Deformation	
D1-Isoclinal Recumbent (?)	D2-Isoclinal Recumbent
D3-Upright to Inclined	D4-Kinks or minor crenulations

Metamorphic Mineral (MetaPelites)	Stages of Deformation			
	D1	D2	D3	D4
Chlorite	?		- - - - -	
Muscovite	- - ———	———	———	- -
Biotite	- - ———	———	———	- -
Staurolite	- ——— -			
Garnet	- - ———	———	-	
Kyanite	- - ———	———	-	
Sillimanite		- ———	———	-
K-feldspar		- ———		

The above chart summarizes: 1)the basic fold styles associated with each phase of deformation (D1-D4); 2)porphyroblast growth stages with respect to the deformational sequence.

Table 1. Summary of porphyroblast growth with respect to the deformational sequence.

D_2, and possibly D_1, structures were accompanied by syntectonic amphibolite facies metamorphism, the peak of which occurred during D_2. Recrystallization and/or growth of micas and hornblende continued during the early stages of D_3. Matrix kyanite growth everywhere predates syn-late D_2 and likely grew during D_1. Sillimanite grew during D_2. D_3 (M_3) was mostly retrogressive with respect to M_2 but P-T conditions during early D_3 appeared to have remained in the stability field of sillimanite in metapelites and hornblende in amphibolites. The deformational sequence and microstructural relations discussed above are the same for each division and so it seems likely that their metamorphic histories are related and part of the same orogenic event.

Phase Assemblages and Mineral Chemistry

Mineral paragenesis varies systematically across the study area. Metapelitic rocks of the GBC contain the following assemblages*:

Chl + Ms + Bt;

Chl + Ms + Bt + Grt;

Ms + Bt + Ep + Grt;

Chl + Ms + Bt + Grt + St;

Ms + Bt + Grt + Ky.

Metapelitic rocks of the PaBC are characterized by the following assemblages:

Ms + Bt + Grt + Ky;

Ms + Bt + Grt + St;

Ms + Bt + Grt + St + Ky;

Bt + Grt + St + Ky;

Ms + Bt + Sil + (Ky) + St + Grt;

Bt + Sil + (Ky) + Grt;

Bt + Sil + Grt;

Bt + Sil + Grt + Kfs.

Metapelitic rocks of the HICG contain the following assemblage:

Bt + Sil + Grt ± Ms

*All assemblages contain plagioclase and quartz; mineral abbreviations from Kretz (1983).

General field observations in the metapelites are that towards the southeast kyanite is replaced by sillimanite, staurolite and muscovite disappear as part of the prograde mineral assemblage and alkali feldspar becomes part of the stable mineral assemblage. Kyanite and staurolite are developed throughout the GBC and as such no isograd for the first appearance of these minerals may be drawn. However, a kyanite to sillimanite mineral isograd was mapped by the replacement of sillimanite as the stable aluminum silicate polymorph in aluminum silicate + garnet + biotite-bearing gneisses. Mineral zones that were mapped are the kyanite zone, a lower sillimanite zone and an upper sillimanite zone (see Fig. 9). In the kyanite zone, metapelitic rocks contain the assemblage kyanite + staurolite + garnet + biotite ± muscovite + quartz + plagioclase. The lower sillimanite zone metapelite mineralogy consists of sillimanite (± metastable kyanite) + staurolite + garnet + biotite ± muscovite + quartz + plagioclase. The disappearance of staurolite defines the boundary between the lower and upper sillimanite zones. A sillimanite + alkali feldspar isograd was not mapped due to the

Figure 9. Metamorphic map showing the sillimanite-in isograd and mineral zones.

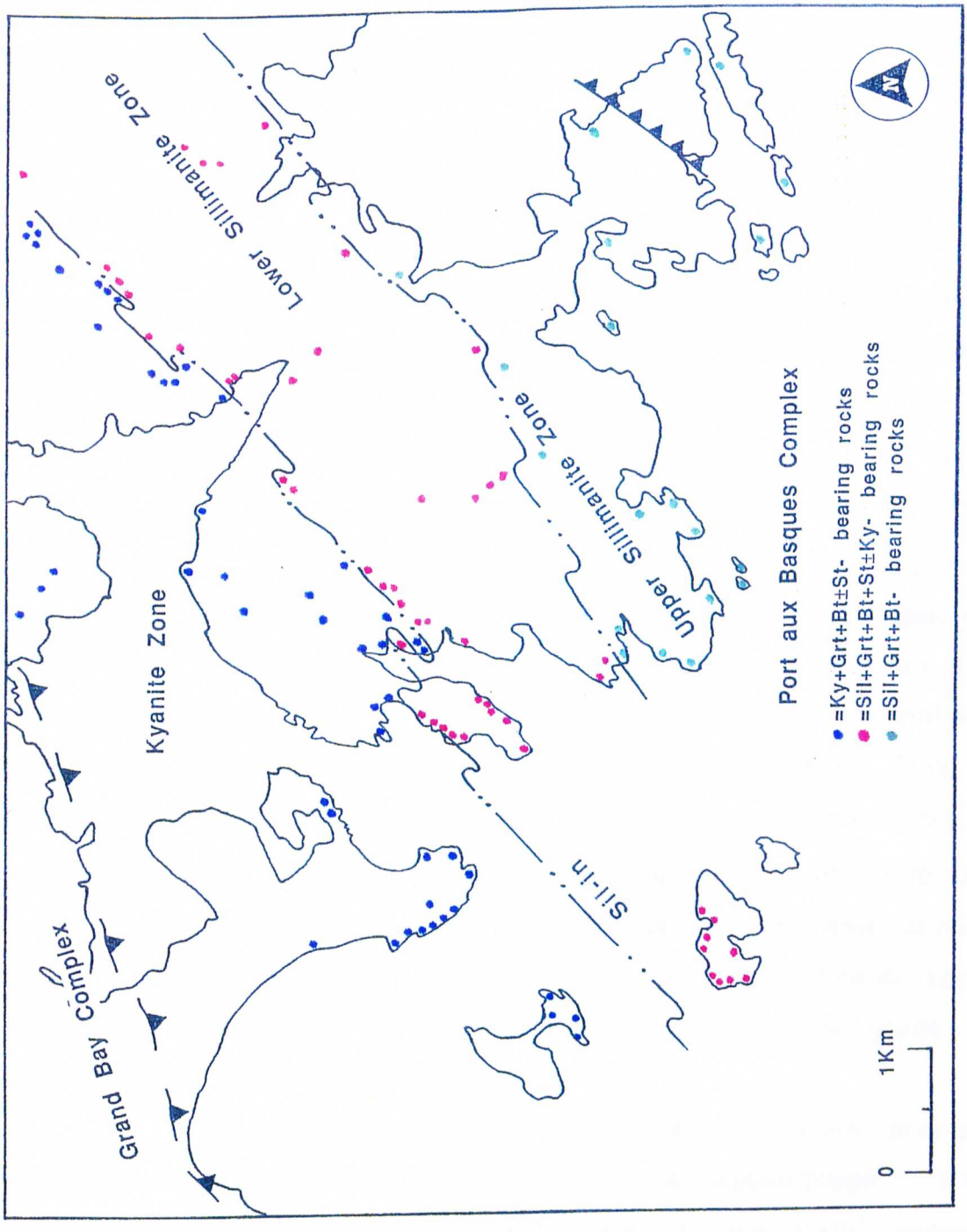

limited number of exposures containing these phases.

The present study shows that the kyanite to sillimanite isograd has been modified by D_3 as the isograd does not necessarily follow explicitly the regional trend of the gneissic fabric. Peak metamorphism and isograd surfaces are syn-D_2 and as such isograd surfaces are related to syn-D_2 metamorphism. These surfaces were probably originally subhorizontal to inclined, mimicking the thermal structure created by the F_2 recumbent folds, but have been deformed subsequently by large-scale F_3 antiforms and synforms. If the isograd surface was inclined to the east then it would act as a passive marker during D_3 folding. The trace of this plane onto the earths surface would result in asymmetric folds. The apparent linear trend of the isograd when viewed from a distant perspective may result from the current trace representing a limb on the asymmetric folds. The kyanite to sillimanite transition is spatially coincident with the first D_3 antiform within the PaBC. This is interpreted to indicate that D_3 folding has brought up hotter rocks in the core of the antiform whereas the accompanying synform to the west exposes cooler rocks that might represent higher level crustal rocks, i.e. kyanite bearing lithologies. Isograd and mineral zone distribution indicates a regional increase in metamorphic grade to the east.

The ensuing discussion will concentrate on more precise efforts to quantify these changes in mineral assemblage. The following is concerned primarily with rocks of the PaBC except where otherwise noted.

Kyanite zone metapelites consist of Ky + St + Grt + Bt + Pl + Qtz ± Ms ± Fe-Ti oxides. In general, staurolite decreases in modal percent to the east while kyanite increases. Textural evidence for reaction progress in these rocks includes: kyanite increase in the mode; biotite and staurolite depletion halos around garnet; kyanite inclusions in garnet; and, armored staurolite relics in plagioclase, garnet or kyanite (Photograph 4g). Chemical data and textural observations were integrated in order to deduce mineral reactions in these rocks. Many of the reactions for the metapelites presented below are based on equilibria in the model AFM or KFMASH system. Further, the reactions presented below are not balanced, but are presented in a general form since the reaction stoichiometry of many KFMASH reactions change along the reaction curve in P-T space. A petrogenetic grid is shown in figure 10 that details the relevant reactions in these rocks. In plotting these reaction curves in P-T space, the activity of H_2O was considered equal to 1. In that these gneisses do not contain graphite nor are there significant carbonate rocks in the area, this seems a valid assumption.

For the study area, staurolite rim compositions become more Mg-rich (where XMg = 100*Mg/(Fe + Mg)) geographically to the east from XMg≈12.5 in sample 91-136 to XMg≈23 in sample HIC-11. See appendix 2 for sample locations. However, staurolite compositional profiles within individual thin section are variable but larger porphyroblasts in kyanite- bearing rocks show a decrease in XMg toward the rims. The change in XMg is systematic and does not display a pattern indicative of late Fe-Mg exchange. For example, staurolite compositions in sample 91-136 record XM_g= 21 for the

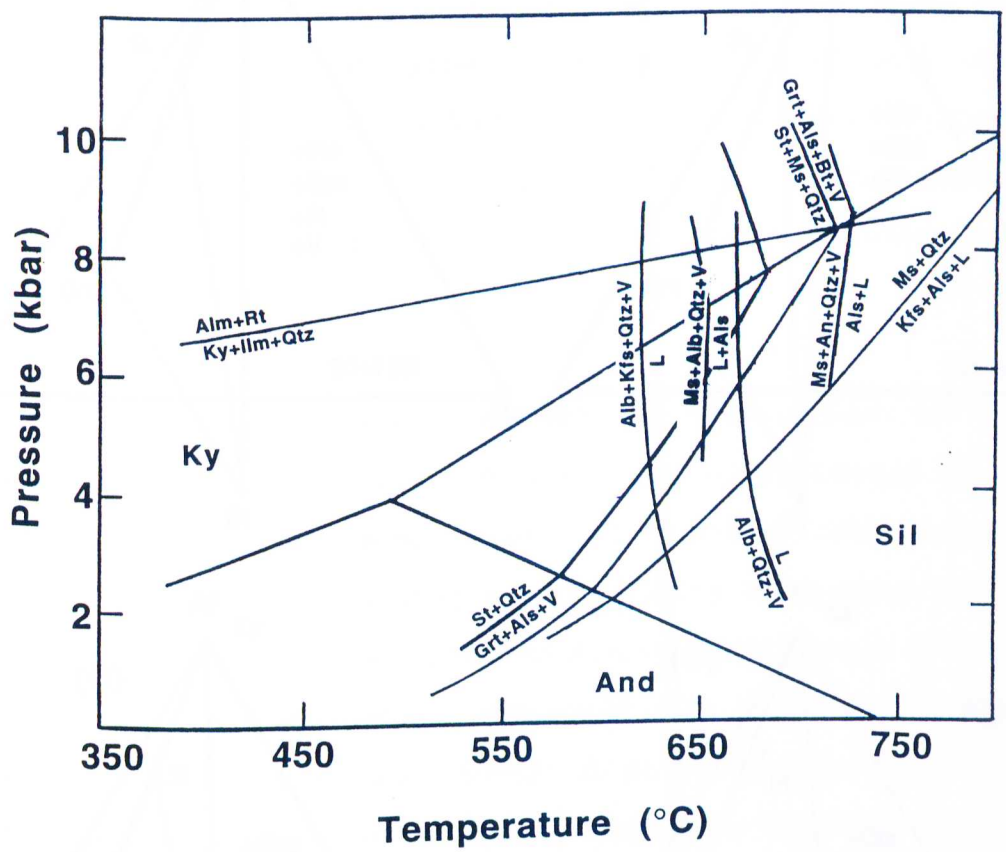

Figure 10. P-T grid after Spear and Cheney (1989). Additional equilibria are Alm+Rt = Ky+Ilm+Qtz (Bohlen et al., 1983); Ms+Qtz = Kfs+Als+L (Thompson, 1982); Alb+Kfs+Qtz+V = L, Ms+Alb+Qtz+V = Als+L, Ms+An+Qtz+V = Als+L, Alb+Qtz+V = L (Thompson and Tracy, 1979).

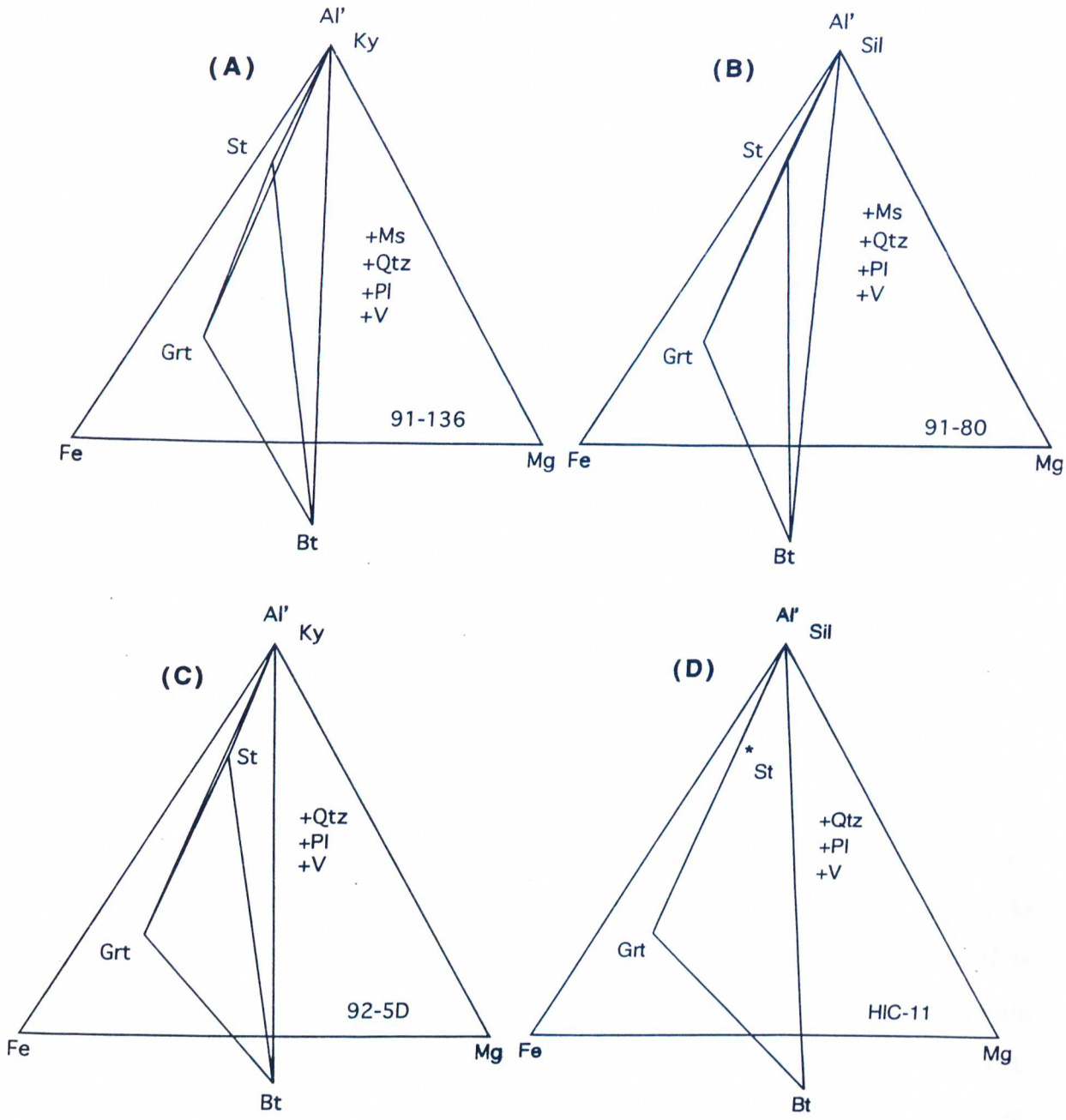

Figure 11. AFM diagrams showing the topology of mineral assemblages using actual mineral compositions from four metapelites of the Port aux Basques Gneisses. See text for details.

core, XMg=12 for the rim. Thus, in these kyanite-bearing rocks the staurolite composition becomes more iron-rich with reaction progress. Following the usual chemography in metapelitic schists of $XMg^{Bt} > XMg^{St} > XMg^{Grt}$ the formation of some kyanite in conjunction with the disappearance of staurolite can be attributed to the following reaction where the mineral paragenesis becomes more Fe rich as the continuous reaction proceeds:

St+Ms+Qtz = Bt+Ky+V. (1)

The above reaction does not however explain all reaction textures in these rocks such as that exhibited by sample 92-80. In this rock, depletion halos depleted in staurolite and biotite occur around garnet and coexisting kyanite leaving the garnet surrounded by a matrix primarily of quartz with minor plagioclase (Photograph 7a). This type of textures, combined with intergrowth textures of kyanite and garnet (samples 91-131 & 92-80) suggest the occurance of biotite and staurolite consuming reactions, kyanite- and garnet-producing reactions. In Figure 11a, the rim compositions of garnet, staurolite, and biotite from sample 91-136 are plotted on an AFM diagram projected through muscovite, quartz and H_20. For these AFM diagrams all FeO was treated as Fe^{2+} however, if the minerals contain a significant amount of Fe^{3+} then the topology of the diagrams may be altered. The crossing tie-lines indicate a possible reaction relationship between staurolite-biotite and kyanite-garnet. Although the bulk composition of many of the gneisses seem likely to control the exact reaction(s) responsible for staurolite disappearance in these rocks, the following general reaction is suggested by the above textures:

Bt + St = Grt + Als + V. (2)

The mineral zoning indicates that for the above divariant reaction assemblage (St+Ms+Qtz = Bt+Ky+V) the tie-lines migrate to more Fe rich compositions on the AFM diagram as temperature increases or until another reaction occurs, which in this system will likely propagate mineral compsitions to more XMg rich values. These divariant reactions are strictly for the KFMASH system that ignores potentially important phase components. In real rocks the actual reactions are likely to be more complex. Perhaps a better way to characterize the compositional variations and phase changes in these rocks is to integrate the chemical and textural observations. Textural observations of staurolite inclusions in kyanite and garnet (Photograph 5c) are consistent with staurolite- consuming and garnet and (or) kyanite- producing reactions. As a next step, the following continuous reaction is proposed for sample 91-136:

$St_{ss} + Bt_{ss} + Ms + Qtz = Ky + St_{ss} + Grt_{ss} + Bt_{ss} + V$ (3)

The "SS" subscript is used to indicate the Fe-Mg solid solution in these phases. Because of the extra non-KFMASH components in phases such as garnet and staurolite additional phase components may be warranted in order to adequately evaluate the reaction, specifically, Zn in staurolite; Ca and Mn in garnet; and, Mn and Ti in biotite. However, for simplicity, only the Ca component in garnet and coexisting plagioclase will be considered.

The An and Grs components were chosen because plagioclase and garnet are the only two calcium bearing phases now found in the rock and inclusion suites do not indicate that any other calcium bearing phase was previously present. Further indication for

including these components in the reaction come from garnet and plagioclase zoning. Garnet zoning profiles are largely homogenized due to volume diffusion at high temperatures (Fig. 12). This is evident in the relatively flat line profile of almandine (Alm) and pyrope (Pyp) as seen in the compositional zoning profiles. This is more apparent in the smaller garnets such as sample 92-5d (Fig. 12). However zoning is still seen preserved in the bell shaped Sps profiles and changes in the Grs content in samples 91-136 & 91-80. Relict growth zoning is weak in these samples with cores being relatively enriched in the spessartine Sps (≈5-6 mol.% Sps) component compared with 3-3.5 mol.% at the rims. In sample 91-136 and 91-80 the Grs profile steepens towards the edge from Grs=4.5-7 at the cores to 5.5-8 near the rims. This difference is within the analytical error estimated to be ± 2.2%. However as the relative errors for each successive point in the garnet profiles are similar, the overall trend of the data remains qualitatively useful. In the same rocks the grossular zoning in garnet is accompanied by weak zoning in plagioclase to more albitic rims from XAn≈ .30-.33 to .26-.30. Therefore, if the system remained closed, the garnet must have grown by addition of the anorthite component from plagioclase. Following this line of reasoning, an increase in grossular content would indicate an increase in pressure as required by the anorthite breakdown reaction:

An = Grs + Ky + Qtz. (4)

By combining the preceding information, the following reaction is proposed for rocks below the sillimanite isograd containing the assemblage (Ms + Bt + Grt + St + Ky):

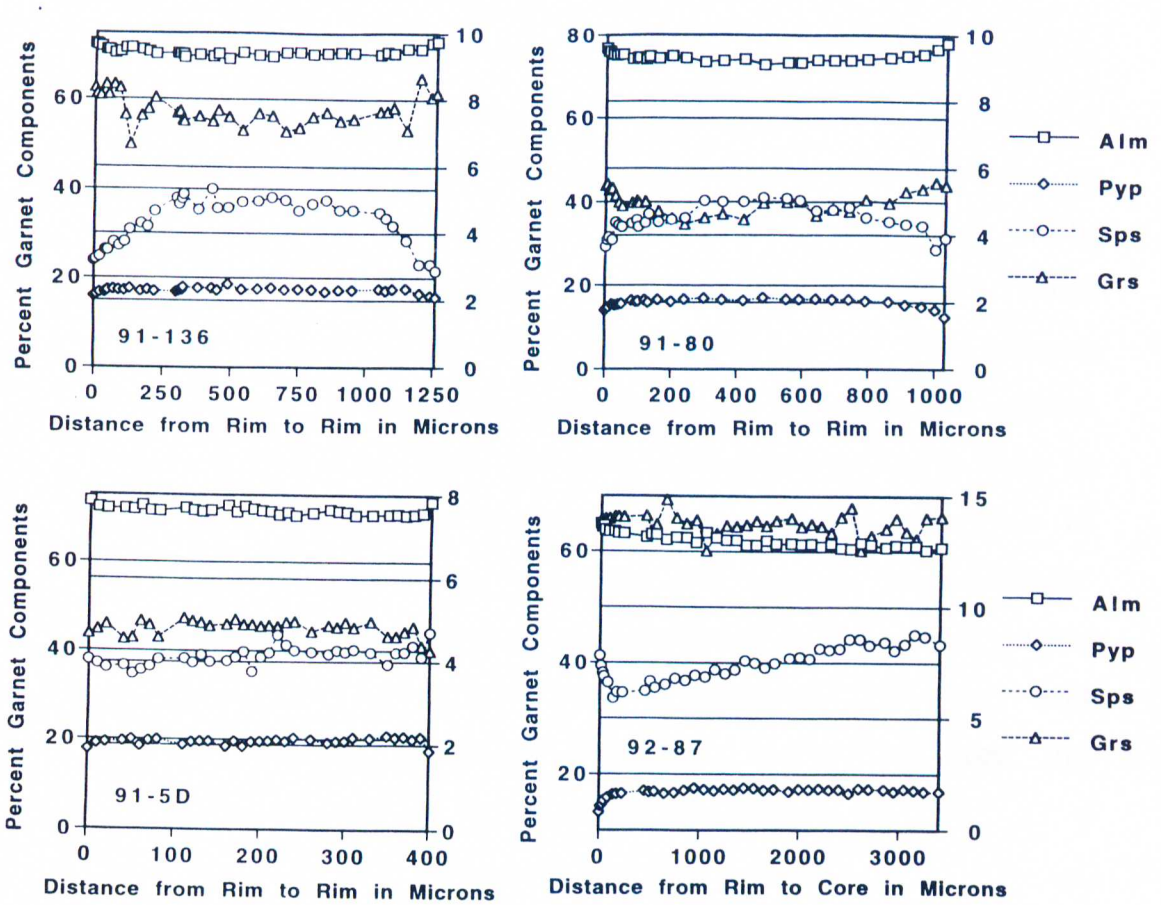

Figure 12. Garnet compositional zoning profiles from representative garnets in the Port aux Basques gneisses. Data points refer to molar percentages of Alm, Sps, Grs and Pyp. Grs and Sps plot on the right "Y" axis; Alm and Pyp plot on the left "Y" axis.

$Bt + St = Grt + Als + V.$ (2)

The mineral zoning indicates that for the above divariant reaction assemblage (St+Ms+Qtz = Bt+Ky+V) the tie-lines migrate to more Fe rich compositions on the AFM diagram as temperature increases or until another reaction occurs, which in this system will likely propagate mineral compsitions to more XMg rich values. These divariant reactions are strictly for the KFMASH system that ignores potentially important phase components. In real rocks the actual reactions are likely to be more complex. Perhaps a better way to characterize the compositional variations and phase changes in these rocks is to integrate the chemical and textural observations. Textural observations of staurolite inclusions in kyanite and garnet (Photograph 5c) are consistent with staurolite- consuming and garnet and (or) kyanite- producing reactions. As a next step, the following continuous reaction is proposed for sample 91-136:

$St_{ss} + Bt_{ss} + Ms + Qtz = Ky + St_{ss} + Grt_{ss} + Bt_{ss} + V$ (3)

The "SS" subscript is used to indicate the Fe-Mg solid solution in these phases. Because of the extra non-KFMASH components in phases such as garnet and staurolite additional phase components may be warranted in order to adequately evaluate the reaction, specifically, Zn in staurolite; Ca and Mn in garnet; and, Mn and Ti in biotite. However, for simplicity, only the Ca component in garnet and coexisting plagioclase will be considered.

The An and Grs components were chosen because plagioclase and garnet are the only two calcium bearing phases now found in the rock and inclusion suites do not indicate that any other calcium bearing phase was previously present. Further indication for

including these components in the reaction come from garnet and plagioclase zoning. Garnet zoning profiles are largely homogenized due to volume diffusion at high temperatures (Fig. 12). This is evident in the relatively flat line profile of almandine (Alm) and pyrope (Pyp) as seen in the compositional zoning profiles. This is more apparent in the smaller garnets such as sample 92-5d (Fig. 12). However zoning is still seen preserved in the bell shaped Sps profiles and changes in the Grs content in samples 91-136 & 91-80. Relict growth zoning is weak in these samples with cores being relatively enriched in the spessartine Sps (≈5-6 mol.% Sps) component compared with 3-3.5 mol.% at the rims. In sample 91-136 and 91-80 the Grs profile steepens towards the edge from Grs=4.5-7 at the cores to 5.5-8 near the rims. This difference is within the analytical error estimated to be ± 2.2%. However as the relative errors for each successive point in the garnet profiles are similar, the overall trend of the data remains qualitatively useful. In the same rocks the grossular zoning in garnet is accompanied by weak zoning in plagioclase to more albitic rims from XAn≈ .30-.33 to .26-.30. Therefore, if the system remained closed, the garnet must have grown by addition of the anorthite component from plagioclase. Following this line of reasoning, an increase in grossular content would indicate an increase in pressure as required by the anorthite breakdown reaction:

An = Grs + Ky + Qtz. (4)

By combining the preceding information, the following reaction is proposed for rocks below the sillimanite isograd containing the assemblage (Ms + Bt + Grt + St + Ky):

St_{ss} + Bt_{ss} + Pl_{ss} + Ms_{ss} + Qtz = Ky + St_{ss} + Pl_{ss} + Grt_{ss} + Bt_{ss} + V (5)

Samples 91-70 and 91-80 contain fibrolite in the rocks as well as kyanite. Staurolite in these samples occurs as ragged minerals in the matrix or as small anhedral grains as inclusions in plagioclase. Mineral compositions of the equilibria from sample 91-80 plotted on an AFM projection through muscovite, quartz and H_20 shows staurolite in a linear relationship with kyanite and garnet (Fig. 11b). This topology indicates that some staurolite should break down to garnet + kyanite. This reaction may be written as:

St + Qtz = Grt + Ky + V (6)

Farther east, staurolite is absent from the equilibrium mineral assemblage and is only seen as inclusions or armored relics surrounded by plagioclase or quartz. These observations combined with the fact that many rocks within the sillimanite zone do not contain muscovite as a stable phase of the prograde mineral assemblage indicate that an additional muscovite and staurolite consuming reaction is necessary.

Sample 92-5D occurs a few meters from the sillimanite-in isograd and lacks muscovite as part of the mineral assemblage. The staurolite in this rock occurs as small anhedral and texturally ragged grains in the matrix. The mineral assemblage in this rock is Grt + Ky + St + Bt + Pl + Qtz + Rt + Ilm. An AFM diagram was plotted for the minerals garnet, kyanite, staurolite and biotite, even though it is recognized that the absence of muscovite from the assemblage does not allow for an AFM diagram as specified by Thompson (1957) (Fig. 11c). The AFM diagram indicates the discontinuous terminal

reaction equilibria:

St = Ky + Grt + Bt (7)

in the model AFM system.

Further, it would appear from the above that many if not all of the metamorphic reactions are continuous reactions and, as only the compositions of the coexisting reaction assemblages are known in the rock and not the compositions of the original reactants and final products, balancing them is not possible or has little meaning.

An AFM diagram was constructed for sample HIC-11B and is shown in figure 11d. Note that staurolite has migrated to the Mg side of the projection and lies well within the divariant field of Grt + Bt + Sil. Reaction 7 is a likely candidate to produce this type of topology. Extra components or buffering by a fluid phase lead Rumble (1978) to term such staurolite consuming reactions as "nominally" discontinuous. Thus, I infer that additional aluminum silicate production is likely by the nominally discontinuous reaction:

St + Ms + Qtz = Grt + Bt + Als + V. (7)

Due to the presence of inclusions of rutile and garnet surrounded by kyanite in sample 92-5D & 91-70 (Photograph 7b, 7e) and the effect of extra components increasing the variance of the system, a more likely reaction for some compositions is of the form:

St + Qtz + Ms + Pl + Ilm = Grt + Rt + Als + Bt + V. (8)

Another pressure sensitive reaction (GRAIL)

Ky + Ilm + Qtz = Grt + Rt (9)

is indicated by inclusions of rutile in garnet in garnet-kyanite schists such as 91-131 and 92-71. These textures indicate that garnet growth occurred on the high pressure side of the GRAIL

reaction curve in P-T space.

Matrix rutile in many samples is rimmed by ilmenite, indicating a recrossing of the GRAIL reaction (9) late in the M_2 reaction history of these rocks.

The following polymorphic reaction is inferred to relate the kyanite zone with the lower sillimanite zone:

Ky = Sil. (10)

Evidence for reaction 10 is sillimanite directly replacing kyanite (sample 91-70, photograph 6b, and numerous others); in other places it occurs through a cycle of reactions similar to those described by Carmichael (1969) in which sillimanite occurs as inclusions in quartz, kyanite is rimmed by muscovite and sillimanite needles are embedded in biotite.

Migmatites are common in the PaBC. The discontinuous quartzo-feldspathic leucosomes in these migmatites are generally parallel to the foliation in the host rock. A small proportion of these leucosomes are deformed by F_2. Most post-date the F_2 folds but are folded by F_3. Many of the leucosome suite appear to be layer-parallel but when followed carefully some of them appear discordant to the foliation (Photograph 7d). The quartz-feldspar rich leucosomes are often rimmed by biotite rich melanosome. Some of the leucosomes are garnet bearing with thin biotite selvages or simply increased modal concentrations of garnet in the immediate vicinity of the leucosome (Photograph 2d). Photograph 3a shows a kyanite porphyroblast in leucosome accompanied by skeletal garnet. Additionally Photograph 7d shows what is interpreted as a

metatexite which may have undergone partial fusion such that the anatectic portion appears to cut across the foliation and thus has probably migrated to some degree from the original site of generation. This rock is a sillimanite + garnet + biotite-bearing gneiss which contains prismatic sillimanite within the leucocratic material. A possible melting reaction to explain this texture would be the continous net-transfer reaction:

Ms + Qtz + Pl + V = Sil + Melt. (11)

It seems possible that the melt phase could additionally become saturated with respect to garnet and garnet precipitate from the melt, thereby accounting for other observed textures featuring garnet in the leucosome. Alternatively the garnet could be residual but morphologic differences in garnets from leucosome areas and garnet from paleosome areas argue against a residual origin.

The model reaction (11) in the KFMASH system was discussed by Thompson and Tracy (1979); it has a steep positive slope with a minimum temperature for the albite endmember reaction in the sillimanite field of around 650°C at 7-kbar pressure. However, the addition of the anorthite component will raise the reaction curve to higher temperatures of *c.* 720° at 8 kbar (Thompson and Tracy, 1979). Both the Alb and An endmember reaction curves are presented in figure 10.

The highest grade rocks (Sil + Grt + Bt + Kfs-bearing assemblages) occur near Margaree where they occur dominantly as stromatic migmatites with granitic mineralogy in the leucosomes. These rocks are interpreted to have undergone partial fusion (Photograph 7e). It was not possible to map a K-feldspar isograd due

to the scarcity of appropriate lithologies in the region. Muscovite is absent from these rocks as a prograde mineral and was possibly completely exhausted by the K-feldspar producing reaction:

Ms + Qtz = Sil + Kfs + Melt. (12)

Bulk rock composition and previous muscovite consumption reactions also likely contribute to the lack of muscovite in these rocks.

This incongruent melt producing reaction (12) is preferred over the vapor producing dehydration reaction to produce Sil + Kfs because of the probable melt forming reactions occurring before the second sillimanite "isograd", such as reaction (11) above. Additionally, pressure conditions as constrained by the petrogenetic grid and geobarometry (present later) indicate that the rocks were above the invariant point where the granitic solidus intersects the dehydration melting curve therby producing liquid instead of vapor.

The Sil + Kfs + Grt + Bt bearing assemblages in metapelites are restricted to the area around Margaree and Fox Roost. As noted in chapter one, this area is almost solely composed of migmatitic gneisses. The presence of Cpx + Spl assemblages in the metaultramafic rocks, the Sil + Kfs + Grt + Bt bearing assemblages and the omnipresent migmatites suggest that this area has experienced the highest degree of thermal metamorphism.

Retrograde Reactions in the Metapelites

Retrograde reactions in metapelites involve the replacement of biotite by chlorite and of garnet by a combination of chlorite and biotite. Sillimanite, kyanite and staurolite are replaced by aggregates or laths of white mica and quartz. Photo 3b shows an

epidosite nodule within an amphibolite. Such evidence of fluid infiltration after the thermal metamorphic maximum accounts for much of the retrogression seen in these rocks. The following three general reactions account for these textures:

$$Als + K^+ + V = Ms + Qtz \quad (13)$$

$$Als + Bt + V = Ms + Chl \quad (14)$$

$$Grt + V = Chl + Qtz. \quad (15)$$

The introduction of fluids containing ionic species such as K^+ in the above reactions seems justified in light of the observed retrogression likely brought on by fluid infiltration through the outcrops.

Reactions in the Amphibolites and Calc-silicates

Most amphibolites in the area contain the assemblage Hbl + Pl + Qtz ± Ortho-Amp ± Grt ± Bt ± Cpx ± Ttn ± Ilm ± Rt. Due to the large number of components and the relatively small number of phases, specific reactions to produce the observed assemblage in these rocks proves very difficult.

Some information may be gleamed from sample 91-168. This sample contains the assemblage Hbl + Pl + Qtz + Chl. Epidote relics in this sample may indicate a model continuous reaction of the form:

$$Chl + Ep + Qtz = Amp + (An)Pl + V \quad (16).$$

The albitic plagioclase component in this reaction was ignored, however the calcic plagioclase produced may combine with albite to produce oligoclase (Yardley, 1989).

Amphibolites of the GBC usually do not contain garnet except at the edges of rocks types. These amphibolitic margins are in contact with either metapelitic schists or gneisses. The marginal

area on the amphibolitic side often forms an area (cm scale across the zone) of large dark purple garnet porphyroblasts. This suggests that these amphibolites are too Al poor to produce garnet, however small scale element mobility does exist allowing transfer of the appropriate elements to produce the garnet.

The appearance of clinopyroxene in amphibolites is limited to samples with high CaO values, no attempt was made to model its formation; however, Grt + Cpx assemblages were studied in sample 91-84 (Photograph 7f). In this specimen titanite is seen rimmed by ilmenite. Clinopyroxene in this sample has an area of hornblende depletion around it. Clinopyroxene + garnet in these rocks may appear by the generalized reaction:

Hbl + Ttn = Cpx + Grt + Ilm + Pl + Qtz. (17)

The actual reaction (s) for the production of clinopyroxene in these rocks is likely more complex and heavily dependent on bulk rock composition.

Many amphibolites of the GBC are mylonitized and are retrogressed to assemblages containing blue-green hornblende + epidote + chlorite + calcite + plagioclase + quartz, which may represent a reversal of reaction 16, or:

Hbl + Pl + V (CO_2 + H_2O) = Cc + Chl + Ep. (18)

Calc-silicate rocks are more common in the HICG, occurring in metasandstones and in amphibolites. They contain a complex and variable mineralogy of Hbl + Grt + Pl + Qtz ± Di ± Kfs ± Ttn ± Cc ± Zo ± Bt. The mineralogy observed is consistent with the highest grade zones mapped by Kennedy (1949). Near Isle aux Morts, the rocks typically contain biotite but lack this phase farther east. Specific

reactions for these rocks was not attempted because of the possibility that the changes in phase assemblage are likely in part due to differences in bulk rock chemistry, that is suggested by the different modes of occurrence of these rocks.

In many calc-silicates, clinopyroxene occurs as a porphyroblast in the matrix in and is inferred to formed by breakdown of amphibole. However, in samples GB-8 and GB-6 some clinopyroxene is now replaced by green hornblende. Additionally, some clinopyroxene in these rocks has developed corona textures of garnet rimming clinopyroxene. Moreover, the garnets in these samples display post-D_2 growth textures such as inclusion trails which fully overgrow the main foliation which in this case is S_2.

Conditions of Metamorphism

Variation of temperatures and pressures across the present erosional surface may be estimated by the different combination of phase assemblages, geothermobarometric data and/or field evidence (such as the development of migmatites which are interpreted to represent both metamorphic segregations and partial melts). Figure 10 shows a petrogenetic grid detailing relevant reactions for metapelites of the Port aux Basques Gneisses.

Petrogenetic Grid

GBC metapelites are sparse but usually contain Grt + Ms + Bt ± Ky ± St -bearing assemblages. In addition to these minerals all assemblages contain Qtz, Pl, Ap, Zrn, ± Chl ± Tur ± Ilm ± Rt ± Hem ± Py ± Ccp. A distinctive rock, which may represent a high-Ca metapelitic or a hydrothermally altered metamafic unit, contains

the assemblage Ky + Hbl + St + Bt + Qtz + Pl with chlorite and white mica (Photograph 8a). Locally garnet also occurs in this rocks but has not been seen in direct contact with both hornblende and kyanite. This metapelite assemblage has been attributed to relatively high pressures of 6-8 kbar (Selverstone et al. 1984; Thompson and LeClair, 1987). Amphibolites of the GBC contain blue-green Hbl + Pl + Qtz + Ttn ± Grt ± Rt ± Ilm. The presence of rutile and clinopyroxene in some of the amphibolites also indicates elevated pressures (Photograph 8b). Chloritoid is absent in the equilibrium assemblage or as a relict inclusion in the metapelites and as such the rocks are assumed to have achieved temperatures sufficient for the breakdown of this mineral. Chloritoid does require a specific bulk rock compostion for its formation, however, a wide range of pelitic compositions exist in the Port aux Basques gneisses and chloritoid has never been observed. Small amounts of chlorite are present in these rocks as inclusions in garnets or in the matrix. The chlorite is believed to be either part of a retrograde assemblage or an isolated two-phase inclusion assemblage. There is no evidence for partial melting in any lithology in the GBC. This implies that if a water-rich fluid phase was present, conditions must have been on the low temperature side of the fluid-phase present granite/metapelite solidus. Using the petrogenetic grid of Spear and Cheney (1989) to evaluate temperatures for the breakdown of chloritoid and chlorite, temperatures in the range of 550-650°C are suggested for the GBC at pressures of 6-8 kbar.

Leucosome/melanosome pairs locally occur throughout the PaBC, in contrast to the GBC, even though the actual development of

the neosomes is sporadic in the complex. Leucosomes throughout the PaBC and the HICG commonly form discontinuous layers 1-5cm thick and 5-20cm in length. These leucosomes may contain garnets and locally aluminum silicate in the leucosome and are surrounded by mafic mineral selvedges. Small (meter scale), garnet-bearing deformed granitoids are present in the kyanite zone and contain disrupted blocks of country rock containing the S_2 fabric. The fact that many of these migmatitic rocks do not contain closely spaced planar or geometric leucosome relationships, are generally not pegmatitic, often contain igneous textures and mineralogy and are in some cases accompanied by rotation of country rock blocks (agmatites) suggests that some of these migmatites are the result of anatexis. The sporadic natures of these mobilizates suggests that the development of melting was likely controlled by the amount of available water. Leucosomes are also seen associated with small scale shear zones (Photograph 2a). These types of migmatites could have formed by metamorphic segregation, injection or anatexis.

A qualitative indication of changing metamorphic conditions is obtained by the change in hornblende and biotite pleochroism, the development of sillimanite + K-feldspar-bearing assemblages in the eastern MC and the presence of high temperature calc-silicates in the HICG. The Sil + Kfs + Grt + Bt bearing assemblages are restricted to the area around Margaree and Fox Roost. As noted in Chapter one, this area is almost solely composed of migmatitic gneisses and granites. The muscovite dehydration reaction to produce Sil + Kfs + L requires temperatures in excess of 700°C at

moderate pressures. Therefore it is concluded that the MC has experienced the highest degree of metamorphism in the area.

Phase assemblages within the PaBC, discussed in the previous section, can be used to indicate qualitative estimates of pressures and temperatures for the complex. To summarize, the western portion of the region contains kyanite and has not reached the staurolite-out reaction (4), whereas rocks in the eastern part of the PaBC and HICG have sillimanite as the stable aluminum silicate and must have reached or exceeded the staurolite breakdown reaction (5). In addition, amphibolitic rocks associated with sillimanite grade rocks locally contain the assemblage Grt + Cpx + Qtz + Pl + Hbl which is generally indicative of medium to higher pressures (> 6kbar) (Bégin 1992; Yardley 1989). Metamorphism in these rocks has exceeded the stability limit of St + Qtz and Ms + Qtz and suggests conditions appropriate for melting reactions such as (11). All of the above information indicates that P and T conditions responsible for "peak" M_2 phase assemblages and migmatites are in the range of 700-750°C at 8-9 kbar.

The preceding P-T estimates were derived from rocks which record limited D_3 deformation. Thus the estimates apply to peak through post-peak M_2 metamorphism. As stated earlier, M_3 was retrogressive with respect to M_2; however, peak conditions for M_3 can be estimated from a variety of direct and indirect means. Partial melting associated with M_2 did not extend into M_3 and no anatexis at all is associated with M_3 and therefore conditions must have been maintained below the wet granite melting curve.

However, the rocks are still in the sillimanite stability field during early M_3, and this period was characterized by the recrystallization of hornblende in basic rocks and recrystallization of both muscovite and biotite in metapelitic rocks. Although reaction kinetics may not have been favorable for porphyroblast growth during M_3, the absence of andalusite or cordierite in any assemblage or late veins may suggest P-T conditions out of their stability fields. The best estimate for peak M_3 conditions is around 550°C at 4-6 kbar. This thermal estimate is likely to vary across the area to generally lower temperatures.

Geothermobarometry

Quantitative P-T estimates may be obtained from geothermobarometry. The composition of phase assemblages in appropriate samples can be used to estimate equilibrium temperatures and pressures from a variety of exchange and net-transfer reactions. Phase compositions for geothermobarometry can be found in Appendix 2, part A. The following exchange equilibria were used for estimating peak to post-peak temperatures.

$$FeMg_{-1\ Grt} = FeMg_{-1\ Bt} \quad (19)$$

$$FeMg_{-1\ Grt} = FeMg_{-1\ St} \quad (20)$$

$$FeMg_{-1\ Grt} = FeMg_{-1\ Cpx} \quad (21)$$

$$FeMg_{-1\ Grt} = FeMg_{-1\ Hbl} \quad (22)$$

As seen above, preference is given to exchange thermometers involving a refractory phase such as garnet. Unfortunately Fe-Mg exchange commonly exists at temperatures down to 500°C allowing resetting during retrogression which casts doubt on the reliability

of garnet-biotite thermometry producing temperatures appropriate for the peak thermal conditions of these gneisses.

The garnet-biotite thermometer calibrations used were those of Ferry and Spear (1978) and Perchuk and Lavrent'eva (1984). Garnet-staurolite thermometry was obtained using the calibration of Perchuk (1991). Garnet-clinopyroxene thermometry was based on the calibrations of Ellis and Green (1979) and Powell (1985). Garnet-hornblende thermometry was based on the calibrations of Graham and Powell (1984) and Perchuk et al. (1985). Thermobarometric data are presented in tables 2 and 3. All temperatures quoted are for rim compositions except where otherwise noted. These data are generally in agreement with estimates from the petrogenetic grid constraints discussed above, especially bearing in mind that the higher calculated T and P more likely reflect peak conditions.

Sample 91-167, a mylonitic schist from the GBC, yields temperatures between 550-600°C using the garnet-biotite thermometer for rim compositions. This is in agreement with earlier estimates for peak metamorphic conditions for the GBC. For kyanite zone rocks such as sample 91-137 of the PaBC, the garnet-biotite thermometer yields temperatures in the range of 650-700°C at 7-9 kbar for rim compositions. Temperatures around 700°C are also indicated by garnet-staurolite thermometry from sample 92-5D.

Sample HLC-11B is from the sillimanite zone and contains relict staurolite. The staurolite contains around 1.5% ZnO. This is higher than any of the ZnO contents in staurolite prohyroblasts suggesting concentration of Zn into the staurolite with increasing

staurolite consumption. It is recognized that the mineral composition preserved in the staurolite was probably never in equilibrium with the rim composition of the garnet. This statement equally applies to equilibrium between the core of the garnet and the relict staurolite. However, There was likely a point during the growth of the garnet when it and the staurolite where in equilibrium. As this precise point cannot be determined, calculated temperatures between staurolite and garnet core and rim compositions were determined. This temperature range is a best estimate for obtaining a meaningful garnet-staurolite "peak" temperature. This thermometer recorded a temperature of around 690°C for core compositions which is consistent with other observations. Garnet-biotite thermometry from sample 91-80 records temperatures around 650°C at 8 kbar. Garnet-staurolite thermometry from this rock yields temperatures of *c.* 710°C. However, generally thermobarometry in the sillimanite grade rocks poses a difficult problem due to more extensive retrogression experienced by the higher grade rocks. For example, PaB91-70 is from the sillimanite zone in an area of penetrative D_3 structures and records temperatures of around 600°C using the garnet-biotite and garnet-staurolite thermometers. This inconsistency is attributed to late-stage re-equilibration of phases after the M_2 thermal maximum. These lower temperatures may also be related in part to the M_3 recrystallization of mica. Sample HLC-11B corroborates this with garnet-biotite temperatures of *c.* 515-550°C. Therefore, to estimate peak M_2 P-T conditions in the higher grade rocks it is necessary to

use data obtained from amphibolites or calc-silicate rocks in low D_3 strain areas. Garnet-hornblende thermometry (Graham and Powell,1984) consistently yields temperatures in the range of 650-750°C. The upper range of these temperatures is inconsistent with the mineralogy of these rocks; this may be due problems with the assumptions of ideal mixing in the solution models on which the geothermometers are based, and in the assumption that all the iron in the phases are Fe^{2+}. Schumacher (1991) states that if both garnet and biotite contain ferric iron then the errors produced by neglecting the iron tend to cancel one another out, he recommended that for Fe-Mg exchange the best results are obtained using an all-ferrous formula for both minerals. This advice will be followed here.

Garnet-clinopyroxene thermometry using rim compositions yields temperatures of around 700 ± 50°C at 8 kbar. Sample 91-84 illustrates the relationship between the clinopyroxene, garnet and the host rock (Photograph 7f). These data likely represent thermal conditions during the "peak" of M_2. Garnet-hornblende thermometry records temperatures of *c.* 620-650°C.

Solid-solid reactions were preferred for geobarometry because their position in P-T space is not dependent on the presence or composition of a fluid phase. Net-transfer reactions based on the following equilibria were used for geobarometry:

Grt + Qtz = Pl + Di (23)

An = Grs + Ky + Qtz (24)

Grt + Ms = Bt + Als (25)

Grt + Rt = Ilm + Als + Qtz (26)

Garnet-plagioclase-clinopyroxene-quartz barometry using the calibration of Powell and Holland (1988) and Newton and Perkins (1982) yields *c.* 8 kbar at the above temperatures. Garnet-plagioclase-aluminum silicate-quartz (GASP) barometry using the calibrations of Hodges and Crowley (1985), Hodges and Spear (1982) and Koziol (1989) yields *c* 6.8-10.6 kbar at the range of above temperatures. The albitic nature of the plagioclase and generally low grossular content of the garnets from metapelitic samples probably account for the wide range in pressures using the different GASP barometers. Three samples were appropriate for using the Garnet-biotite-muscovite-aluminum silicate barometer of Holdaway et al. (1988). These samples yielded pressures of 7.4 to 8.8 kbar at 700°C. GRAIL barometry using the calibration of Bohlen et al. (1983) yields pressures of *c.* 8 kbar at the above temperatures. Statistical analysis on the uncertainty of these calculations was not done. However, an extensive treatment of uncertainties in geothermobarometry was presented by Kohn and Spear (1991). Following their work for statistical errors using the above calibrations, the uncertainties associated with the above calculations are ±50°C and 1 kbar.

From the petrogeneitic grid and from thermobarometry peak M_2 conditions are on the order of 700-750°C at 8-9 kbar. The source of the metamorphism is interpreted to be related to tectonic thickening during D_2 with subsequent thermal relaxation. The higher pressures indicated by the petrogenetic grid are consistent with

Table 2 Geothermobarometric Data

Samples are listed geographically from west to east
Thermometric calculations were made with reference to a fixed nominal pressure
The calculated temperatures listed are subject to uncertainties of +/- 50 degrees celsius

Garnet-Biotite Thermometry (Rim Data)

Nominal Pressure = 8 kbar

Sample	Ferry & Spear (1978) T(C)	Perchuk & Lavrent'eva (1984) T(C)	Phase Assemblages
91/167A	558	582	Grt+Ep+Bt+Ms+Pl+Qtz+Opaques
91/136	742	674	Grt+St+Ky+Ms+Bt+Pl+Qtz+Opaques
91/70	605	608	Grt+Bt+Ms+Pl+Qtz+Rt+Ilm (St)
92/5D	624	613	Grt+Ky+St+Bt+Pl+Qtz+Rt+Ilm
91/80	647	625	Grt+Sil+(Ky)+St+Bt+Ms+Pl+Qtz+Opaques*
HLC-11B	515	552	Grt+Sil+Bt+Pl+Qtz+Ilm (St)

Garnet-Staurolite Thermometry (Rim (R) & Core (C) Data)

Nominal Pressure = 8 kbar

Sample	Perchuk (1991) T(C)	
91/136	868	Grt+St+Ky+Ms+Bt+Pl+Qtz+Opaques
91/70/R	627	Grt+Bt+Ms+Pl+Qtz+Rt+Ilm (St)
91/70/C	659	Grt+Bt+Ms+Pl+Qtz+Rt+Ilm (St)
92/5D/C	706	Grt+Ky+St+Bt+Pl+Qtz+Rt+Ilm
92/5D/R	794	Grt+Ky+St+Bt+Pl+Qtz+Rt+Ilm
91/80	711	Grt+Sil+(Ky)+St+Bt+Ms+Pl+Qtz+Opaques
HLC/11B/C	689	Grt+Sil+Bt+Pl+Qtz+Ilm (St)
HLC/11B/R	555	Grt+Sil+Bt+Pl+Qtz+Ilm (St)

Table 2 Continued

Garnet-Hornblende Thermometry (Rim Data)

Graham & Powell (1984) Perchuk et al. (1985)

Nominal Pressure = 8 kbar

Sample	T(C)	T(C)	
92/87	656	632	Grt+Hbl+Bt+Pl+Qtz+Ilm
92/97	650	655	Grt+Hbl+Bt+Pl+Qtz+Ilm
91/84	744	591	Grt+Hbl+Cpx+Pl+Qtz+Tnt+Ilm
91/176	730	597	Grt+Hbl+Pl+Tnt+Bt+Cpx+Qtz

Garnet-Clinopyroxene Thermometry (Rim & Core Data)

Nominal Pressure = 8 kbar

Ellis & Green (1979) Powell (1985)

Sample	T(C)	T(C)	
91/84/C	760	746	Grt+Hbl+Cpx+Pl+Qtz+Tnt+Ilm
91/84/R	693	676	Grt+Hbl+Cpx+Pl+Qtz+Tnt+Ilm
GB/8/C	636	620	Grt+Cpx+Hbl+Tnt+Cc+Pl+Qtz
GB/8/R	664	648	Grt+Cpx+Hbl+Tnt+Cc+Pl+Qtz

*Those phases in () are inclusions or otherwise not part of the equilibrium assemblage

Table 3 Geothermobarometric Data

Samples are listed geographically from west to east

Barometric calculations were made with reference to a fixed temperature

The calculated pressures are subject to uncertainties of +/- 1 kbar

Sample	T(C)	GRAIL	GPCQ (a)	GPCQ (b)	GASP (a)	GASP (b)	GASP (c)	GBMA
91/136	700				10.6	9.9	8.8	7.4
91/70	700				9.7	6.8	6.6	8.8
92/5D	700	8.2			8.6	7.5	6.5	
92/5D-C	700	7.7						
91/80	700				8.6	7.4	6.8	7.9
91/84	700		8.3	8.8				
HLC/11B	700				6.4	5.2	6.2	
GB/8	700		10.6	6.6				

Sample	Phase Assemblage
91/136	Grt+St+Ky+Ms+Bt+Pl+Qtz+Opaques
91/70	Grt+Bt+Ms+Pl+Qtz+Rt+Ilm (St)*
92/5D	Grt+Ky+St+Bt+Pl+Qtz+Rt+Ilm
92/5D-C	Grt+Ky+St+Bt+Pl+Qtz+Rt+Ilm
91/80	Grt+Sil+(Ky)+St+Bt+Ms+Pl+Qtz+Opaques
91/84	Grt+Hbl+Cpx+Pl+Qtz+Tnt+Ilm
HLC/11B	Grt+Sil+Bt+Pl+Qtz+Ilm (St)
GB/8	Grt+Cpx+Hbl+Tnt+Cc+Pl+Qtz

*Those phases in () are inclusions or otherwise not part of the equilibrium assemblage

GRAIL-Bohlen et al., 1983

GPCQ (a)-Powell, 1985

GPCQ (b)- Newton & Perkins, 1982

GASP (a)- Koziol, 1989

GASP (b)-Hodges & Crowley, 1985

GASP (c)-Hodges & Spear, 1982

GBMA-Holdaway et al., 1988

this. There is no evidence for heating from a magmatic source. The Port aux Basques granite was intruded during D_1 and evidence presented here argues for the metamorphic peak during D_2. The M_2 metamorphism does not display any relationship to the granite. In fact, metamorphic grade increases with increasing distance away for the granite on the southeastern side. Thus, thickening of the crust is a reasonable means of achieving the metamorphic conditions indicated by the Port aux Basques gneisses.

Chapter Summary

Metamorphic evidence presented in Chapter 3 indicates that the Port aux Basques gneisses were variably metamorphosed to amphibolite facies conditions. In that the WPG and Bay du Nord Group are at greenschist facies (Brown, 1977), higher grades of metamorphism occur in the GBC than WPG, the PaBC than the GBC, the HICG than the PaBC and the HICG than the Bay du Nord Group. The timing of initial juxtaposition of the divisions is unknown, however, the earliest movement recognized is late D_2 overthrusting.

Analysis of porphyroblast-matrix relationships indicate that the minerals characteristic of peak metamorphism grew syn-deformationally during D_2. Vapor present melting initiated in the kyanite zone and culminated with the muscovite-out dehydration melting reaction and the development of sillimanite + alkali feldspar bearing assemblages. Estimates from a petrogenetic grid combined with geothermobarometry indicate temperatures of *c.* 700-750°C at 8-9 kbar. The kyanite to sillimanite transition and the D_2

structures which suggest overthrusting, are interpreted to represent a clockwise trajectory in P-T space.

Timing of Metamorphism and Deformation

Geochronology

The ages of deformation and metamorphism for the Port aux Basques Gneisses are poorly constrained. K-Ar dates of 415 and 400 ± 20 Ma were reported for muscovite within late pegmatite by Lowdon et al. (1962) and Wanless et al. (1965). Additionally, a 412 ± 2 Ma date (U-Pb on titanite) was reported from a northern portion of the Port aux Basques Gneisses from an amphibolitic unit (Dunning et al., 1990a). The significance of these isotopic dates is difficult to evaluate without microstructural constraints and consideration of closure temperatures (T_c) of the dated mineral in the isotopic system of interest. The closure temperature (T_c) is defined as "the temperature the mineral experienced at the time given by its age" (Dodson 1973). The closure temperature of a mineral is influenced by several factors such as pressure, crystal chemistry, structural state and abundant dislocations, but most researchers agree that the prevalent factor is the rate at which the rocks cool (Cliff 1985). The following is a list of the minerals to be used in this study and their presumed closure temperatures from various authors.

MINERAL	TEMPERATURE (°C)	REFERENCES
Titanite (U-Pb)	*c.* 600-650	Cliff & Cohen 1980
		Mezger, K. 1994
		Mezger et al. 1991
		Mezger et al. 1993
Hornblende (Ar)	*c.* 500	Harrison, 1981
		Mezger et al. 1993

Muscovite (Ar) *c.* 350-400 Purdy & Jäger,1976
Cliff & Cohen, 1980

U-Pb analysis

The U-Pb system may yield high precision ages with uncertainties between .1 and .5%. Two isotopes of uranium ultimately decay to two isotopes of lead. By analyzing for U and Pb abundance and Pb isotopic compositions, we obtain two independent geochronometers which will be concordant, provided that all the criteria for dating has been met (see Faure 1986). The decay of ^{238}U to ^{206}Pb as a function of time are given as:

$^{206}Pb^*/^{238}U = (e^{yt}-1)$

The decay of ^{235}U to ^{207}Pb is given as:

$^{207}Pb^*/^{235}U = (e^{yt} -1)$

Where $^{206}Pb^*/^{238}U = {}^{206}Pb/^{204}Pb - (^{206}Pb/^{204}Pb)i/(^{238}U/^{204}Pb)$ and $(^{206}Pb/^{204}Pb)i$ is equal to the amount of common lead initially incorporated into the phase, i.e. that which is not radiogenic.

The age equations are of the typical form where the initial ratio of daughter (^{207}Pb or ^{206}Pb) to stable reference isotope (^{204}Pb) plus the parent (^{238}U or ^{235}U) to reference ratio times the first order decay equation (e^{yt} - 1) results in the equations above. Here y is the decay constant and t is the time elapsed since closure of the mineral to U, Pb and all intermediate daughter products. Since ^{235}U and ^{238}U have different decay schemes, two independent ages can be calculated. These two ages may be plotted on a U-Pb concordia diagram. If the system remained closed, the crystallization age of the crystal will reside on the concordia. However, if the system became open with respect to the parent or daughter, then the system

moves off the concordia. In many cases, the system does not always remain closed. This loss or gain of U or Pb can be minimized by calculating a date based on the $^{207}Pb/^{206}Pb$ ratio, since Pb isotopes are not fractionated under normal crustal conditions. The simplified "207-206" age equation is:

$(^{207}Pb/^{206}Pb)^* = {}^{235}U/^{238}U\ (e^{y235} - 1/\ e^{y238} - 1)$ where $(^{207}Pb/^{206}Pb)^*$ is the ratio of radiogenic ^{207}Pb to radiogenic ^{206}Pb.

A U-Pb age for titanite separated from a calc-silicate (GB-8) has been determined in the present study. Analytical methods are described in Appendix 4. For sample location see figure 13. The mineralogy of the sample assemblage is indicative of the high grade M_2 event, as discussed earlier. Photograph 8c illustrates the relationship between the idioblastic to subidioblastic titanite and the host rock. The sample is from the hinge zone of a large F_3 fold and displays a relatively minor D_3 overprint. Titanite grains in the sample are large (5-10mm in the long dimension), light brown and translucent. The titanite fraction yielded a $^{207}Pb/^{206}Pb$ date of 417 ± 10Ma. The $^{206}Pb/^{238}U$ and $^{207}Pb/^{235}U$ dates are 424 Ma and 423 Ma, respectively (Table 4). The common lead correction was obtained from coexisting calcite in the sample. The above age equations can be used to create a concordia diagram with the $^{206}Pb/^{238}U$ ratio on the ordinate and the $^{207}Pb/^{235}U$ ratio on the abscissa. The basic age equations can be used to plot points which are numerical values of the radiogenic $^{207}Pb/^{206}Pb$ ratio as a function of age. The locus of these points define the concordia. Therefore, the age of a system at any time after its formation is indicated by its location on the

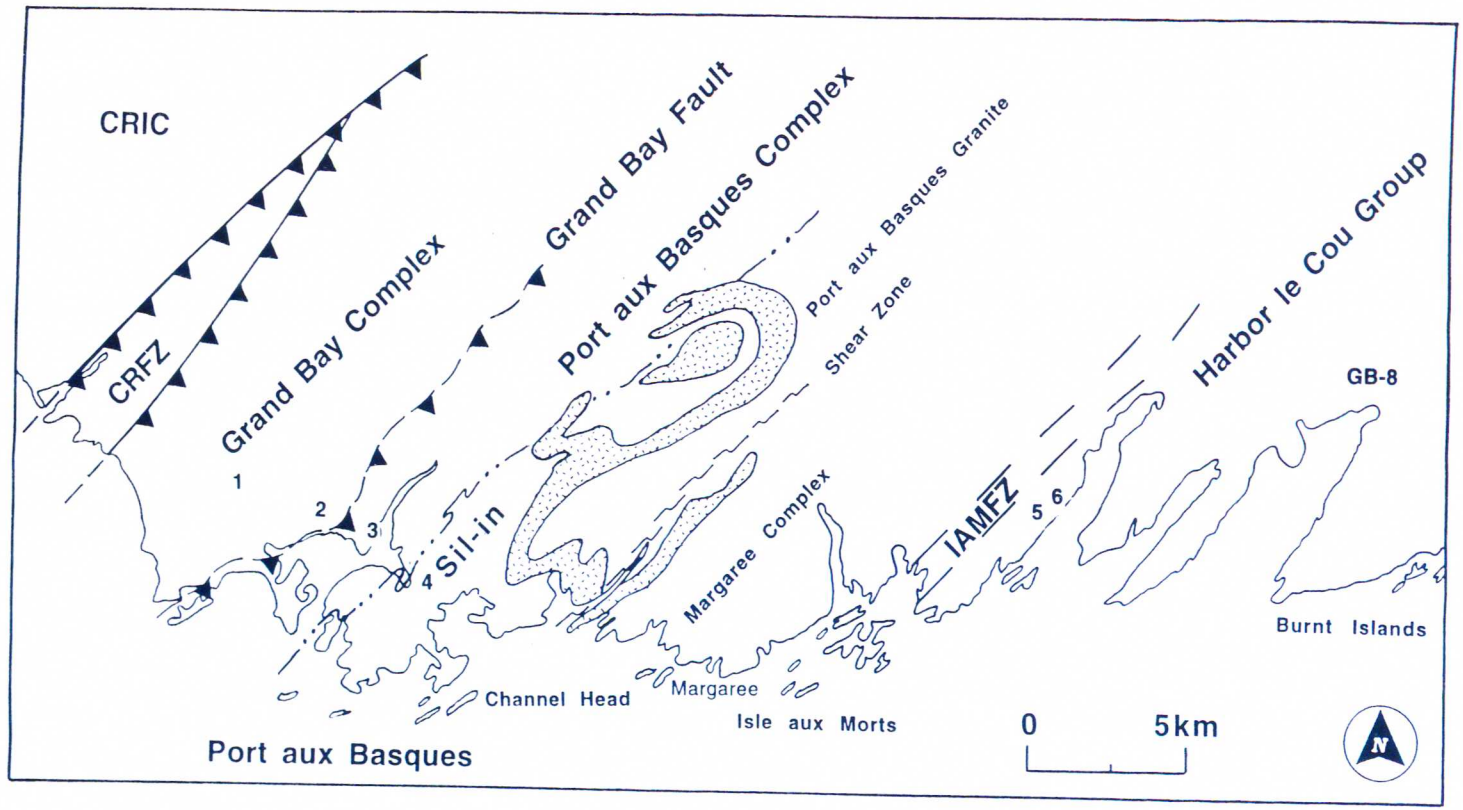

Figure 13. Local geologic map of the Port aux Basques area and the surrounding Port aux Basques Gneisses. Numbers refer to sample locations used in geochronology. Stippled unit is the Port aux Basques Granite. CRFZ is Cape Ray Fault Zone; IAMFZ is Isle aux Morts Fault Zone;CRIC is Cape Ray Igneous Complex; the dash-dot-dot line is the Sillimanite-in (Sil-in) isograd.

Table 4. Isotopic ratios obtained from titanite.

Concentrations

Sample	Weight (mg)	U (ppm)	Pb (ppm)	Common Pb (ng)
PaB-GB8 (Titanite)	2.15	58.8	5.5	1.3

Atomic Ratios

$^{206}Pb/^{204}Pb$	$^{207}Pb/^{204}Pb$	$^{208}Pb/^{204}Pb$	$^{207}Pb/^{206}Pb$	$^{206}Pb/^{238}U$	$^{207}Pb/^{235}U$
229.6	27.319	78.455	0.05511	0.0681	0.5174

Ages (Ma)

$^{206}Pb/^{238}U$	$^{207}Pb/^{235}U$	$^{207}Pb/^{206}Pb$
425	423	417

Calcite isotopic compositions for Pb

Sample	Weight (mg)	$^{206}Pb/^{204}Pb$	$^{207}Pb/^{204}Pb$	$^{208}Pb/^{204}Pb$
PaB-GB-8 (Calcite)	15.2	18.386	15.69	38.305

"The ratios above have been corrected for blank, common Pb and mass fractionation effects."

concordia curve (Faure, 1986). The resultant titanite ratios lie slightly above concordia (Fig. 14) All of these ages are older than but consistent with the 412 Ma date reported by Dunning et al. (1990a). These dates are interpreted to represent the time at which the titanite passed through its appropriate closure temperature for the U-Pb isotopic system. Titanite of this size in a slowly cooled terrain appears to have a Tc >600°C (Mezger et al., 1991; Mezger et al., 1993; Mezger, 1994). More rapidly cooled terrains would require a higher Tc. The relatively high Tc suggests that this date probably represents cooling shortly after the peak M_2 event.

$^{40}Ar/^{39}Ar$ analyses

Ar/Ar dating relies upon the formation of ^{39}Ar in the sample by irradiation of K-bearing minerals in a nuclear reactor. The minerals in this case are hornblende and muscovite. The methods for $^{40}Ar/^{39}Ar$ are discussed in Faure, 1986 and references therein.

The following is a simplified age equation to solve for time:

$t = 1/y \ln (^{40}Ar/^{39}Ar\ J + 1)$ where J is a substitution for the complex term:

$J = (e^{yt} - 1)/(^{40}Ar/^{39}Ar)$ and the value of J is calculated using the $^{40}Ar/^{39}Ar$ ratio of a flux monitor. The flux monitor is a sample of known age which is irradiated with the unknown sample. For the calculated age equation above, it is assumed that all of the Ar^{40} in the irradiated sample is either radiogenic or atmospheric. Other caveats include that all of the ^{36}Ar in the sample is atmospheric and that Ar^{39} is only produced decay of ^{39}K. If these assumptions are reasonable then the radiogenic $^{40}Ar/^{39}Ar$ ratio is given by:

$^{40}Ar/^{39}Ar = (^{40}Ar/^{39}Ar\ (measured)) - 295.5\ (^{36}Ar/^{39}Ar)$ where

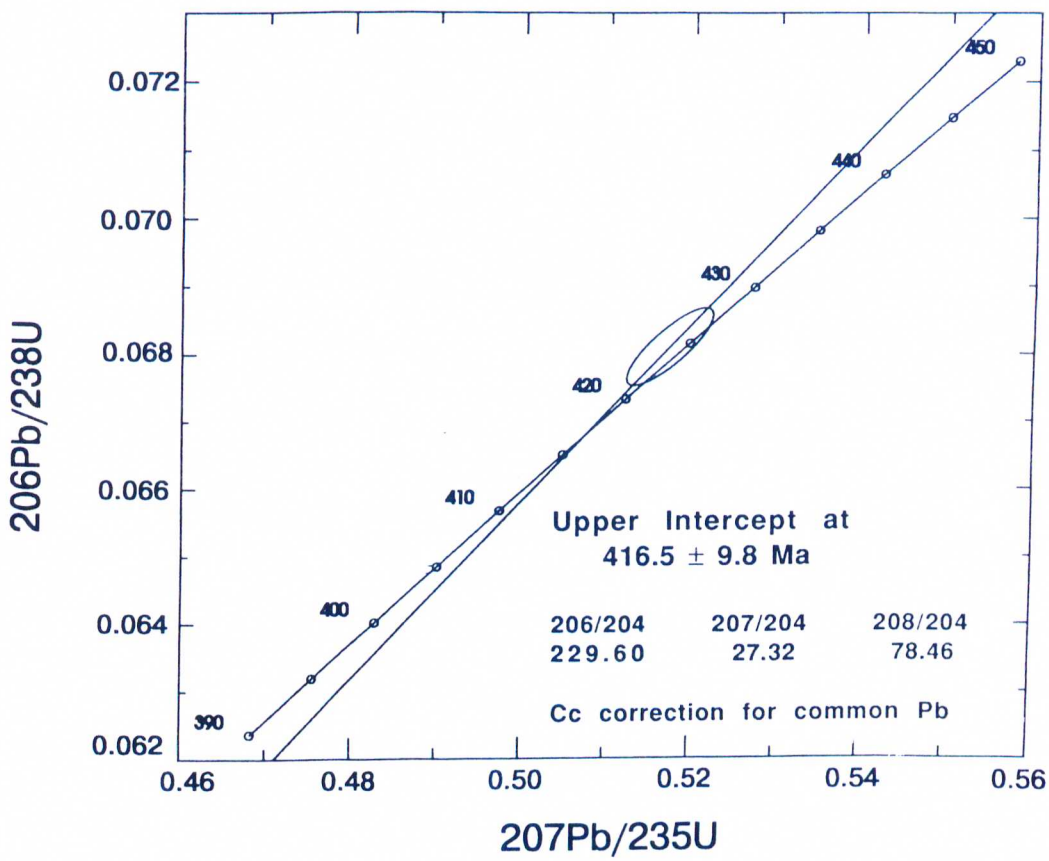

Figure 14. U-Pb concordia diagram for titanite from sample GB-8. Also given are the Pb isotopic ratios for calcite which were used to correct for common lead in the age analysis.

295.5 is the value of atmospheric argon. The value of 295.5 for atmospheric argon has been contested in the literature, therefore isotope correlation ages (discussed later) are preferred.

The above section discusses how an age can be calculated solely on the basis of the $^{40}Ar/^{39}Ar$ ratio of a neutron irradiated sample. The incremental heating technique allows the attainment of a series of dates to be calculated from a single sample as it is being heated up and evolving argon. If the sample has been totally closed to argon and potassium since initial cooling, then all of the calculated ages should be the same. As this is rarely the case, ages are calculated based on the reproducibility of the particular samples $^{40}Ar/^{39}Ar$ ratios. Thus, plateau ages are defined. Total gas ages are also useful as indicators of isotopic equilibrium and Ar retention. Total gas ages are really K-Ar ages assuming that all of the Ar is derived from decay of K.

Various fractions of hornblende and muscovite were dated using $^{40}Ar/^{39}Ar$ incremental release techniques in order to calibrate the cooling and exhumation history of the Port aux Basques area following the M_2 metamorphic event. Analytical methods are given in Appendix 4. Sample locations are indicated in figure 13. Ar spectra diagrams are shown in Appendix 6.

Six hornblende concentrates record variable apparent K/Ca ratios in the low temperature portion of the experimental conditions. This variation is also reflected in variable apparent ages, and suggests the experimental evolution of Ar from overgrowths of older grains or from compositionally distinct phases such as biotite. During sample preparation each sample was hand

checked for impurities such as a distinct phase. None of the samples for age dating were seen to contain additional phases when viewed under a binocular microscope. It is considered unlikely that the compositional variations observed are the result of a separate phase in the sample but rather may reflect submicroscopic inclusions in the hornblendes or alternatively overgrowths on a population of older grains. In general, >80% of the total ^{39}Ar evolved from each concentrate is characterized by similar K/Ca ratios at intermediate and high temperatures, indicating that gas release in this temperature range is from a compositionally distinct and homogenous phase. Isotope correlation ages were calculated by using the inverse abscissa ratios of $^{40}Ar/^{39}Ar$ in the age equation. Calculated plateau ages are also listed, but isotope correlation ages are considered more reliable as they do not require an assumption of the present-day $^{40}Ar/^{39}Ar$ ratio. A "plateau" is considered to be defined if the dates recorded by two or more contiguous gas fractions having similar apparent K/Ca ratios, each representing >4% of the total ^{39}Ar evolved (and together constituting >50% of the total quantity of ^{39}Ar evolved) are mutually similar within ±1% interlaboratory uncertainty. See Table 5 for tabulated age date results.

Sample 1 is a penetratively strained, retrogressed garnet-chlorite amphibolite of the GBC (Photograph 8d). It records a hornblende isotope correlation date of 401.4 ± 0.4 Ma and a plateau date of 402.4 ± 0.7 Ma. Sample 2 is a clinopyroxene-bearing amphibolite of the GBC near the GBF and does not define a plateau date (Photograph 8e). It yields a total gas date of 401.0 ± 3.7 Ma

Table 5

All ages in millions of years (Ma)
Chronologic samples are listed in geographic order from west to east.

Sample	Field Number	Phase	Total Gas Date	Ar/Ar Plateau Date	Isotope Correlation Date
1	91-163a	Hbl	402.6+-1.0	402.4+-0.7	401.4+-0.4
2	91-168	Hbl	401.0+-3.7	NA	
3	91-162a	Hbl	402.1+-1.3	402.4+-1.3	398.7+-0.5
3b	91-162b	Ms	394.3+-0.7	394.3+-0.7	
4	91-178a	Hbl	413.2+-2.1	412.7+-1.6	406.7+-1.1
4b	91-178b	Ms	391.4+-0.7	391.3+-0.7	
5a	91-177a	Hbl	407.9+-3.4	407.7+-1.3	405.5+-0.7
5b	91-177b	Ms	390.6+-0.7	391.1+-0.7	
6	91-177e	Hbl	455.9+-1.1	422.2+-1.1	418.9+-2.1

NA-Not applicable under the conditions specified in this paper.

that is consistent with the date obtained from nearby sample 1. Samples 3 and 4 are from the PaBC and yield isotope correlation dates of 398.7 ± 0.5 and 406.7 ± 1.1 Ma and plateau dates of 402.4 ± 1.3 and 412.7 ± 1.6 Ma, respectively. Sample 3 and sample 4 are hornblende amphibolites (Photographs 8b and 9a). Samples 5 and 6 are amphibolites from the HICG and record isotope correlation dates of 405.5 ± 0.7 and 418.9 ± 1.9 Ma and plateau dates of 405.7 ± 1.3 and 422.2 ± 1.1 Ma, respectively (Photograph 9c and 9d).

Muscovite concentrates record well-defined plateau. The two muscovites from the PaBC (Samples 3b and 4b) yield dates of 394.3 ± 0.7 and 391.3 ± 0.7 Ma (Photograph 8f and 9b). Sample 5b, a sillimanite grade gneiss from the HICG, yielded a muscovite concentrate which records a plateau date of 391.1 ± 0.7 Ma (Photograph 9e).

Isotope correlation dates will be used in the following discussion for reasons cited above. The hornblende isotope correlation dates and the muscovite plateau dates are interpreted to reflect the time of cooling through the closure temperatures (Tc) appropriate for intracrystalline diffusion of argon in each mineral phase. The Tc for hornblende is typically taken at 500 ± 25°C (Harrison 1981), but can be variable depending on structural state, composition and cooling rate. The Tc for the K-Ar system in muscovite has been suggested to be 350-400°C (Cliff and Cohen 1980 Purdy and Jäger, 1976). Muscovite Tc of 375 ± 25°C is suggested by empirical comparisons with the K-Ar system, and using the preliminary data of Robins (1972) in the diffusion equations of Dodson (1973).

Cooling History

A temperature-time (T-t) path for rocks of the PaBC and the HICG is shown in figure 15. The U-Pb titanite age of *c.* 417Ma provides a minimum age for the M_2 event. The $^{40}Ar/^{39}Ar$ cooling ages postdate M_2 but have significant implications for the timing of D_3, as hornblende recrystallized during D_3. Sample 1 of the GBC is located near the CRFZ. Sample 2 and 3 lie on the west and east side of the GBF, respectively. These samples are penetratively strained, thus the hornblende ages from these samples (401-402 Ma) are interpreted to date cooling immediately following the development of the LS-tectonite fabrics associated with the D_3 mylonite zones (Photograph 8b). The hornblende ages obtained are *c.* 5 My younger than those samples further removed from the shear zones (Sample 4). Sample 4 (407 Ma) is from a central section of the PaBC and has been little affected by the deformation responsible for the mylonite zones. This age is inferred to closely date the culmination of M_3 metamorphism during the early stages of D_3. Samples 5 and 6 are from the HICG and record different ages. Based only on the different pleochroic schemes and different mineralogy between the samples, the hornblendes may be different compositionally. These compositional differences may account for the age difference recorded by each concentrate. Alternatively the different ages may reflect differential cooling associated with rapid exhumation. The close proximity and similarity in time and space of ages from the titanite and hornblende of the HICG suggests extremely rapid cooling given the difference in appropriate Tc and the similarity between

the titanite and hornblende dates. Considering the titanite date of Dunning et al. (1990a), from the PaBC, the data yield a minimum cooling rate through *c.* 600 and 500°C of 20°C/My. These fast cooling rates indicate rapid exhumation following high grade metamorphism. These rates cannot be explained by the steady state decay of a perturbed geotherm thus, the early exhumation of these gneisses was tectonically controlled, perhaps by tectonic stripping.

The $^{40}Ar/^{39}Ar$ muscovite plateau ages from samples 3b, 4b and 5b (*c.* 391-395 Ma) suggest that metamorphic cooling through 375°C was approximately synchronous across the area. Cooling rates through *c.* 500 and 375°C were calculated for localities 3-5 using the ages recorded by the $^{40}Ar/^{39}Ar$ systems. Locality 3, near the GBF, yields a relatively fast cooling rate of 25-30°C/My. Localities 4 and 5 record slower cooling of around 4-8°C/My. The difference in rates are likely to reflect differential exhumation near the GBF mylonite zone.

These cooling rates indicate that exhumation was initially rapid and was probably tectonically controlled, perhaps driven by early D_3 events. Rare kinematic indicators on syn- to post-D_2 structures such as minor shear zones within the town of Port aux Basques and near the GBF suggests a component of overthrusting with tops to the west-northwest (van Staal et al., 1992a and b). Later, post-D_3, exhumation was slower with overall time integrated rates from 8-1°C/My indicating a return to an erosionally controlled regime. The T-t data above are consitent with the P-T information discussed earlier, and are consistent with a generally overthickened lithosphere with a tectonically controlled initital portion of the

retrograde P-T-t path. Post- D_3 exhumation was slower except near major mylonite zones where unroofing was likely to be more rapid.

Pressure-Temperature-time-Deformation History

The relative timing of porphyroblast growth with respect to deformation is essentially the same for all three structural domains. Microstructural relations indicate early-syn-D_2 growth of kyanite, staurolite and garnet followed by syn-D_2 growth of sillimanite and garnet. The D_1-D_2 kyanite to D_2 sillimanite transition is suggestive of a clockwise trajectory in pressure-temperature space. F_2 folds are recumbent and the present reosional surface reveals a partial Barrovian sequence typical of overthickened terranes, which in this case suggests increasing metamorphic grade to the southeast. The D_1 and D_2 deformations are thought to be progressive and part of the same overall tectonic event (van Staal et al. 1992b) with D_2 and possibly D_1 accompanied by syntectonic amphibolite facies metamorphism with peak M_2 conditions of 700°C at 8-9 kbar around 420Ma. D_1 metamorphism is poorly constrained with the late-D_1 growth of the high pressure aluminum silicate polymorph kyanite, with maximum temperature conditions attained during D_2. Samples near the sillimanite isograd dsiplay evidence for garnet and kyanite growth above the GRAIL reaction curve for a significant portion of their history. As P-T conditions passed through the upper stability limit of the phases St + Ms + Qtz, the Sil + Grt + Bt-bearing assemblages were produced. As temperatures increased, the melting reaction (11) was crossed and culminated in the muscovite-out dehydration reaction 12. This

prograde metamorphism is interpreted to be the result of a crustal thickening event. Pressures reached during D_2 require a minimum of 25-30 km of overburden. The U-Pb titanite age calculated from calc-silicate rocks indicates peak metamorphic conditions occurred at *c.* 420Ma. After the development of a thickened crust, the area may hve become gravitationally unstable and begun to collapse. The similarity between titanite and hornblende ages indicate rapid cooling and exhumation through 500°C. D_3 is thought to be related to transpression, which is manifested by strike-slip and (or) reverse movement along major shear zones (van Staal et al., 1992). Significant retrogression accompanied the D_3 event, resulting in the recrystallization of micas in metapelites and hornblende in amphibolites. The best estimates for "peak" temperatures during D_3 (discussed in Chapter 3) are around 500°C. Hornblende and muscovite $^{40}Ar/^{39}Ar$ dates suggest post- D_3 time-integrated cooling rates of *c.* 8-1°C/My. The relatively lower cooling rates as compared to those obtained from the titanite plus hornblende data indicate that exhumation generally became retarded with time as the crust returned to isostatic equilibrium. With the above in mind, combined with the microstructural and reaction data given earlier, a partial pressure-temperature-time-deformation path (P-T-t-D) is given representing rocks within the sillimanite zone (Fig. 16).

Regional Implications

This study has shown that an upper amphibolite facies metamorphic event characterized by a clockwise P-T-t path with maximum temperatures around 700-750°C at 8-9 kbar occurred in

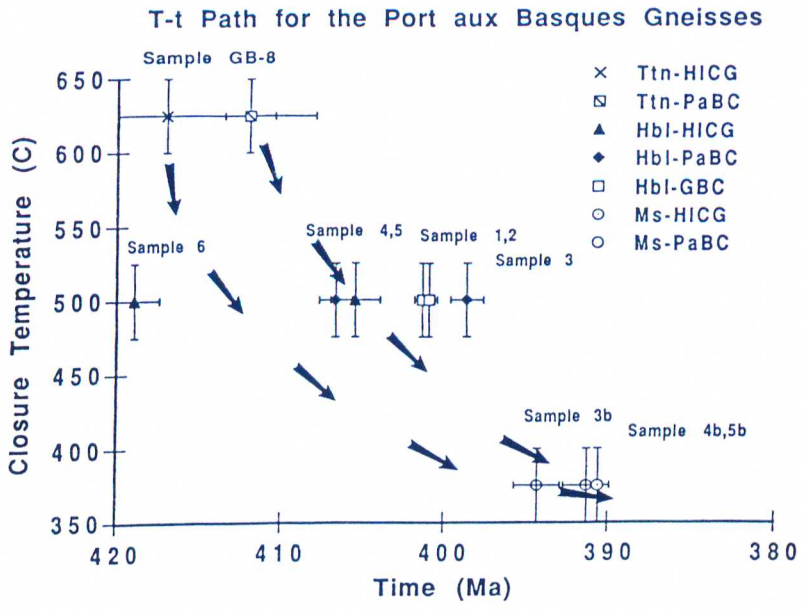

Figure 15. Temperature-time path for the Port aux Basques Gneisses.

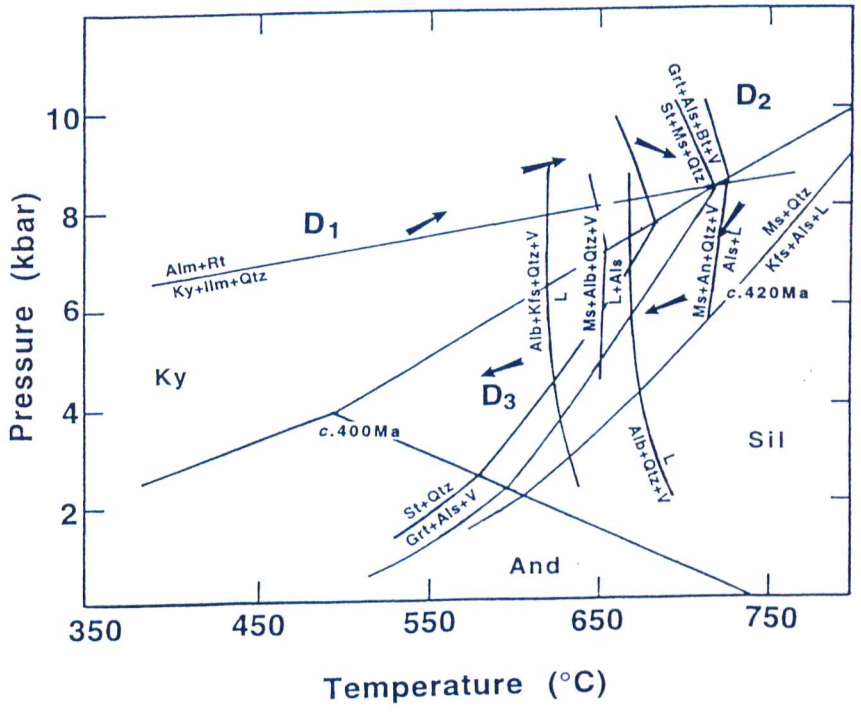

Figure 16. Pressure-Temperature-time-Deformation path for the Port aux Basques Gneisses.

southwest Newfoundland during Silurian times. In particular what other parts of the Northern Appalachians show evidence for a crustal thickening event in the Silurian. Silurian tectonothermal events have been documented in southern Newfoundland along the inboard margin of the Avalon Composite Terrane (Dunning et al. 1990). This event in southwestern Newfoundland was manifested by high-grade metamorphism with a clockwise path in P-T space and a structural regime indicative of overthrusting. Peak metamorphic conditions were reached during D_2 (*c* 420 Ma) or earlier and are coincident with the emplacement of the two mica-granites such as the Rose Blanche Granite.

Regional correlations to other areas and delineation of areas with similar P-T paths can help constrain the type and extent of this Silurian orogenic event. Lin et al. (1993) contend that the HICG is similar in both lithology and structure to the greenschist facies Bay du Nord Group which is part of the Exploits subzone. The Bay du Nord Group has yielded a 466 ± 3 Ma U-Pb zircon date (Dunning et al., 1990a). If the correlation is valid this would provide an upper age limit of deformation for the Port aux Basques Gneisses. Other regionally significant ages which date syn-to post D_1 structures include a 423 +5/-2 Ma U-Pb zircon date for the Little Passage gneiss, lithologically similar to the PaBC. This date represents the peak of metamorphism in these sillimanite grade gneisses which are lithologically similar to the Port aux Basques Gneisses (Dunning et al., 1990a). The syntectonic Gaultois Granite gave a U-Pb zircon date of 421 ± 2 Ma, making it the youngest syntectonic granitic body

in the Hermitage Flexure (Dunning et al., 1990). Additional constraints on the early deformation and metamorphism include the syn-D_1 429 +5/-3 Ma U-Pb zircon date from the granodioritic phase of the Burgeo Intrusive Suite and the post-D_1, La Poile pluton that yielded a U-Pb zircon date of 416 ± 4 Ma (Chorlton and Dallmeyer, 1986).

Isotopic dates reflecting peak-post peak high grade metamorphism include the above Little Passage gneiss and the 412 ± 2 Ma titanite age from amphibolite of the northern PaBC (Dunning et al., 1990a) On Cape Breton Island, a U-Pb monazite age of 411 ± 2 Ma came from the metapelitic gneisses in the central highlands which may be correlatives of the PaBC (Barr and Jamieson, 1991; Lin et al., 1994). These rocks experienced metamorphic conditions of 700-750°C at 8-10 kbar (Plint and Jamieson, 1989). Geochronologic and P-T results presented here confirm a similar Silurian tectonothermal history for southwestern Newfoundland and part of Cape Breton Island.

The GBC and HICG are lithologically similar to the Exploits subzone of the Dunnage Zone, whereas the PaBC resembles the Gander Zone (van Staal et al., 1992). Kinematic analysis of ductile shear zones in southwestern Newfoundland indicate that this event was accompanied by reverse-sinistral overthrusting of the GBC, followed by reverse-dextral thrusting in the CRFZ (van Staal et al., 1992b; Dubé and Lauziere, 1993). This movement becomes dominantly dextral strike-slip to the northeast (Dubé and Lauziere, 1993). Post-D_2 thrusting is also evident on the GBF. The IAMFZ

displays essentially dextral strike-slip movement which is consistent with that of the CRFZ in this part of the area. Structural analysis of the area indicates an initial deformation characterized by overthrusting, possibly in a sinistral transpressive regime, and a later deformation consisting of dominantly dextral movement on the shear zones associated with upright shallow plunging D_3 folds. Thus, the Silurian in Newfoundland was characterized by collisional tectonics whereas the Devonian period was represented by cooling of the metamorphic pile and the intrusion of epizonal potassic granitoids such as the Strawberry Hill and Isle aux Morts Granites.

In southwestern Newfoundland the CRIC marks the eastern edge of the Notre Dame subzone, with the CRFZ defining the northwestern edge of the Exploits subzone. The PaBC may thus represent a Gander inlier, and constitute a structural "window" through the Exploits subzone. As suggested by Williams et al., (1988) one alternative involves tectonic transport of the Exploits subzone across the Gander zone. The PaBC (Gander) was later uplifted (D_3) and juxtaposed against the GBC. Cawood et al. (1994) record Silurian ages of deformation and peak metamorphism for rocks of the Corner Brook Lake region of the Humber Zone. A Silurian age of metamorphism of the Laurentian margin is similar to events in the Port aux Basques Gneisses and throughout Newfoundland. This Siluro-Devonian event can be interpreted as a continent-continent collision, which can be related to the docking of the Avalon Composite Terrane with Laurentia involving the juxtaposition of the Dunnage and Gander Zones.

This Silurian-Early Devonian event has been recorded elsewhere in the Canadian Appalachians. Regional correlations based on style of deformation, geochronology and metamorphism can be made in New Brunswick and Cape Breton Island. Projected along strike this high-grade metamorphism occurs on St. Paul Island (Phinney, 1963) and Cape Breton Island (Plint and Jamieson, 1987) where similar metamorphic conditions of 700-750°C at 8-10 kbar are recorded in equivalent rocks (Lin et al., 1994). Many workers (Barr and Raeside, 1989; Reynolds, 1989; Dunning et al., 1990a,b; and Barr, Jamieson, Raeside and McMullin, 1992) have suggested correlations between the Aspy terrane of Cape Breton Island and southern Newfoundland. In particular, as suggested by Lin et al. (1994), the Jumping Brook Metamorphic suite of Cape Breton Island may be represented by the Harbor le Cou Group in SW Newfoundland while the PaBC is lithologically similar to rocks of the Cape North Group in the northern Cape Breton Highlands. $^{40}Ar/^{39}Ar$ hornblende ages ranging from *c.* 415-380 have been presented by Dallmeyer and Keppie (1993) from medium pressure, greenschist to upper amphibolite facies shear zones in the Cape Breton Eastern Highlands. These ages are similar to those obtained from amphibolite facies shear zones in this study. In New Brunswick, hornblende concentrates from metamorphosed mafic dikes recorded late Silurian to early Devonian (*c.* 416-390 Ma) argon isotope correlation ages (Nance and Dallmeyer, 1993). These ages were interpreted to closely date a late Silurian transpressive deformation related to terrane accretion. This work confirms a similar Silurian through early Devonian geologic history between the Maritimes and

Newfoundland including deformation, metamorphism and plutonism.

Keppie (1989, 1992) related this deformation in Cape Breton to sinistral accretion of the Avalon Composite Terrane with the Gander and Exploits terranes. Other authors (e.g. Nance and Dallmeyer, 1993) suggest that the dextral component of this deformation can be attributed to the accretion of the Meguma Terrane.

The data contained herein supports and confirms a Silurian orogenic event that in southwestern Newfoundland is related to crustal thickening. This event which has been termed the Salinic orogeny, after Dunning et al. (1990a), may be explained in terms of the docking of the Avalon Composite Terrane with a composite Laurentia.

Thesis Summary

Geologic relationships and geochronologic data indicate that the Port aux Basques Gneisses, exposed over much of southwestern Newfoundland, were regionally metamorphosed in a collisional event during the Early Silurian. These gneisses thus represent the exhumed metamorphic core juxtaposed between two terranes as a consequence of the Silurian orogenisis. A first period of deformation (D_1) produced isoclinal folds (F_1) and an axial planar schistosity (S_1). These are overprinted by D_2 tight to isoclinal folds (F_2), and a differentiated crenulation cleavage (S_2). The NE-trending structural character of the area reflects D_3 deformation, which has folded recumbent D_2 structures into a series of large decameter to kilometer scale, upright to steeply inclined often gently doubly plunging open to tight folds (F_3). D_4 is most prevalent near major shear zones where it manifests itself as abundant kink and (or) chevron folds.

Peak assemblages assigned to the M_2 regional metamorphism are syn- to late kinematic with respect to the main S_2 fabric. Late D_1 to early syn-D_2 kyanite porphyroblasts and early to syn- D_2 staurolite porphyroblasts each contain S_1 inclusion trails. Upper amphibolite facies conditions achieved during syn to late- D_2 control the consumption of muscovite, staurolite and kyanite in favor of sillimanite + garnet ± alkali feldspar assemblages in the metapelitic gneisses. The upper amphibolite facies conditions were accompanied by the development of migmatites by anatexis. Information from microstructural relationships, petrogenetic grids and geothermobarometry are combined to characterize the trajectory of the gneisses in pressure-temperature space as clockwise

with maximum thermal conditions of *c.* 700-750°C at 8-9 kbars during D_2, overprinted by retrogression during D_3 and D_4.

In order to better characterize the peak to post peak trajectory six hornblende, three muscovite and one titanite concentrate have been prepared from several units within the Port aux Basques Gneisses to obtain $^{40}Ar/^{39}Ar$ and U-Pb mineral ages. A titanite obtained from a high grade calc-silicate yields a $^{207}Pb/^{206}Pb$ age of *c.* 417 Ma. Hornblende isotope correlation ages range from *c.* 400 to *c.* 420 Ma, while muscovite plateau ages are *c.* 390. The titanite age is interpreted to date cooling shortly after the thermal peak in these gneisses. Initial cooling was rapid, on the order of 25°C/Ma. The hornblendes, however, record the retrogressive effects associated with D_3 and are thought to closely date the onset of this event, while muscovite ages represent further cooling through its appropriate closure temperature. Post-D_3 time integrated cooling rates of approximately 8-1°C/Ma are required for the Port aux Basques Gneisses. Although initial cooling following the M_2 event was rapid, D_3 cooling and exhumation was slower except near major mylonite zones where unroofing was likely to have been accelerated.

Geologic relationships, integrated structural geology and metamorphic petrology, and thermochronologic data indicate that the Port aux Basques Gneisses were the product of a collisional event during the Silurian, which juxtaposed the St. Lawrence promontory on the Laurentian margin and the Cabot promontory on the Avalon margin during the final closure of the Iapetus ocean (Lin et al., 1994b).

Appendix 1

Photographs

Photograph 1. (a) Overprinting relationships between F_1, F_2 and F_3 folds of the Port aux Basques Complex. Note the F_1-F_2 mushroom pattern developed in the more competent metapsammites and the tight F_3 folds developed in the metasemi-pelites (top right). Location: Little Point. (b) Gneissic layering (S_2) developed in the Port aux Basques Gneisses. Location: 3 Km east of Port aux Basques. (c) Typical view of flaggy rocks in the Port aux Basques Complex. The gneissic layering dips to the southeast. Location: Near the RCMP station. (d) F_2-F_3 type 3 fold interference pattern in migmatitic rocks of the Port aux Basques Complex. Location: Northeast of water treatment plant, Port aux Basques. (e) Deformed rocks within the Grand Bay Fault Zone. Note the layer-parallel fault and cut off indicating motion top to the west. Location: Grand Bay Fault Zone. (f) Penetrative D_3 deformation showing non-cylindrical, doubly plunging F_3 folds. Location: Little Point.

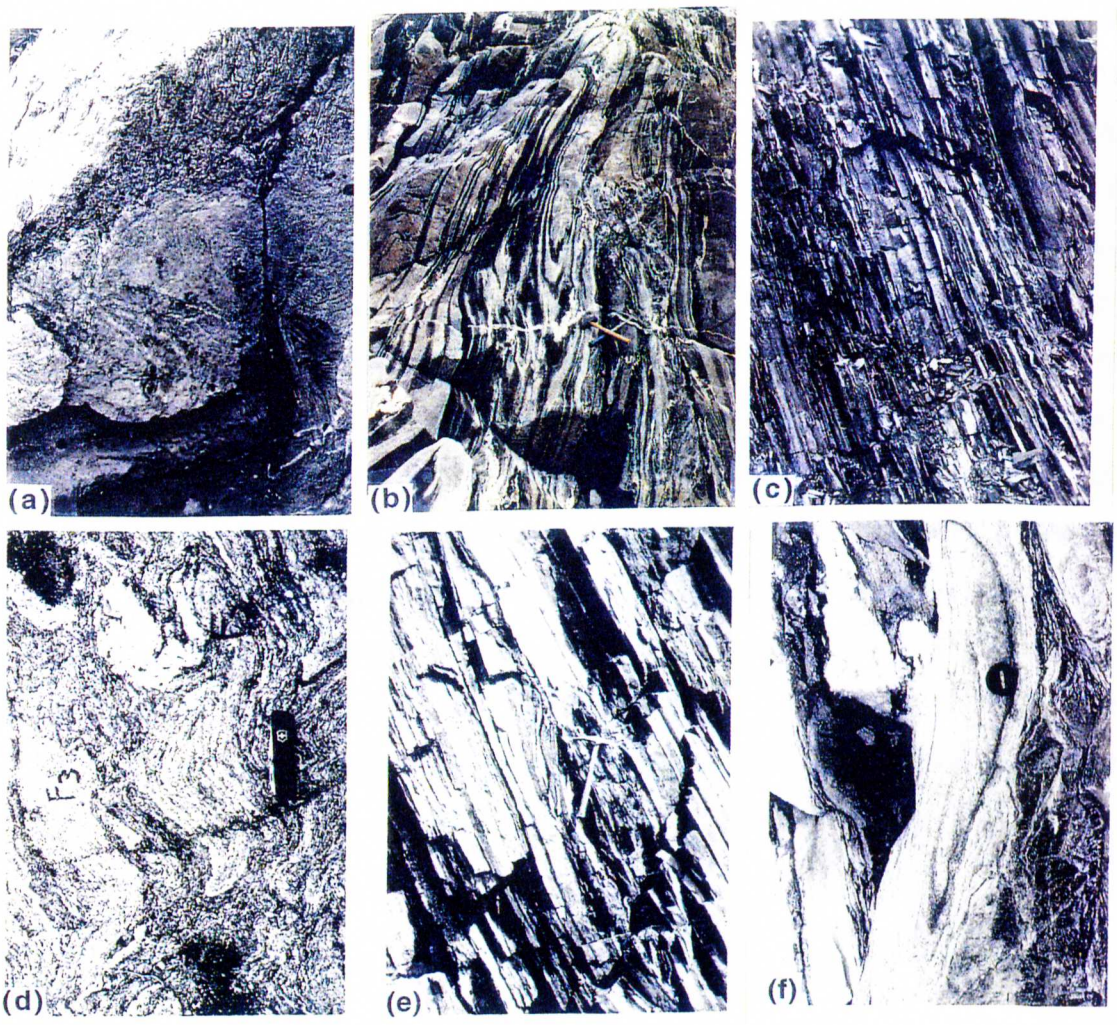
(a)
(b)
(c)
F3
(d)
(e)
(f)

Photograph 2. (a) Leucosome, melanosome development in migmatitic gneisses of the PaBC, A small scale sinistral shear zone obliquely cuts the migmatitic layering (b) Quartz-feldspar leucosomes and biotite-rich melanosomes developed in semi-pelitic Port aux Basques Complex rocks and interpreted to represent upper amphibolite facies partial melting. Location: Port aux Basques. (c) Quartz-feldspar leucosomes associated with melanosome patches, developed in amphibolitic unit of the Port aux Basques Complex. Location: North of RCMP Station, west of Port aux Basques. (d) Diffuse leucocratic area with a preponderance of garnet in semi-pelitic gneiss of the PaBC. Location: Port aux Basques. (e) Quartzo-feldspathic leucosome developed in metapelites of the PaBC. Note large garnet near center of field of view. Location: Port aux Basques. (f) Sillimanite-kyanite-garnet-biotite- schist. The kyanite has rims of sillimanite (fibrolite). Location: Little Point.

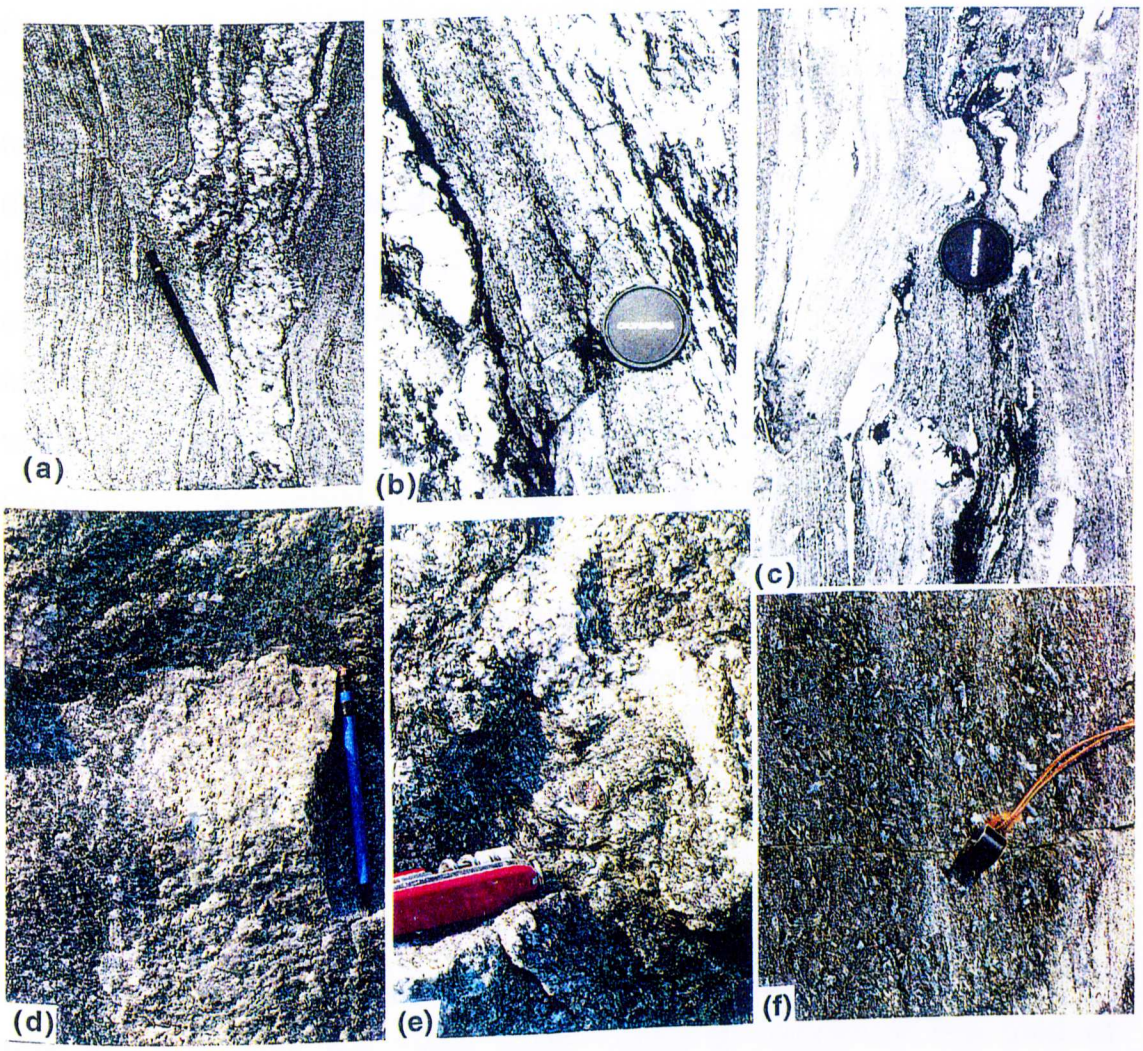
(a)
(b)
(c)
(d)
(e)
(f)

Photograph 3. (a) Kyanite prism (Ky-below and right of lens cap in leucosome) and skeletal garnet (Grt-below kyanite) within quartzo-feldspathic leucosome. Location: Grand Bay. (b) Epidosite nodule developed in amphibolite of the PaBC. Location: Near Channel Head. (c) Amphibolite-granitoid intercalated gneisses with the development of migmatites of the MC. Location: Channel Head. (d) Migmatitic gneisses of the MC, note rotated amphibolitic block within migmatitic gneisses. Location: Fox Roost. (e) Sample 92-71. Garnet-kyanite schist illustrating the preservation of S_1 in the pressure shadow of a garnet which curves into the transposive S_2 fabric. Oriented inclusions in the core of the garnet roughly parallel the S_1 remnant suggesting growth during D_1 or early D_2, which is then overgrown by a relatively inclusion free rim which is wrapped by the S_2 fabric. Long dimension of the field of view is 7.5 mm. Location: Adjacent to Trans-Canada Highway near Port aux Basques. (f) Sample 91-77. Garnet schist showing the hinge area of a F_3 microfold. Both muscovite and biotite have recrystallized as strain-free grains around the hinge zone. Long dimension of the field of view is 8 mm. Location: Port aux Basques. (g) Sample 92-110. Garnet-sillimanite schist illustrating the lack of recrystallization of mica around the hinge zone of a F_4 crenulation. Long dimension of the field of view is 5.5 mm. Location: Southeast of Port aux Basques.

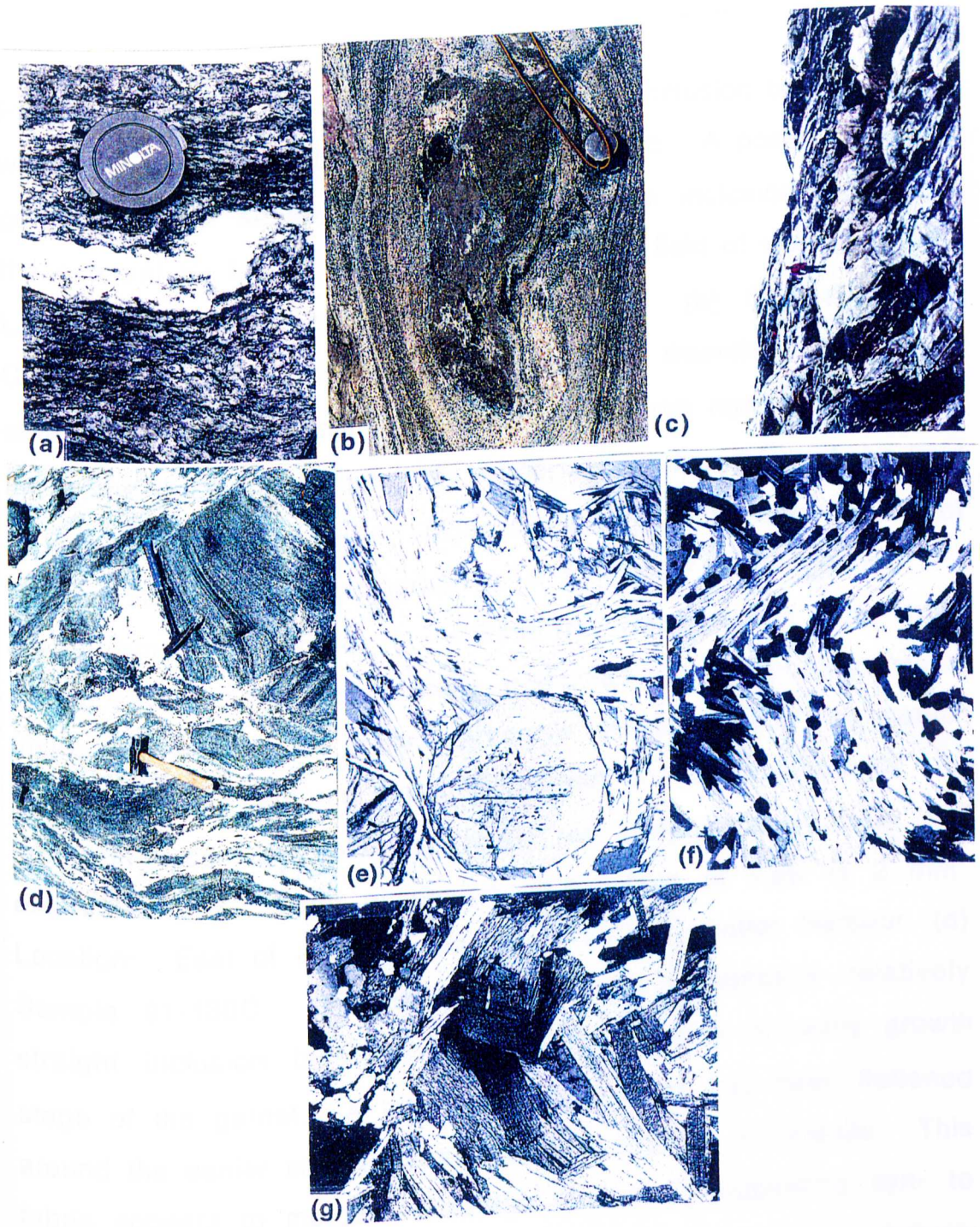
(a)
(b)
(c)
(d)
(e)
(f)
(g)

Photograph 4. (a) Sample 91-68. Sigmoidal inclusion tails in garnet which represent crenulations of a S_0/S_1 fabric. A post-S_1 - pre-S_2 garnet rim now separates the discordant core inclusion trails from the external S_2 fabric. Long dimension of the field of view is 2 mm. Location: Coastline of Port aux Basques. (b) Sample 91-52. Crenulations of S_1 preserved as inclusions of ilmenite in the center of a garnet porphyroblast. A post-D_1 syn-D_2 rim now separates the inclusions from the wrapping S_2 fabric. Long dimension of the field of view is 5 mm. Location: Along coastline near Second Pond. (c) Sample 92-74. Photomicrograph of a sillimanite-garnet gneiss. F_3 crenulations preserved in sillimanite (lower left) are fully transposed around the partially dissolved garnet porphyroblast. Inclusions within the garnet preserve crenulations of an earlier fabric, likely S_1 captured during D_2 growth of the porphyroblast. An inclusion free rim now separates the porphyroblast from the external matrix. Long dimension of the field of view is 2 mm. Location: East of Port aux Basques, north of Butter Harbour. (d) Sample 91-136C. The core of this garnet contains relatively straight inclusion tails (S_0/S_1) preserved during an early growth stage of the garnet. A later developing fabric has been flattened around the earlier core as seen by the inclusions of ilmenite. This fabric appears to merge toward the current S_2 suggesting syn- to late-D_2 growth of this stage of the crystal. An outer relatively inclusion free rim separates the later flattened fabric from the external matrix. The rim of this garnet likely represents syn to late-D_2 growth. Long dimension of the field os view is 9 mm.

Photographs e and g are views of this same garnet under higher magnification. Location: Near Pole Rock. (e) Sample 91-136C. This photograph represents a close up of the crystal detailing the relatively straight core inclusions. Long dimension of the field of view is 4 mm. Location: Near Pole Rock. (f) Sample 91-131a. Kyanite crystal partially enclosed by a garnet porphyroblast. Long dimension of the field of view is 4 mm. Location: Near Pole Rock. (g) Sample 91-136C. Another close up which shows the presence of relict staurolite inclusions in the rims of the garnet. Long dimension of the field of view is 1 mm. Location: Near Pole Rock.

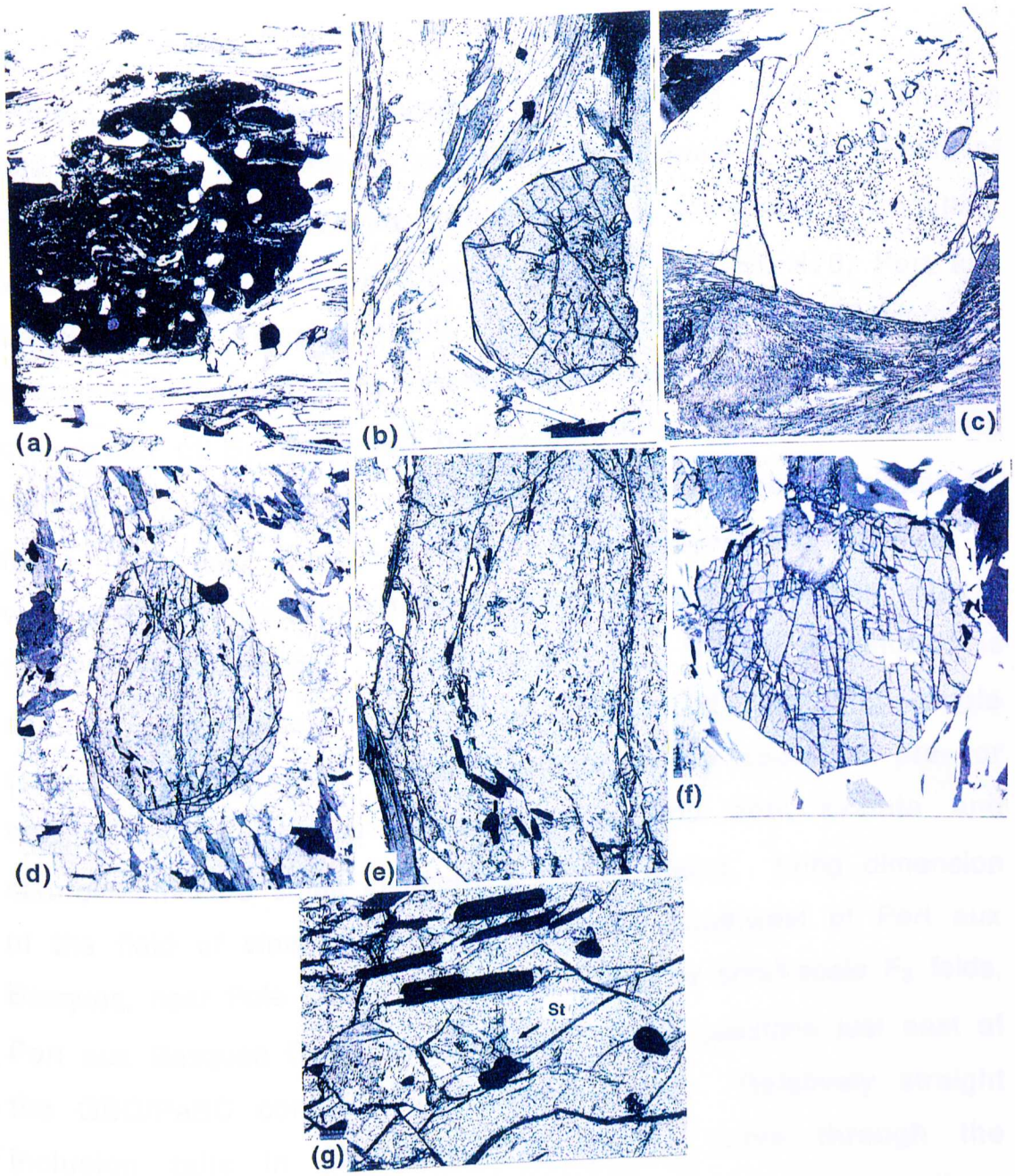
(a)
(b)
(c)
(d)
(e)
(f)
St
(g)

Photograph 5. (a) Staurolite with oriented quartz inclusion interpreted to represent S_1 preserved during early syn-D_2 growth of staurolite now wrapped by transposive S_2 schistosity. Location: West of junction of Trans Canada Highway and Rt. 470, Port aux Basques. (b) Sample 91-56b. Quartz and ilmenite inclusions in staurolite preserving a F_2 microfold are interpreted to represent a crenulation of S_1 preserved during growth of staurolite concurrent with transposition of the S_1 fabric into the current dominant S_2 fabric which now wraps the crystal. Long dimension of the field of view is 8 mm. Location: Near Second Pond along coastline, east of the GBC/PaBC contact. (c) Sample 91-136. The S_2 schistosity is seen to wrap around one end of a large (20 mm long) single staurolite porphyroblast. The staurolite, which could be pre- or early syn-D_2, includes earlier kyanite, and both kyanite and staurolite include small idiomorphic garnet grains. Long dimension of the field of view is 14 mm. Location: Southwest of Port aux Basques, near Pole Rock. (d) Kyanite folded by small-scale F_3 folds, Port aux Basques Complex. Location: Along coastline just east of the GBC/PaBC contact. (e) Sample 91-68. Relatively straight inclusion tails in the center of kyanite curve through the porphyroblast rim and are consistent with early syn-D_2 growth, a conclusion supported by the overall shape of the porhyroblast which exhibits small "tails" at the top left and lower right corners. The dominant schistosity which encloses the kyanite crystal is S_2. Long dimension of the field of view is 4 mm. Location: Coastline of Port aux Basques. (f) Syn to late-D_1 kyanite (possibly early-D_2)

preserved during the formation of the S_2 fabric. Kyanite is folded within the S_2 fabric, thus forming small-scale F_2 folds. Port aux Basques Complex. Location: Near Port aux Basques Elementary School.

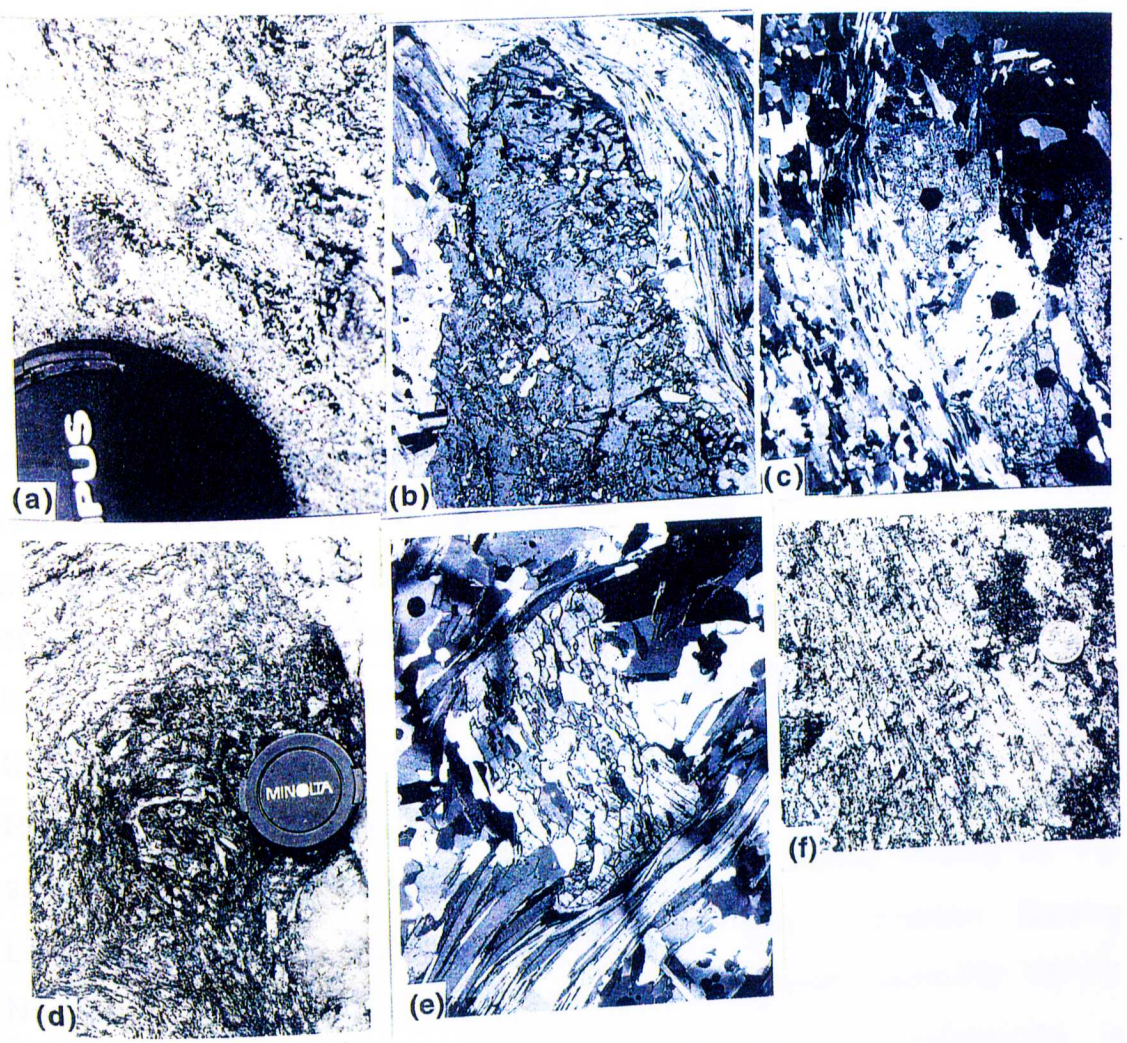
(a)
(b)
(c)
(d)
(e)
(f)
MINOLTA

Photograph 6. (a) Sample 91-54. A kyantite porphyroblast which grew during late D_1 or early during the D_2 folding and S_2 crenulation cleavage formation, which has been wrapped later by S_2 as the developing S_2 foliation transformed into a schistosity. The kyanite appears to have rotated during the development of S_2 and is now curved at each end by post-crystallization deformation. Long dimension of the field of view is 6 mm. Location: Coastline of Port aux Basques. (b) Sample 91-70. Polymorphic kyanite to sillimanite reaction texture in a garnet-aluminium silicate-rutile-biotite gneiss of the Port aux Basques Complex. Long dimension of the field of view is 1.5 mm. Location: Coastline of Port aux Basques. (c) S_0 layering and S_1 schistosity crenulated by S_2, all folded by F_3. Sillimanite lies in the schistosity and is folded by F_3. Location: Harbour le Cou Group, near Northwest Pond. (d) Photomicrograph showing S_2 sillimanite which has recrystallized during folding by F_3. Long dimension of the field of view is 7 mm. Location: Quarry Northwest Arm. (e) S_2 sillimanite and migmatitic layering tightly folded by F_3 such that the long dimension of sillimanite is approximately parallel to the S_3 axial plane cleavage to F_3 folds. Location: North of Butter Harbour. (f) L_3 lineation defined by sillimanite. Location: Near Coast Guard Station, Port aux Basques.

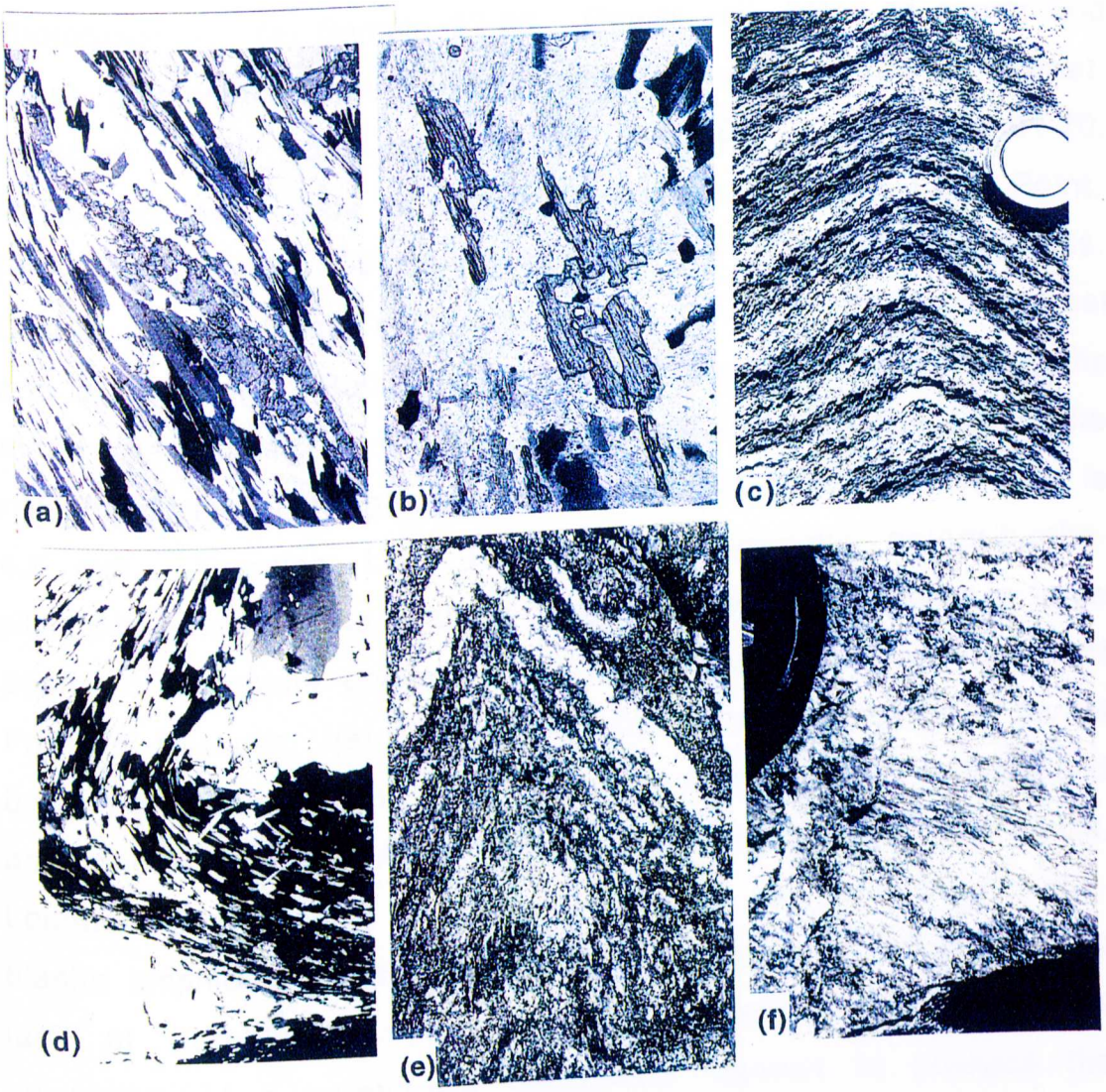
(a)
(b)
(c)
(d)
(e)
(f)

Photograph 7. (a) Sample 92-80. Gneiss with halos of quartz and minor plagioclase around large euhedral porhyroblast of garnet. Location: PaBC, along coastline near the GBF. (b) Sample 91-70. Rutile inclusion inside of a kyanite crystal. Location: Little Point. (c) Sample 92-5D. Photomicrograph of a garnet-kyanite gneiss. Garnet porphyroblasts contain inclusions of rutile within the garnet and at the rims. Rutile at the rims of the garnet and within the matrix are rimmed by ilmenite. Small staurolite crystals lie to the right hand side of the garnet. Long dimension of the field of view is 4.5 mm. Location: Little Point. (d) Migmatitic garnet-biotite-sillimanite gneiss. The quartz + feldspar leucosome contains a large prismatic sillimanite crystal. Location: Approx. 3 km northeast of Port aux Basques. (e) Sillimanite + alkali feldspar + biotite + garnet-bearing gneiss in the MC. The leucosome contains alkali feldspar and an igneous texture. Alkali feldspar also occurs within the matix. Location: Margaree. (f) Sample 91-84. Garnet-clinopyroxene-titanite amphibolitic gneiss of the Port aux Basques Complex. The lack of hornblende near the clinopyroxene porphyroblast is supportive of a hornblende consuming reaction to produce the pyroxene phase. Long dimension of the field of view is 8 mm. Location: Port aux Basques.

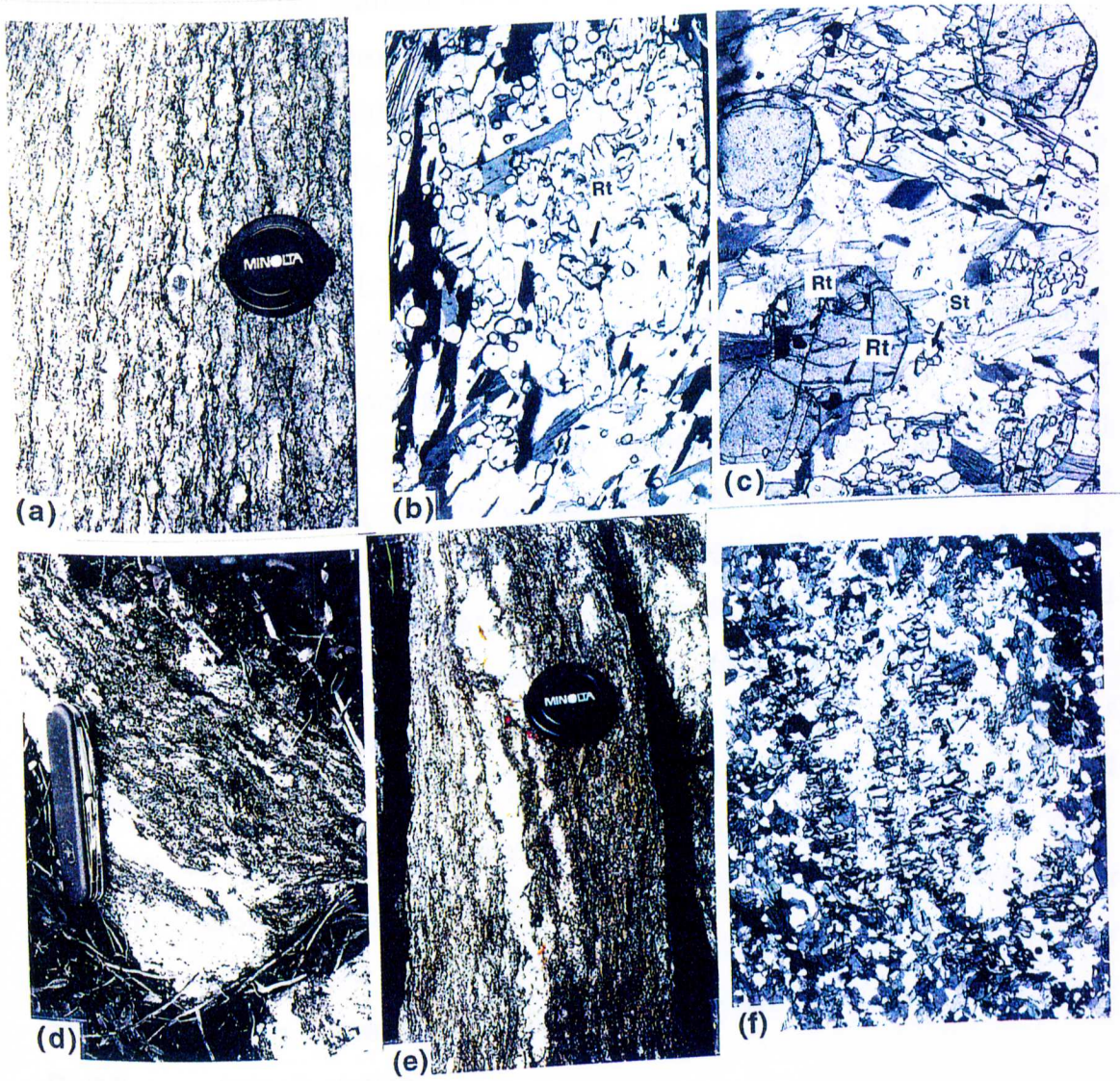
(a)
(b)
Rt
(c)
Rt
St
Rt
(d)
(e)
(f)

Photograph 8. (a) Sample 92-91. Kyanite-hornblende-mica gneiss of the Grand Bay Complex. Long dimension of the field of view is 5 mm. Location: Approximately 3 km north of the RCMP station. (b) $^{40}Ar/^{39}Ar$ chronometric sample number 3. Sample cut parallel to the strong L-tectonite fabric defined by hornblende. The high relief mineral is rutile. Long dimension of the field of view is 7 mm. Location: PaBC near RCMP station. (c) Sample GB-8. A calc-silicate sampled for geochronology. Note the large titanite near the center of the field of view surrounded by clinopyroxene. The crystal at extinction is a garnet porphyroblast. Long dimension of the field of view is 7.5 mm. Location: Head of Gods Bay. (d) $^{40}Ar/^{39}Ar$ chronometric sample number 1. Hornblende fractions were obtained for age dating. Long dimension of the field of view is 2.5 mm. Location: GBC adjacent to Trans-Canada Highway. (e) $^{40}Ar/^{39}Ar$ chronometric sample number 2. Hornblende fractions were obtained for age dating. Long dimension of the field of view is 2.5 mm. Location: GBC, adjacent to Trans-Canada Highway. (f) $^{40}Ar/^{39}Ar$ chronometric sample number 3b. Muscovites were separated for analysis. Long dimension of the field of view is 5 mm. Location: PaBC near RCMP station.

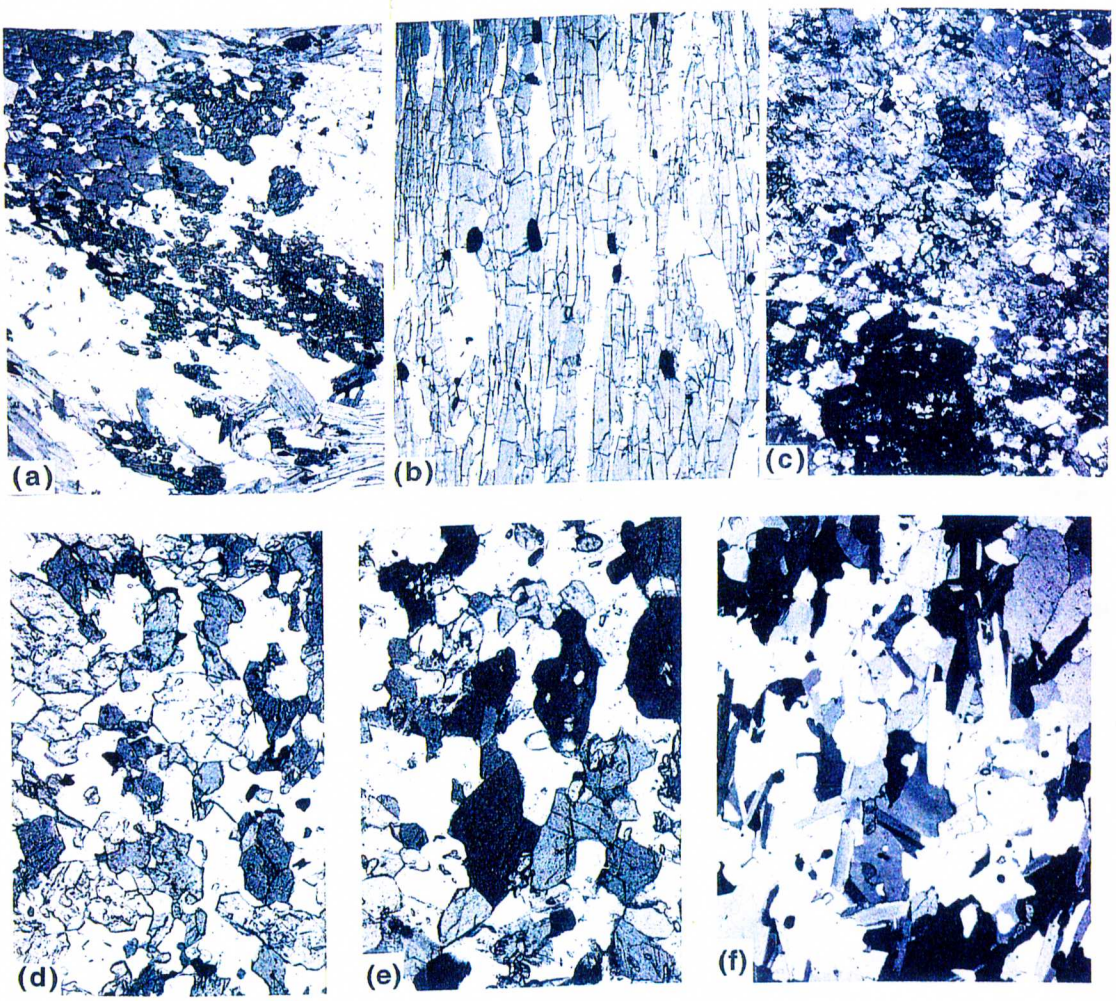
(a)
(b)
(c)
(d)
(e)
(f)

Photograph 9. (a) $^{40}Ar/^{39}Ar$ chronometric sample number 4. Hornblende was separated for analysis. Long dimension of the field of view is 5 mm. Location: Port aux Basques. (b) $^{40}Ar/^{39}Ar$ chronometric sample number 4b. Muscovites were separated for analysis. Long dimension of the field of view is 4.5 mm. Location: Port aux Basques. (c) $^{40}Ar/^{39}Ar$ chronometric sample number 5. Hornblendes were separated for analysis. Long dimension of the field of view is 6.5 mm. Location: Quarry east of Isle aux Morts. (d) $^{40}Ar/^{39}Ar$ chronometric sample number 6. Hornblendes were separated for analysis. Long dimension of the field of view is 3.5 mm. Location: Quarry east of Isle aux Morts. (e) $^{40}Ar/^{39}Ar$ chronometric sample number 5b. Thin section view of a garnet-sillimanite schist. Muscovite fractions were extracted for age dating. Long dimension of the field of view is 4 mm. Location: Quarry east of Isle aux Morts.

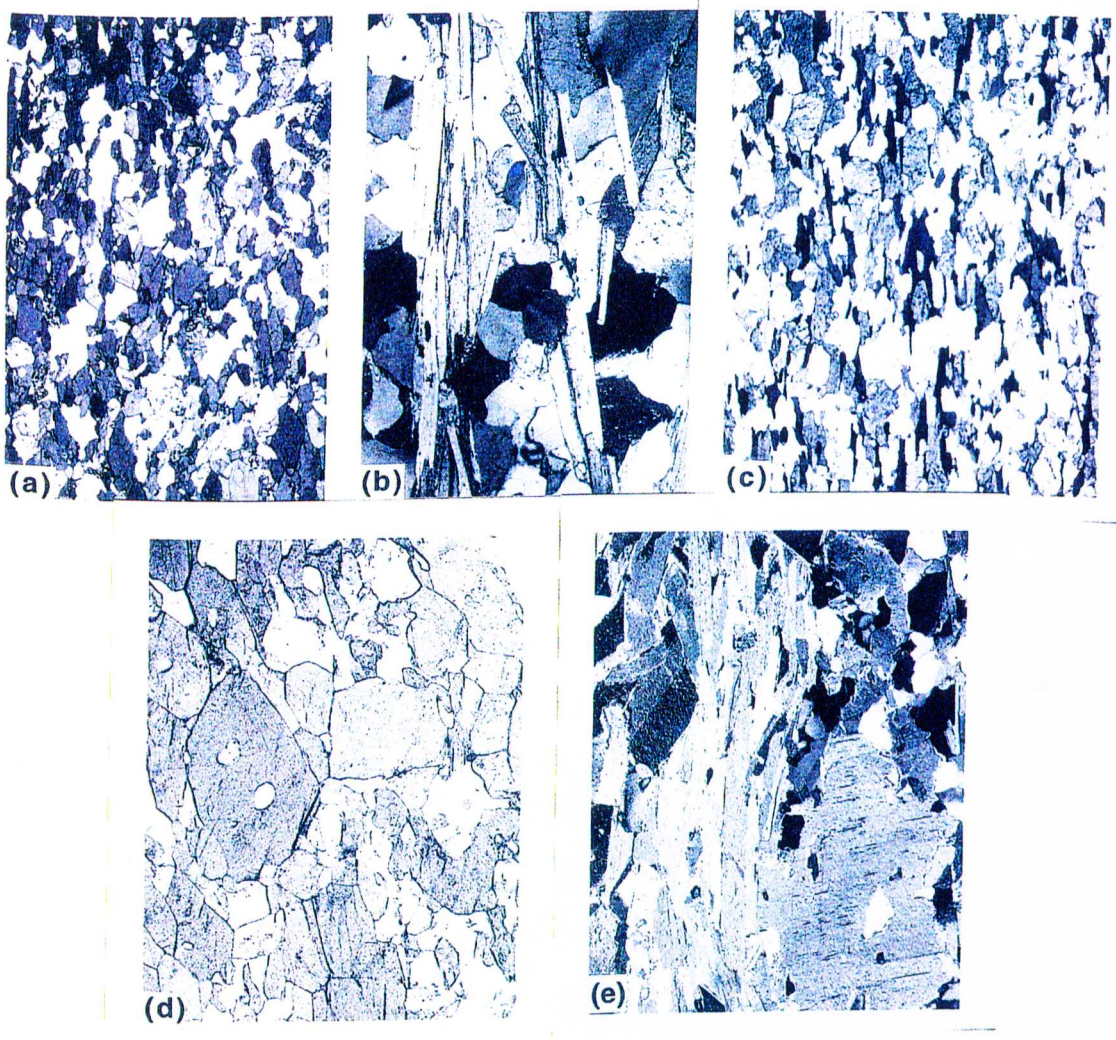
(a)
(b)
(c)
(d)
(e)

Appendix 2 Map of Sample Locations

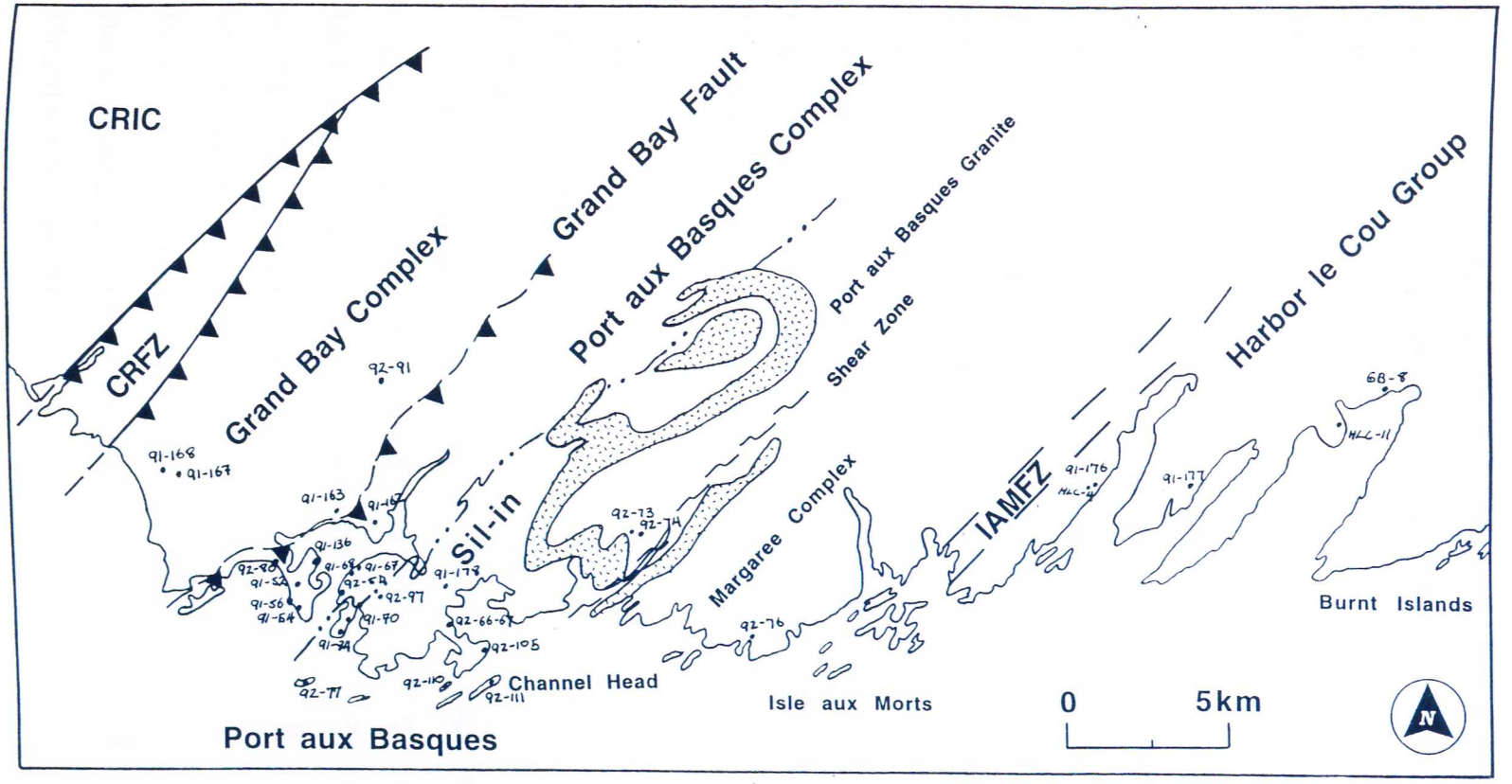

Figure 17. Local geologic map of the Port aux Basques area and the surrounding Port aux Basques Gneisses, showing sample locations for samples discussed in the text. Stippled unit is the Port aux Basques Granite. CRFZ is Cape Ray Fault Zone; IAMFZ is Isle aux Morts Fault Zone;CRIC is Cape Ray Igneous Complex; the dash-dot-dot line is the Sillimanite-in (Sil-in) isograd.

Appendix 3. Sample Descriptions

Abbreviations used: AP=axial plane; HL=hinge line.

Sample 92-91

Location:GBC

Description:

This highly strained leucocratic gneiss contains bladed kyanite and green hornblende lying in the foliation and defining a strong lineation. Kyanite is locally folded by F_3 crenulations. Porphyroblasts of coarse grained garnet and staurolite are rare but do occur. The foliation is defined by recrystallized and flattened quartz, plagioclase, biotite and the aluminum-silicates. Chlorite and white mica help define the matrix of quartz and plagioclase which have irregularly shaped grain boundaries. Structural Measurements: S_2-60 to 160; F_3AP-58 to 175.

Sample 91-163A

Location: GBC

Description:

This medium to course grained amphibolite consists of approximately 65% hornblende (x=yellow-green,Z=dark green). This rock has a very strong L-tectonite fabric associated with shearing along the Grand Bay Fault. The hornblende is unzoned and recrystallized to form a strong stretching lineation. The remaining bulk of the rock consists of plagioclase, quartz, and rutile porphyroblasts. Other accessory minerals include apatite, calcite, chlorite and opaques.

Sample 91-167

Location:GBC

Description:

This two mica schist is a metacalcpelite as seen by the equilibrium assemblage of garnet, epidote, biotite, muscovite, quartz, plagioclase and opaques. This is a fine grained rock with mica between .5 and 1 mm in length. Medium grained crystals of epidote lie in the foliated matrix (S_2) and occur as inclusions in the subhedral garnet porphyroblasts.

Sample 91-168A

Location: GBC

Description:

This well foliated amphibolite consists of approximately 60% hornblende (x=pale yellow-green, Z=blue-green) up to 3.5 mm in longest dimension. The rock has a penetrative LS-tectonite fabric. Hornblende is often resorbed and replaced by chlorite and contains scattered inclusions of plagioclase and quartz. The remaining bulk of the rock consists of medium grained plagioclase, epidote, quartz, chlorite and biotite. Other accessory minerals include rutile, zircon, apatite, titanite and opaques. Small calcite fractures occur sporadically.

Sample 92-5D

Location:PaBC

Description:

S2 is the dominant fabric, defined by biotite, in this kyanite-garnet gneiss. The garnet displays two obvious growth stages. The garnet has inclusion rich cores and inclusion poor rims. Rutile occurs as inclusions in the garnets and in the matrix. The rutile is often rimmed by ilmenite in the matrix. Staurolite may occur as ragged poikilolitic crystals but more often as anhedral grains in the matrix or as relict inclusions in plagioclase. Kyanite contain inclusions of biotite and garnet. The matrix is composed of quartz, rutile, ilmenite and plagioclase. Structural Measurements: S_2-N74E,75SE; L_3-S88W,30 & N64E,65SE; S_3-N68W,50SW; F_2H.L-S80W,60; F_2AP-N74W,54SE.

Sample 91-52

Location:PaBC

Description:

This kyanite-garnet schist has an intensified S_2 foliation defined by muscovite and biotite wrapped around euhedral to subhedral garnets. Bladed kyanite crystals lie in the S_2 fabric and define L_3. The garnet may contain inclusion trails of an earlier fabric. Matrix quartz and plagioclase have straight grain boundaries. Accessories include ilmenite, zircon, apatite and rutile. Structural Measurements: S_2-N60E, 62SE.

Sample 91-54

Location:PaBC

Description:

This garnet-kyanite-staurolite gneiss contains abundant course grained golden poikilolitic staurolite with inclusions of ilmenite and quartz. Muscovite and biotite define the intensified and flattened S_2 fabric which wraps around the porphyroblasts. This sample shows signs of retrogression with biotite alteration to chlorite along cleavage planes and sericite alteration of plagioclase. The matrix contains quartz, plagioclase and opaques. Structural Measurements: S_2-N58E,68SE; L_2(From Amphibolite)-60, N62E; F_2HL-58, N54E.

Sample 92-66

Location:PaBC

Description:

This medium grained garnet-sillimanite schist has a well developed lineation (L_3) defined by sillimanite. Sillimanite has been partly replaced by white mica. Small subhedral garnets are resorbed and replaced by chlorite or white mica aggregates. Structural Measurements: L_3-20 to 95; L_2-80 to 168; S_x-75 to 180.

Sample 91-68

Location: PaBC

Description:

This sample is a garnet-kyanite schist with a well developed

fabric (S_2) in part defined by muscovite and biotite. The foliation wraps around garnet and kyanite porphyroblasts which contain single phase inclusions of quartz and opaques. The bulk of the matrix is composed of quartz and plagioclase with straight grain boundaries. Accessories include apatite, zircon and occasional small grains of staurolite. Structural Measurements: S_2-N50E, 65SE.

Sample 91-70
Location:PaBC
Description:

This garnet schist has a penetrative S_2 fabric defined by biotite. Muscovite is euhedral apparently representing a late phase replacing sillimanite. Garnet is small and euhedral lying in the matrix. Staurolite occurs as anhedral grains inside of plagioclase. Kyanite crystals are strongly replaced by sillimanite and sillimanite plus quartz mosaics. Kyanite lies in the S_2 fabric, sillimanite may be undeformed. Structural Measurements: S_2-N50E,45SE.

Sample 92-71
Location:PaBC
Description:

This garnet schist contains a crenulation fabric of S_1 being transposed into S_2. Large pink porphyroblasts of garnet contain oriented inclusions of opaques. Pressure shadows around the garnets may preserve the S_1 fabric. Rutile occurs in the cores of some garnets. Biotite and muscovite partly define the S_1/S_2 fabric,

while quartz and plagioclase define matrix with straight grain boundaries. Structural Measurements: F_2HL-10 to 225.

Sample 92-74

Location:PaBC

Description:

This sample is a migmatitic sillimanite-garnet bearing gneiss in which the gneissic layering (S_2) has been folded into chevron style F_3 folds accompanied by an axial planar S_3 fabric defined by sillimanite and biotite. Both sillimanite and biotite form a strong S_3 fabric which has intensified and wraps around garnets. Garnet is small and strongly resorbed where biotite and sillimanite have tightened around the porphyroblast. The matrix is composed of quartz, plagioclase and ilmenite. Tourmaline, apatite and zircon are accessories. Structural Measurements: S_3-45 to 145.

Sample 92-76

Location: MC

Description:

This rock is a sillimanite-garnet-alkali feldspar-biotite-bearing gneiss with stromatic migmatitic structures. Alkali feldspar occurs in the leucosome and paleosome of the gneiss. Garnet is partly replaced by biotite.

Sample 91-77

Location:PaBC

Description:

This garnet-mica schist has a strong crenulation cleavage from tight F_3 folding of S_2. The idiomorphic garnet is small and inclusion free throughout the matrix. Muscovite and biotite have recrystallized around the hinge zones of the F_3 folds. Matrix quartz and plagioclase have relatively straight grain boundaries. Accessories include apatite and opaques. Structural Measurements: S_2-N38E, 70SE.

Sample 92-80

Location:PaBC

Description:

This course grained garnet bearing gneiss has a penetrative S_2 fabric defined by biotite. This rock contains mm to cm scale banding of quartzofeldspathic material surrounded by dark biotite rich bands. Large pink garnet porphyroblasts are surrounded by leucocratic quartz rich and ferromagnesium mineral depleted halos. Bladed kyanite crystals are oriented subparallel to the main rock fabric. Minor staurolite crystals define the matrix along with quartz, plagioclase and opaques. Structural Measurements: S_2-65 to 165; L_{ST}-75 to 80.

Sample 91-84

Location:PaBC

Description:

This hornblende gneiss contains porphyroblasts of garnet and clinopyroxene set in an equigranular matrix of hornblende, quartz, titanite and plagioclase. Ilmenite and apatite occur as accessories. Large scale gneissic banding is defined as S_2. Structural Measurements: S_2-N45E,80SE.

Sample 92-87

Location:PaBC

Description:

This biotite bearing amphibolitic gneiss is medium grained with large garnet porphyroblasts with inclusions of ilmenite. The rock has a strong S fabric with small chevron type F_3 folds crenulating the S_2 fabric. The assemblage is Grt + Hbl + Bt + Pl + Qtz + Ilm. Structural Measurements: F_3AP-60 to 160; F_3HL-25 to 234; F_3HL-32 to 252; S_2-55 to 165.

Sample 92-97

Location:PaBC

Description:

S_2 is the gneissic fabric in this garnet-bearing amphibolite which has been folded by F_3. Hornblende has recrystallized around the F_3 folds. Large purple porphyroblasts of garnet are set in a matrix of hornblende, plagioclase and quartz. Accessory minerals

include biotite apatite and ilmenite. Structural Measurements: F_3HL-15 to 240; F_3AP-65 to158; S_2-70 to 275; E.S.-40 to 305.

Sample 92-110

Location:PaBC

Description:

This retrogressed garnet-sillimanite schist shows folding by F_4. Garnets are strongly resorbed and replaced by chlorite or white mica. Biotite and muscovite have been folded but have not recrystallized around the hinge zones of the F_4 folds. Biotite in the matrix is altered to chlorite along cleavage planes and sillimanite has been altered to white mica and quartz aggregates. The matrix is fine grained composed of quartz and plagioclase with irregular grain boundaries. Structural Measurements: F_3HL-20 to 230; F_4AP-82 to 212.

Sample 91-136

Location:PaBC

Description:

This medium grained gneiss has a well developed S_2 fabric defined by muscovite and biotite that wraps around subhedral porphyroblasts of kyanite and poikiloblasts of staurolite. Golden brown staurolites and bladed kyanite are subparallel giving the rock a weak lineation (L_2). Garnet is small and euhedral occurring in the matrix and kyanite/staurolite porphyroblasts. The matrix is

predominately of quartz and plagioclase. Accessory minerals include ilmenite, rutile, apatite, tourmaline and allanite. Structural Measurements: S_2-N30E, 82SE.

Sample 91-136C

Location:PaBC

Description:

This garnet-kyanite-biotite gneiss has a penetrative S_2 fabric defined by brown biotite which flattens around course grained pink garnet. The equigranular matrix is composed of course grained quartz and plagioclase. Staurolite occurs only as a relict inclusion in the rim of the garnet. Plagioclase is often twinned with sericite alteration along the twin planes. Garnet porphyroblasts contain abundant oriented inclusions of ilmenite and quartz. Accessory minerals include apatite, ilmenite and monazite. Structural Measurements: S_2-N30E,82SE.

Sample 91-162A

Location: PaBC

Description:

The rock is a moderately foliated (S_2) amphibolite with well developed straight grain boundaries. Hornblende (x=yellow,Z=blue-green) comprises 60% of the sample and is generally 2-3mm in longest dimension. The primary assemblage is hornblende, plagioclase, quartz, clinopyroxene and minor garnet. Garnet is small and euhedral. Chlorite rich veins crosscut the rock. Other minerals

include biotite, rutile, apatite and opaques.

Sample 91-162B

Location: PaBC

Description:

The rock is a well foliated (S_2), two mica, garnet bearing gneiss. Biotite and muscovite are well developed, comprise approximately 20% of the rock, are 2mm in length and show little retrogressive effects. Garnet is small, around 1mm in diameter. The matrix is dominated by quartz and plagioclase with irregular grain boundaries. Other minerals include zircon, minor chlorite after biotite and opaques.

Sample 91-178A

Location: PaBC

Description:

The rock is well foliated with moderate gneissic segregations. The dominant fabric in this rock is S_2. Mineralogy consists of approximately 70% hornblende with the remainder being quartz, plagioclase and titanite. Hornblende (x=light green, z=dark green) is 1-4mm in longest dimension, unzoned and relatively inclusion free. Minor minerals include epidote, apatite and opaques.

Sample 91-178B

Location: PaBC

Description:

The rock is a two mica (combined 15%), garnet bearing gneiss. Muscovite and biotite define the penetrative foliation (S_2). Muscovite is 1-5mm in longest dimension and the biotite is partially altered to chlorite. Garnet is subhedral and 1-2mm in diameter with inclusion rich cores. Quartz and plagioclase comprise the remaining bulk of the rock. Other minerals include zircon, apatite and opaques.

Sample 91-177A
Location: HICG
Description:

The rock is a biotite-amphibolite that is well foliated and contains gneissic segregation into hornblende-rich and poor layers. The rock is comprised of 30% hornblende (x=light green, z=brown-green) that is 3-7mm in longest dimension. The hornblende is unzoned and inclusion free. The remaining matrix minerals are quartz, plagioclase and biotite Minor minerals include zircon, apatite, titanite and opaques.

Sample 91-177B
Location: HICG
Description:

Muscovite and biotite make up approximately 25% of this well foliated (S_2/S_3) gneiss. Muscovite ranges from 2-6mm in longest dimension and along with biotite, defines the foliation, though some muscovite lies oblique to the foliation. Muscovite is occasionally

associated with fibrolite; quartz inclusions within the muscovite may also contain fibrolite. Quartz, plagioclase and K-feldspar comprise the matrix. Other minerals include garnet, zircon, apatite and opaques.

Sample 91-177E

Location: HICG

Description:

The rock is a medium to course grained, moderately foliated amphibolite. The fabric is a combined S_2/S_3. Hornblende (x=light brown-green, z= brown) appears slightly zoned with lighter colored rims and occasionally contains inclusions of epidote, quartz and zircon. Other minerals include zircon, biotite and opaques.

Sample 92-GB8

Location: HICG

Description:

This sample is a coarse grained calc-silicate gneiss which contains abundant large green clinopyroxene and orange garnet poikiloblasts in a matrix of plagioclase and quartz. The large scale gneissic banding is S_2. Clinopyroxene porphyroblasts show signs of retrogression with hornblende forming along edges and cleavage planes. Garnet porphyroblasts are subhedral with inclusions of quartz, zoisite, and plagioclase that outline inclusion trails indicating overgrowth of the S_2 fabric. Garnet also forms corona texture around clinopyroxene. Titanite is abundant as a well formed

porphyroblast in the matrix. Calcite and apatite are accessories.

Sample HIC-11

Location:HICG

Description:

This medium grained biotite-garnet-sillimanite gneiss contains large porphyroblasts of garnet with inclusions of sillimanite. Prismatic sillimanite defines the foliation with biotite and minor retrograde chlorite wraps around the garnet. The matrix is composed of quartz and plagioclase with irregularly shaped grain boundaries. Staurolite occurs as a relict inclusion in plagioclase and chlorite has replaced some brown biotite along cleavage planes. Accessory minerals include zircon, opaques and allanite. S_2-85,60.

Appendix 4 Analytical Methods

Collection of Samples

Samples of the Port aux Basques Gneisses used in this study were collected by the author during the summer field seasons of 1991 and 1992. Samples were collected on the basis of mineralogy, structure, porphyroblast-matrix relations and location. Only the freshest samples were collected. A number of samples were collected near the kyanite to sillimanite transition for thin sectioning in order to validate field identification of these phases. Samples collected for microstructural analysis were selected from areas where structural relationships were well defined. S-surfaces were marked, noted in the field logbook and placed on the field map. Sample maps were generated in the field on aerial photographs at 1:1200 scale. Sample locations were then transferred to a topographic map. Approximately 200 total samples were collected.

Analytical Methods

Electon probe microanalyzer

Major and minor element analysis of garnet, staurolite, plagioclase, muscovite, biotite, amphibole, rutile and ilmenite were obtained by the electron probe microanalyzer. Polished thin sections were prepared from only the freshest of samples where microstructures were well defined. Microfiche mosaics were composed from each thin section to ensure that the sites of chemical analysis were accurately located and that mineral chemistry was linked to petrographic relationships.

The electron probe microanalyzer contains an electron gun and column that accelerates a focused electron beam to the surface of a

polished sample, which in this case is a thin section. Electrons from this beam penetrate the thin section and collide with atoms in the region known as the excited volume. In this region, secondary x-rays are generated which are characteristic of the excited sample. The intensity of these x-rays are measured by spectrometers. These data are then compared against a variety of standards which enable quantification of the analysis. Specifics for analysis of minerals in this study follow below.

The JEOL 840-A electron probe microanalyzer was equipped with three wavelength-dispersive spectrometers and using an accelerating voltage of 15 kV. Garnets were analyzed using a beam current of 15-20 nA and a spot size of 2 x 2 um. Staurolites were analyzed using a beam current of 15 nA and a spot size of 5 x 5 um. Plagioclase, pyroxene, amphibole and biotite were analyzed with a beam current of 10 nA and a spot size generally of 10 x 10 um. Spot sizes were increased in phases which have lighter elements (such as Na) which are likely to rapidly diffuse. Elements were analyzed for 30 seconds per point. Analytical uncertainty due to count statistics is ± 0.6% for Si. Uncertainties in other elements vary from 1 to 2% for major cations up to 25% for minor elements such as Ti in garnet. Errors listed are one sigma. Vacuum operation was around 10^{-6} Torr.

Standards used were naturally occurring silicates and oxides obtained from the Natural Museum of Natural History, Washington D.C. Mineral standards used were the Roberts Garnet, Kakanui Hornblende, Durango Apatite, Sanidine, Albite, Plagioclase, Willemite and Rhodonite. Data reduction was performed using the techniques of Bence & Albee (1968).

Mass Spectrometry

Isotopes of U and Pb were analyzed by thermal ionization mass spectrometry. After chemical separation which involve ion exchange separations to purify the sample by removing alkalies and other elements which contribute to additional interferences during the analysis, the elements are loaded as a solution on a rhenium filament. The sample filament is then placed in the sample turret and slowly heated for analysis. A suitable current is found that creates a stable ion beam which enters a magnetic field whose magnetic field lines are perpendicular to the ion travel direction and thus allow separation of ions based on mass. The separated ion beams continue through the analyzer tube and into the collector. One of the ion beams are focused through a collector slit allowing entry into the detector cup. This beam is neutralized by electrons that flow from ground to the collector through a resistor. The voltage difference generated across the resistor is measured. The resulting signal is traced on a chart with each peak representing a discrete mass to charge ratio that identifies that isotope in the mass spectrum of the element analyzed. The strength of the signal or height of the peak determines the relative abundance of the isotopes.

The determination of $^{40}Ar/^{39}Ar$ dates was accomplished using a gas source mass spectrometer. The essentials of how the instrument works are the same as above, except that the sample is prepared and heated for analysis differently. A clean mineral separate is first irradiated in a nuclear reactor. During this time a small portion of the ^{39}K is converted to ^{39}Ar. During incremental heating of the sample, the released sample gas is introduced into an

electron impact source where the gas is ionized by collision with a stream of electrons. The ion beam is then collected and resolved as above. Thus a series of calculated dates are obtained as the argon is released from different crystallographic sites as heating continues.

Samples for geochronolgy were selected from only the freshest outcrops. Weathered portions were chipped off in the field. Samples were only collected from areas where structures and petrology were well defined.

Whole rock samples originally 1 X 1 X 1 .5' were quartered and crushed to <1 mm for mineral separations. Titanite and calcite was separated from calc-silicate; hornblende was separated from amphibolites; and muscovite was from metapelitic gneisses. Mineral separates were purified using heavy liquids and a Frantz Isodynamic separator. Individual inclusion free grains and fragments were hand picked under a binocular microscope. Only the largest ≥ .5 mm crystals of titanite were selected based on the lack of visible inclusions, color and homogeneity.

Sample preparation for hornblende and muscovite began as above and then involved crushing and sieving the sample into different size fractions. The size fractions were than washed in water and acetone. Hornblende and muscovites were separated from the rock matrix by a combination of heavy liquids and gravity settling. At this point the various size fractions were reviewed for sample purity. The largest size fraction which has the fewest contaminants was selected for further processing. The samples were then put through a large magnetic separator. After this coarse separation, the samples were run through a Franz magnetometer,

again viewed under a binocular microscope and any mineral impurities were removed by handpicking. Thus only pure separates were collected. Any potential impurities were not detectable by binocular microscope. Thin sections do reveal inclusions of quartz, plagioclase, opaques and minor epidote. The clean mineral separates were wrapped in aluminum-foil packets, encapsulated in sealed quartz vials.

For $^{40}Ar/^{39}Ar$ determinations, washed, clean, mineral concentrates were wrapped in aluminum foil packets, encapsulated in sealed quartz vials, and irradiated for 40 hrs in the TRIGA Reactor at the U.S. Geological Survey, Denver, CO. Variations in the flux of neutrons along the length of the irradiation assembly were monitored with several mineral standards. The samples were incrementally heated until fusion in a double-vacuum, resistance heated furnace following methods described by Dallmeyer and Gil-Ibarguchi (1990). Measured isotopic ratios were corrected for total system blanks and the effects of mass fractionation. Interfering isotopes produced during irradiation were corrected using factor reported by Dalrymple et al. (1981) for the TRIGA Reactor. Interlaboratory uncertainties are *c* ±1.25-1.5% of the quoted age.

Separated titanite was washed in cool H_2O four times and then washed in 1N HCl for about 10 minutes to remove surface contamination. Titanite was dissolved in a screw top Savillex™ teflon vial at *c* 100°C using a mixture of concentrated HF and HNO_3. The mineral decomposed to a white powder in less than 20 hours. After evaporating the sample for 24 hours, it was completely

soluble in 6N HCL. The sample stayed in solution when diluted to 2N HCL for ion exchange chemistry. Calcite was washed in cool H_2O for 20 minutes to remove surface contamination. It was dissolved in a screw top Savillex™ teflon vial at room temperature using 2N HCL. The sample dissolved completely in < 2 minutes. After evaporating for 24 hours the sample dissolved completely in HBr for ion exchange chemistry. Pb was separated using HBr-HCl chemistry and U by HNO_3-H_2O chemistry using BioRad AG50-X8 anion exchange resin (Tilton, 1973 and Mattinson, 1986)

For isotopic measurements, Pb and U were loaded on single rhenium filaments using the phosphoric acid-silica gel technique (Cameron et al., 1967) The total procedural blank for Pb during this time was between 100-200 pg.

Measured Pb ratios for the blank are:

$^{206}Pb/^{204}Pb = 17.42 \pm 0.5$

$^{207}Pb/^{204}Pb = 15.85 \pm 0.1$

$^{208}Pb/^{204}Pb = 35.03 \pm 0.5$

Measured Pb isotopic ratios were corrected for fractionation using a value of 0.12% per atomic mass unit (a.m.u.). Uranium fractionation was corrected using a value of 0.13% per amu.

The uncertainties for the U/Pb and Pb/Pb ratios are 2 sigma.

Appendix 5 Representative Mineral Analysis

All mineral formulas were calculated assuming all FeO as Ferric Iron with the exception of Cpx & Ilm.

Fe2O3 for Cpx and Ilm was based on stochiometry and site occupancy.

Analysis are in weight percent.

Garnet

Sample	HLC-11B	HLC-11B	92-5D	92-5D
Sample Pt.	GRT-A-3	GRT-A-8	GRT-C-1	GRT-C-4
	CORE	RIM	RIM	40UM-RIM
SiO2	38.07	37.25	37.07	36.89
Al2O3	22.02	22.27	21.98	21.82
TiO2	0.00	0.06	0.14	0.00
FeO	32.27	35.19	33.85	33.31
MnO	0.98	1.14	1.35	1.26
MgO	5.63	3.85	4.28	4.92
CaO	1.36	1.44	1.58	1.61
Total	100.33	101.20	100.25	99.81
Si	2.99	2.95	2.95	2.95
Al	2.04	2.08	2.06	2.05
Ti	0.00	0.00	0.01	0.00
Fe	2.12	2.33	2.25	2.22
Mn	0.07	0.08	0.09	0.09
Mg	0.66	0.45	0.51	0.59
Ca	0.11	0.12	0.14	0.14
XMg	23.71	16.31	18.40	20.83
Sum Cations	7.99	8.01	8.01	8.03
No. Oxygens	12.00	12.00	12.00	12.00

Sample	92-5D	91-70	91-70	91-136
Sample Pt.	GRT-C-13	GRT-B-1	GRT-B-3	GRT-D-2
	CORE	RIM	CORE	RIM
SiO2	36.81	37.40	36.77	39.56
Al2O3	21.45	22.10	21.64	21.82
TiO2	0.06	0.16	0.05	0.00
FeO	32.57	32.72	32.43	31.10
MnO	1.77	4.45	4.40	1.25
MgO	5.00	3.97	4.36	3.97
CaO	1.86	0.64	0.64	2.72
Total	99.52	101.44	100.29	100.42
Si	2.95	2.96	2.94	3.09
Al	2.03	2.06	2.04	2.01
Ti	0.00	0.01	0.00	0.00
Fe	2.18	2.16	2.17	2.03
Mn	0.12	0.30	0.30	0.08
Mg	0.60	0.47	0.52	0.56
Ca	0.16	0.05	0.06	0.23
XMg	21.48	17.80	19.32	18.52
Sum Cations	8.04	8.01	8.03	7.90
No. Oxygens	12.00	12.00	12.00	12.00

Sample	91-136	91-84	91-84	91-84
Sample Pt.	GRT-D-8	GRT-A-4	GRT-A-1	GRT-B-5
	CORE	RIM	CORE	RIM
SiO2	39.36	38.73	38.84	38.80
Al2O3	21.69	21.57	21.59	21.67
TiO2	0.00	0.00	0.14	0.04
FeO	30.51	19.30	18.89	19.58
MnO	1.83	7.15	5.96	7.04
MgO	4.36	1.50	1.43	1.51
CaO	2.59	12.00	13.85	12.27
Total	100.34	100.25	100.70	100.91
Si	3.08	3.04	3.03	3.03
Al	2.00	2.00	1.98	1.99
Ti	0.00	0.00	0.01	0.00
Fe	2.00	1.27	1.23	1.28
Mn	0.12	0.48	0.39	0.47
Mg	0.51	0.18	0.17	0.18
Ca	0.22	1.01	1.16	1.03
XMg	20.29	12.14	11.87	12.11
Sum Cations	7.92	7.96	7.97	7.97
No. Oxygens	12.00	12.00	12.00	12.00

Sample	91-84	GB-8	GB-8	91-167A
Sample Pt.	GRT-B-2	GRT-A-2	GRT-A-4	GRT-A-1
	CORE	RIM	CORE	RIM
SiO2	38.50	37.82	37.76	37.65
Al2O3	21.41	21.00	21.15	21.49
TiO2	0.05	0.19	0.18	0.09
FeO	19.33	21.50	20.00	28.21
MnO	5.89	2.86	2.83	3.12
MgO	1.37	0.67	0.49	2.38
CaO	13.58	16.81	18.29	5.11
Total	100.13	100.85	100.70	98.05
Si	3.03	2.98	2.97	3.04
Al	1.98	1.95	1.96	2.04
Ti	0.00	0.01	0.01	0.01
Fe	1.27	1.42	1.32	1.90
Mn	0.39	0.19	0.19	0.21
Mg	0.16	0.08	0.06	0.29
Ca	1.14	1.42	1.54	0.44
XMg	11.24	5.29	4.16	13.06
Sum Cations	7.98	8.04	8.04	7.93
No. Oxygens	12.00	12.00	12.00	12.00

Sample	91-176	91-176	92-97	92-97
Sample Pt.	GRT-A-1 CORE	GRT-A-2 RIM	GRT-A-1 CORE	GRT-A-4 RIM
SiO2	37.65	37.51	38.84	37.69
Al2O3	21.04	21.07	22.51	22.51
TiO2	0.50	0.04	0.00	0.00
FeO	25.21	25.17	27.22	27.77
MnO	2.96	2.93	2.00	1.85
MgO	0.56	0.53	4.76	4.52
CaO	11.59	10.77	4.81	5.54
Total	99.51	98.02	100.14	99.76
Si	3.01	3.04	3.02	2.97
Al	1.98	2.01	2.07	2.09
Ti	0.03	0.00	0.00	0.00
Fe	1.69	1.70	1.77	1.83
Mn	0.20	0.20	0.13	0.12
Mg	0.07	0.06	0.55	0.53
Ca	0.99	0.93	0.40	0.46
XMg	3.82	3.62	23.75	22.49
Sum Cations	7.97	7.96	7.95	7.99
No. Oxygens	12.00	12.00	12.00	12.00

Sample	92-87	92-87	92-87	91-80
Sample Pt.	GRT-A-3 RIM	GRT-A-9 SPS-INFLEC.	GRT-A-40 CORE	GRT-A-1 RIM
SiO2	36.70	37.65	37.56	37.53
Al2O3	21.06	22.23	21.82	21.63
TiO2	0.26	0.23	0.14	0.19
FeO	29.86	29.45	28.06	33.41
MnO	3.54	2.70	4.00	1.57
MgO	3.41	4.25	4.39	3.43
CaO	4.99	5.09	5.13	1.86
Total	99.82	101.60	101.10	99.62
Si	2.95	2.94	2.95	3.00
Al	1.99	2.05	2.02	2.04
Ti	0.02	0.01	0.01	0.01
Fe	2.01	1.92	1.84	2.24
Mn	0.24	0.18	0.27	0.11
Mg	0.41	0.50	0.51	0.41
Ca	0.43	0.43	0.43	0.16
XMg	16.91	20.47	21.81	15.46
Sum Cations	8.04	8.02	8.03	7.97
No. Oxygens	12.00	12.00	12.00	12.00

Biotite

Sample	91-136	91-136	91-136	HLC92-11B
Sample Pt.	BT-A-3	BT-A-2	BT-C-1	BT-A-6
SiO2	36.08	36.34	36.45	36.99
TiO2	2.28	2.40	1.90	2.09
Al2O3	18.98	18.68	19.25	21.01
FeO	19.19	19.02	18.41	15.93
MnO	0.04	0.07	0.05	0.00
MgO	11.39	11.21	11.36	12.45
CaO	0.03	0.00	0.00	0.52
Na2O	0.32	0.43	0.29	0.44
K2O	8.81	8.70	9.02	8.39
Total	97.12	96.85	97.73	97.81
Si	5.36	5.40	5.41	5.34
Ti	0.25	0.27	0.21	0.23
Al	3.32	3.27	3.37	3.57
Fe	2.38	2.37	2.29	1.92
Mn	0.01	0.01	0.01	0.00
Mg	2.52	2.49	2.51	2.68
Ca	0.01	0.00	0.00	0.08
Na	0.09	0.12	0.08	0.12
K	1.67	1.65	1.71	1.54
XMg	51.41	51.24	52.38	58.21
Sum Cations	15.61	15.58	15.59	15.48
No. Oxygens	22.00	22.00	22.00	22.00

Biotite

Sample	92-5D	91-70	91-70	91-167A
Sample Pt.	BT-A1	BT-A-2	BT-C-1	BT-A-1
SiO2	36.65	35.84	36.44	36.16
TiO2	2.80	2.39	2.62	1.93
Al2O3	20.26	18.71	19.04	17.57
FeO	17.67	17.95	17.13	20.22
MnO	0.03	0.11	0.14	0.24
MgO	11.45	11.48	11.34	10.29
CaO	0.00	0.00	0.00	0.00
Na2O	0.30	0.25	0.40	0.07
K2O	7.99	9.82	9.38	9.45
Total	97.15	96.55	96.49	95.93
Si	5.36	5.36	5.41	5.49
Ti	0.31	0.27	0.29	0.22
Al	3.49	3.30	3.33	3.15
Fe	2.16	2.25	2.13	2.57
Mn	0.00	0.01	0.02	0.03
Mg	2.49	2.56	2.51	2.33
Ca	0.00	0.00	0.00	0.00
Na	0.09	0.07	0.12	0.02
K	1.49	1.87	1.78	1.83
XMg	53.59	53.27	54.13	47.57
Sum Cations	15.54	15.69	15.58	15.64
No. Oxygens	22.00	22.00	22.00	22.00

Biotite

Sample	91-167A	91-80
Sample Pt.	BT-C-1	BT-C-1
SiO2	35.28	35.07
TiO2	1.68	2.66
Al2O3	17.85	18.73
FeO	19.85	19.57
MnO	0.26	0.07
MgO	10.61	9.67
CaO	0.00	0.00
Na2O	0.05	0.32
K2O	9.10	8.91
Total	94.68	95.00
Si	5.42	5.36
Ti	0.19	0.31
Al	3.23	3.37
Fe	2.55	2.50
Mn	0.03	0.01
Mg	2.43	2.20
Ca	0.00	0.00
Na	0.02	0.09
K	1.78	1.74
XMg	48.80	46.83
Sum Cations	15.67	15.57
No. Oxygens	22.00	22.00

Hornblende

Sample	PAB91-176	PAB91-176	PAB91-84	PAB91-84
Sample Pt.	HBL-A-1	HBL-B-1	HBL-A-1	HBL-B-2
SiO2	38.29	38.74	43.01	42.44
TiO2	1.02	0.76	0.80	0.78
Al2O3	14.07	13.97	10.72	11.39
FeO	26.18	26.22	19.66	20.67
MnO	0.33	0.24	0.62	0.56
MgO	2.78	2.97	8.54	8.54
CaO	11.27	11.41	11.11	11.33
Na2O	1.27	1.14	1.89	1.33
K2O	1.81	1.77	0.32	0.33
Total	97.02	97.22	96.67	97.37
Si	6.07	6.11	6.50	6.35
Ti	0.12	0.10	0.09	0.09
Al	2.63	2.60	1.91	2.00
Fe2	3.09	2.99	1.79	1.57
Fe3	0.38	0.47	0.70	1.02
Mn	0.05	0.03	0.08	0.07
Mg	0.66	0.70	1.93	1.91
Ca	1.92	1.92	1.80	1.82
K	0.36	0.36	0.06	0.06
Na	0.39	0.35	0.55	0.39
Sum Cations	15.67	15.62	15.41	15.27
No. Oxygens	23.00	23.00	23.00	23.00

Hornblende

Sample	PAB92-97	PAB92-97	PAB92-87	PAB92-87
Sample Pt.	HBL-A-2	HBL-A-4	HBL-A-2	HBL-A-5
SiO2	41.78	41.85	41.43	41.71
TiO2	0.63	0.59	0.53	0.55
Al2O3	16.15	16.22	16.17	16.87
FeO	16.48	16.82	17.39	17.21
MnO	0.06	0.03	0.25	0.24
MgO	9.68	9.60	8.36	7.94
CaO	11.42	11.52	11.23	11.13
Na2O	1.20	1.19	1.19	1.32
K2O	0.54	0.52	0.08	0.00
Total	97.94	98.34	96.63	96.97
Si	6.07	6.07	6.11	6.13
Ti	0.07	0.06	0.06	0.06
Al	2.77	2.76	2.81	2.92
Fe2	1.04	1.06	1.18	1.28
Fe3	0.96	0.98	0.97	0.84
Mn	0.01	0.00	0.04	0.03
Mg	2.09	2.07	1.83	1.74
Ca	1.78	1.78	1.77	1.75
K	0.10	0.10	0.02	0.00
Na	0.34	0.33	0.34	0.38
Sum Cations	15.22	15.21	15.12	15.12
No. Oxygens	23.00	23.00	23.00	23.00

Clinopyroxene

Sample	91-84	91-84	91-84	GB92-8
Sample Pt.	CPX-A-5 RIM	CPX-A-6 RIM	CPX-A-2 CORE	CPX-A-1 CORE
SiO2	51.13	51.53	50.65	51.55
TiO2	0.14	0.13	0.15	0.00
Al2O3	1.77	1.73	1.76	0.50
FeO	12.55	11.54	13.04	13.59
Fe2O3	1.81	2.26	2.55	1.77
MnO	0.88	0.89	0.91	0.26
MgO	10.04	10.15	8.95	9.27
CaO	21.15	21.17	21.07	23.35
Na2O	0.61	0.88	0.56	0.29
Total	100.08	100.28	99.64	100.58
Si	1.95	1.96	1.95	1.98
Ti	0.00	0.00	0.00	0.00
Al	0.08	0.08	0.08	0.02
Fe2	0.40	0.37	0.42	0.44
Fe3	0.05	0.07	0.07	0.05
Mn	0.03	0.03	0.03	0.01
Mg	0.57	0.58	0.51	0.53
Ca	0.87	0.86	0.87	0.96
Na	0.05	0.07	0.04	0.02
XMg	58.79	61.04	55.03	54.88
Sum Cations	4.00	4.00	3.99	4.00
No. Oxygens	6.00	6.00	6.00	6.00

Clinopyroxene

Sample	GB92-8
Sample Pt.	CPX-A-4 RIM
SiO2	50.84
TiO2	0.08
Al2O3	0.57
FeO	13.11
Fe2O3	2.76
MnO	0.26
MgO	9.25
CaO	23.29
Na2O	0.25
Total	100.41
Si	1.95
Ti	0.00
Al	0.03
Fe2	0.42
Fe3	0.08
Mn	0.01
Mg	0.53
Ca	0.96
Na	0.02
XMg	55.63
Sum Cations	4.00
No. Oxygens	6.00

Plagioclase

Sample	92-87	92-87	HLC92-11B	GB92-8
Sample Pt.	PL-C-4 CORE	PL-C-4 RIM	PL-C-1 RIM	PL-B-4 RIM
SiO2	58.38	58.58	59.35	56.41
Al2O3	26.90	27.09	1.32	26.47
FeO	0.04	0.05 N	N	
CaO	7.83	7.98	7.44	10.70
Na2O	6.71	6.59	8.17	6.16
K2O	0.09	0.06	0.11	0.92
Total	99.95	100.35	100.01	100.66
Si	2.61	2.60	2.66	2.54
Al	1.42	1.42	1.32	1.41
Fe	0.00	0.00	0.00	0.00
Ca	0.37	0.38	0.36	0.52
Na	0.58	0.57	0.71	0.54
K	0.01	0.00	0.01	0.05
XAn	0.39	0.40	0.33	0.49
Sum Cations	4.98	4.97	5.04	5.05
No. Oxygens	8.00	8.00	8.00	8.00

Plagioclase

Sample	91-84	91-84	92-87	91-70
Sample Pt.	PL-A-2 RIM	PL-C-6 RIM	PL-A-4 RIM	PL-A-1 RIM
SiO2	62.06	61.97	57.35	65.36
Al2O3	24.70	24.62	27.90	21.34
FeO				0.08
	N	N	N	
CaO	5.36	5.01	9.03	2.11
Na2O	8.03	7.74	5.79	10.13
K2O	0.10	0.07	0.03	0.09
Total	100.25	99.41	100.10	99.10
Si	2.74	2.75	2.56	2.89
Al	1.28	1.29	1.47	1.11
Fe	0.00	0.00	0.00	0.00
Ca	0.25	0.24	0.43	0.10
Na	0.69	0.67	0.50	0.87
K	0.01	0.00	0.00	0.01
XAn	0.27	0.26	0.46	0.10
Sum Cations	4.97	4.94	4.96	4.99
No. Oxygens	8.00	8.00	8.00	8.00

Plagioclase

Sample	91-136	91-136	92-5D	91-80
Sample Pt.	PL-A-1	PL-D-1	PL-B-1	PL-C-3
	RIM	RIM	RIM	RIM
SiO2	60.56	60.94	61.82	61.74
Al2O3	24.64	25.32	24.27	24.49
FeO	0.13	0.15	0.00	0.03
CaO	6.57	5.42	4.89	5.23
Na2O	7.72	8.43	8.43	7.81
K2O	0.03	0.05	0.00	0.12
Total	99.65	100.31	99.46	99.42
Si	2.70	2.70	2.75	2.74
Al	1.30	1.32	1.27	1.28
Fe	0.01	0.01	0.00	0.00
Ca	0.31	0.26	0.23	0.25
Na	0.67	0.72	0.73	0.67
K	0.00	0.00	0.00	0.01
XAn	0.32	0.26	0.24	0.27
Sum Cations	4.99	5.01	4.98	4.96
No. Oxygens	8.00	8.00	8.00	8.00

Ilmenite

Sample	92-5D ILM-A-6	92-5D ILM-C-2
SiO2	0.85	1.52
TiO2	50.31	50.34
Al2O3	0.08	0.09
Cr2O3	0.30	0.31
Fe2O3	1.73	0.64
FeO	45.17	46.29
MnO	0.81	0.80
MgO	0.09	0.00
CaO	0.05	0.00
Total	99.39	99.98
Si	0.04	0.08
Ti	1.92	1.90
Al	0.01	0.01
Cr	0.01	0.01
Fe3	0.07	0.02
Fe2	1.91	1.95
Mn	0.04	0.03
Mg	0.01	0.00
Ca	0.00	0.00
Sum Cations	4.00	4.00
No. Oxygens	6.00	6.00

Staurolite

Sample	HLC-11B	HLC-11B	92-5D	92-5D
Sampel Pt.	ST-A-3/BLEB	ST-B-3/BLEB	ST-A-2-BLEB	ST-B-3/30U
SiO2	26.79	27.06	28.37	28.09
Al2O3	56.05	55.93	55.31	55.80
TiO2	0.72	0.85	0.85	0.76
FeO	11.28	11.62	12.59	13.05
MnO	0.09	0.06	0.10	0.09
MgO	1.93	1.92	1.74	1.23
ZnO	1.51	1.45	0.54	0.45
Total	98.37	98.89	99.50	99.47
Si	7.37	7.73	8.04	7.94
Al	18.17	18.84	18.47	18.66
Ti	0.15	0.18	0.18	0.16
Fe	2.59	2.78	2.98	3.10
Mn	0.02	0.02	0.02	0.02
Mg	0.79	0.82	0.74	0.52
Zn	0.31	0.31	0.11	0.10
XMg	23.39	22.75	19.77	14.37
Sum Cations	29.40	30.67	30.55	30.53
No. Oxygens	46.00	46.00	46.00	46.00

Staurolite

Sample	92-5D	91-70	91-70	91-136
Sampel Pt.	ST-B-CORE	ST-A-2/COR	ST-A-3/RIM	ST-A-1/RIM
SiO2	27.92	27.39	27.36	30.04
Al2O3	55.49	53.91	53.53	53.10
TiO2	0.76	0.75	0.69	0.73
FeO	13.43	11.38	11.24	13.59
MnO	0.06	0.30	0.28	0.13
MgO	2.03	1.64	1.63	1.10
ZnO	0.41	1.53	1.60	0.36
Total	100.10	96.90	96.33	99.05
Si	7.90	7.99	8.03	8.56
Al	18.50	18.53	18.51	17.84
Ti	0.16	0.16	0.15	0.16
Fe	3.18	2.78	2.76	3.24
Mn	0.01	0.07	0.07	0.03
Mg	0.86	0.71	0.71	0.47
Zn	0.09	0.33	0.35	0.08
XMg	21.23	20.44	20.55	12.60
Sum Cations	30.69	30.58	30.57	30.37
No. Oxygens	46.00	46.00	46.00	46.00

Staurolite

Sample	91-136	91-80
Sampel Pt.	ST-A-8/COR	ST-A-1/RIM
SiO2	29.18	28.04
Al2O3	50.51	54.66
TiO2	0.67	0.61
FeO	14.49	12.17
MnO	0.13	0.17
MgO	2.39	1.15
ZnO	0.38	1.29
Total	97.75	98.09
Si	8.50	7.74
Al	17.35	17.79
Ti	0.15	0.13
Fe	3.53	2.81
Mn	0.03	0.04
Mg	1.04	0.47
Zn	0.08	0.26
XMg	22.72	14.43
Sum Cations	30.68	29.24
No. Oxygens	46.00	46.00

The following mineral analysis are arranged by sample number.
Phase abbreviations follow Kretz, 1983.
Analysis from Sample 91-136

Sample	91-136	91-136	91-136	91-136	91-136	91-136	91-136	91-136	91-136	91-136	91-136	91-136
Phase	Pl	Pl	Pl	Pl	Pl	Pl	Pl	Pl	Pl	Pl	Pl	Pl
Phase Pt.	Pl-A-1	Pl-A-2	Pl-A-3	Pl-A-4	Pl-A-5	Pl-A-6	Pl-A-7	Pl-A-8	Pl-A-10	Pl-A-11	Pl-B-1	Pl-B-2
Location	Rim	50um Rim	100um Rim	175um Rim	300um Rim	475um Rim	650um Rim	1.2mm C	Rim	Rim	Center	Center
SiO2	60.56	61.01	60.74	60.80	60.40	60.21	60.34	60.53	61.70	60.03	60.37	59.69
Al2O3	24.64	24.75	24.93	24.98	24.85	25.21	25.08	24.99	24.29	25.01	24.55	24.56
FeO	0.13	0.07	0.00	0.00	0.00	0.02	0.09	0.04	0.22	0.18	0.08	0.05
CaO	6.57	6.46	6.58	6.46	6.74	6.57	6.79	6.53	5.59	6.40	6.26	6.65
K2O	0.03	0.14	0.12	0.19	0.09	0.19	0.20	0.09	0.04	0.11	0.18	0.09
Na2O	7.72	7.89	7.67	7.79	7.78	7.64	7.80	7.82	8.45	8.00	8.04	7.94
Total	99.65	100.31	100.05	100.22	99.87	99.83	100.29	100.00	100.29	99.73	99.47	98.97

Sample	91-136	91-136	91-136	Sample	91-136	91-136	91-136	Sample	91-136	Sample	91-136	91-136
Phase	Pl	Pl	Pl	Phase	Ms	Ms	Ms	Phase	Ms	Phase	St	St
Phase Pt.	Pl-B-4	Pl-B-5	Pl-B-6	Phase Pt.	Ms-A-1	Ms-A-2	Ms-B-1	Phase Pt.	Ms-B-2	Phase Pt.	St-A-1	St-A-2
Location	Rim	Rim	Rim	Location	Center	Rim	Center	Location	Rim	Location	Rim	200um Rim
SiO2	60.29	60.46	60.65	SiO2	46.81	47.53	47.15	SiO2	47.72	SiO2	30.04	29.71
Al2O3	24.59	24.70	24.87	TiO2	0.68	0.74	0.72	TiO2	0.73	Al2O3	53.10	51.40
FeO	0.05	0.02	0.08	Cr2O3	0.15	0.00	0.21	Cr2O3	0.16	TiO2	0.73	0.64
CaO	6.63	6.56	6.54	Al2O3	36.20	36.34	36.21	Al2O3	36.56	FeO	13.59	14.03
K2O	0.05	0.13	0.21	CaO	0.00	0.00	0.00	CaO	0.00	MgO	1.10	2.01
Na2O	7.83	7.81	7.78	MnO	0.00	0.00	0.00	MnO	0.00	MnO	0.13	0.16
				MgO	0.69	0.85	0.75	MgO	0.71	ZnO	0.36	0.41
Total	99.44	99.67	100.13	K2O	9.64	9.74	10.10	K2O	10.24			
				FeO	2.73	3.14	3.14	FeO	3.02	Total	99.06	98.36
				Na2O	1.09	1.17	1.13	Na2O	1.10			
				Total	98.01	99.53	99.41	Total	100.23			

Sample	91-136	91-136	91-136	91-136	91-136	91-136
Phase	St	St	St	St	St	St
Phase Pt.	St-A-3	St-A-4	St-A-5	St-A-6	St-A-7	St-A-11
Location	50um Rim	250um Rim	700um Rim	Center	2.5mm Rim	Rim
SiO2	29.54	29.89	30.10	29.34	28.90	28.90
Al2O3	52.37	51.95	52.60	51.78	51.16	52.20
TiO2	0.68	0.69	0.59	0.67	0.61	0.69
FeO	14.09	13.63	13.78	14.16	14.42	13.49
MgO	1.34	1.57	1.82	2.17	2.35	1.28
MnO	0.16	0.12	0.06	0.12	0.10	0.16
ZnO	0.35	0.32	0.35	0.36	0.30	0.47
Total	98.52	98.17	99.28	98.60	97.84	97.17

Sample	91-136	91-136	91-136	91-136	91-136	91-136	91-136	91-136	91-136	91-136
Phase	St	St	St	St	St	St	St	St	St	St
Phase Pt.	St-B-1	St-B-2	St-B-3	St-B-4	St-A2-1	St-A2-2	St-A2-3	St-A2-4	St-A2-5	St-A2-6
Location	Rim	Center	N-Rim	E-Rim	Rim	30um Rim	50um Rim	100um Rim	120um Rim	200um Rim
SiO2	30.10	29.82	29.64	29.56	0.46	0.33	0.38	0.29	0.28	0.31
Al2O3	52.56	51.43	52.15	52.42	27.73	27.54	27.66	27.09	27.63	26.96
TiO2	0.74	0.66	0.61	0.68	55.58	53.97	55.82	52.14	54.02	52.85
FeO	14.05	12.68	13.66	14.00	0.62	0.70	0.59	0.71	0.68	0.70
MgO	1.51	2.28	1.75	0.10	0.08	0.13	0.08	0.05	0.07	0.07
MnO	0.10	0.16	0.12	0.34	13.11	13.31	13.22	13.78	13.96	13.75
ZnO	0.38	0.25	0.41	0.34	1.09	1.10	1.13	1.59	1.88	1.69
Total	99.44	97.27	98.34	98.79	98.68	97.09	98.89	95.66	98.53	96.34

Sample	91-136	91-136	91-136	91-136	91-136	91-136	91-136
Phase	St	St	St	St	St	St	St
Phase Pt.	St-A2-7	St-A2-8	St-A2-9	St-A2-10	St-A2-11	St-A2-12	
Location	220um Rim	430um Rim	530um Rim	630um Rim	780um Rim	950um Rim	
SiO2	0.29	0.37	0.34	0.34	0.29	0.25	
Al2O3	27.87	27.87	27.79	28.20	27.90	27.76	
TiO2	54.11	54.92	53.04	54.86	53.19	55.63	
FeO	0.64	0.62	0.71	0.63	0.68	0.64	
MgO	0.07	0.12	0.08	0.09	0.11	0.04	
MnO	14.01	13.76	13.49	13.30	13.66	13.63	
ZnO	1.86	1.46	2.04	1.42	2.05	1.45	
Total	98.85	99.11	97.50	98.84	97.86	99.42	

Sample	91-136	91-136	91-136
Phase	St	St	St
Phase Pt.	St-A2-13	St-A2-14	St-A2-15
Location	1250um Rim	1350um Rim	1650um Rim
SiO2	0.32	0.32	0.22
Al2O3	27.57	27.56	27.57
TiO2	52.01	53.39	52.88
FeO	0.70	0.58	0.69
MgO	0.07	0.08	0.09
MnO	13.46	13.50	14.24
ZnO	2.00	2.27	2.16
Total	96.13	97.70	97.84

Sample	91-136	91-136
Phase	St	St
Phase Pt.	St-A2-16	St-A2-17
Location	1800um Rim	2200um Rim
SiO2	0.32	0.31
Al2O3	27.29	26.46
TiO2	53.10	51.25
FeO	0.60	0.64
MgO	0.07	0.12
MnO	13.58	13.39
ZnO	2.18	2.20
Total	97.13	94.36

Sample	91-136	91-136	91-136	91-136	91-136
Phase	Bt	Bt	Bt	Bt	Bt
Phase Pt.	Bt-A-2	Bt-A-3	Bt-B-1	Bt-B-2	Bt-C-1
Location	Center	Edge	Center	Edge	Center
F	0.00	0.61	0.00	0.67	0.24
SiO2	36.34	36.08	35.62	34.84	36.45
Al2O3	18.68	18.98	19.03	18.47	19.25
TiO2	2.40	2.28	1.56	1.69	1.90
MnO	0.07	0.04	0.05	0.02	0.05
MgO	11.21	11.39	11.73	12.52	11.36
FeO	19.02	19.19	18.15	19.41	18.41
CaO	0.00	0.03	0.04	0.00	0.00
Na2O	0.43	0.32	0.40	0.17	0.29
K2O	8.70	8.81	8.50	8.04	9.02

Sample	91-136	91-136
Phase	Bt	Bt
Phase Pt.	Bt-C-2	Bt-C-3
Location	Center	Edge
F	0.13	0.06
SiO2	36.13	36.05
Al2O3	18.90	19.21
TiO2	2.04	2.09
MnO	0.04	0.01
MgO	11.39	11.14
FeO	18.35	17.14
CaO	0.00	0.00
Na2O	0.31	0.14
K2O	8.96	9.23
Total	96.23	95.08

Sample	91-136	91-136	91-136	91-136
Phase	Grt	Grt	Grt	Grt
Phase Pt.	Grt-B-1	Grt-B-2	Grt-B-3	Grt-B-4
Location	Rim	8um Rim	20um Rim	50um Rim
SiO2	37.52	39.05	38.86	39.06
Al2O3	20.96	21.58	22.03	22.08
TiO2	0.03	0.06	0.05	0.01
FeO	31.15	31.72	31.49	31.76
MgO	3.32	3.32	3.77	3.92
MnO	1.40	1.39	1.35	1.36
CaO	2.64	2.64	2.41	2.34
Cr2O3	0.31	0.30	0.00	0.00
V2O5	0.00	0.01	0.03	0.04
Total	97.32	100.07	100.00	100.58

Sample	91-136	91-136	91-136	91-136	91-136
Phase	Grt	Grt	Grt	Grt	Grt
Phase Pt.	Grt-B-5	Grt-B-6	Grt-B-7	Grt-B-8	Grt-B-9
Location	100um Rim	150um Rim	230um Rim	290um Rim	350um Rim
SiO2	39.55	39.35	39.01	39.27	39.16
Al2O3	22.20	22.17	22.10	22.26	21.72
TiO2	0.04	0.03	0.05	0.01	0.01
FeO	30.91	30.68	30.75	31.12	30.07
MgO	4.12	4.22	4.15	4.23	4.23
MnO	1.57	1.80	1.84	1.87	2.03
CaO	2.43	2.28	2.04	2.15	2.36
Cr2O3	0.00	0.00	0.09	0.07	0.30
V2O5	0.02	0.00	0.04	0.01	0.02
Total	100.85	100.52	100.60	100.98	99.91

Sample	91-136	91-136	91-136	91-136	91-136	91-136	91-136	91-136	91-136	91-136	91-136	91-136
Phase	Grt	Grt	Grt	Grt	Grt	Grt	Grt	Grt	Grt	Grt	Grt	Grt
Phase Pt.	Grt-B-10	Grt-B-11	Grt-B-12	Grt-B-13	Grt-B-14	Grt-B-15	Grt-B-16	Grt-B-17	Grt-B-18	Grt-B-19	Grt-B-20	Grt-B-21
Location	390um Rim	425um Rim	500um Rim	550um Rim	600um Rim	650um Rim	700um rim	750um Rim	800um Rim	850um Rim	950um Rim	1000um Rim
SiO2	39.12	39.58	39.32	39.20	39.37	38.76	38.90	38.77	38.74	38.82	39.00	38.78
Al2O3	21.89	22.00	22.10	22.11	21.92	21.37	21.57	21.78	21.40	21.58	21.78	21.96
TiO2	0.00	0.00	0.00	0.02	0.00	0.02	0.00	0.00	0.00	0.00	0.00	0.00
FeO	30.16	30.22	30.21	30.01	30.79	29.97	30.26	29.96	29.41	30.13	30.09	30.14
MgO	4.24	4.07	4.07	4.10	4.14	3.95	4.01	3.91	3.96	3.84	3.99	4.04
MnO	2.00	2.29	2.25	2.24	2.34	2.31	2.31	2.34	2.31	2.26	2.24	2.35
CaO	2.35	2.37	2.47	2.48	2.35	2.40	2.40	2.19	2.46	2.60	2.42	2.35
Cr2O3	0.13	0.13	0.00	0.00	0.12	0.10	0.08	0.12	0.03	0.06	0.22	0.00
Total	99.89	100.66	100.42	100.16	101.03	98.87	99.52	99.08	98.32	98.85	99.74	99.62

Sample	91-136	91-136	91-136	91-136	91-136	91-136	91-136
Phase	Grt	Grt	Grt	Grt	Grt	Grt	Grt
Phase Pt.	Grt-B-22	Grt-B-23	Grt-B-25	Grt-B-26	Grt-B-27	Grt-B-28	Grt-B-29
Location	1050um Rim	1100um Rim	1200um Rim	1225um Rim	1250um Rim	1300um Rim	1350um Rim
SiO2	38.42	39.13	39.15	39.32	38.75	38.83	38.83
Al2O3	21.79	22.19	22.00	21.93	21.61	21.76	21.81
TiO2	0.00	0.00	0.00	0.00	0.00	0.00	0.00
FeO	30.07	29.65	30.97	30.68	31.14	30.70	31.84
MgO	4.09	3.95	4.11	4.13	3.96	3.64	3.06
MnO	2.20	2.13	1.80	1.72	1.38	1.38	1.51
CaO	2.41	2.45	1.96	2.40	2.58	2.49	2.77
Cr2O3	0.00	0.00	0.04	0.00	0.10	0.00	0.13
Total	98.98	99.51	100.03	100.19	99.52	98.79	99.95

Sample	91-136	91-136	91-136	91-136
Phase	Grt	Grt	Grt	Grt
Phase Pt.	Grt-C-15	Grt-C-15B	Grt-C-16	Grt-C-17
Location	7um Rim	Rim	20um	40um Rim
SiO2	38.85	39.02	38.40	39.40
Al2O3	21.54	21.52	21.66	21.81
TiO2	0.00	0.00	0.00	0.00
FeO	30.17	31.00	30.65	30.82
MgO	3.82	3.82	4.00	4.10
MnO	1.33	1.34	1.39	1.50
CaO	2.66	2.78	2.70	2.85
Cr2O3	0.00	0.00	0.00	0.13
ZnO	0.00	0.01	0.00	0.02
Total	98.37	99.48	98.79	100.64

Sample	91-136	91-136	91-136	91-136	91-136	91-136	91-136	91-136	91-136	91-136	91-136	91-136
Phase	Grt	Grt	Grt	Grt	Grt	Grt	Grt	Grt	Grt	Grt	Grt	Grt
Phase Pt.	Grt-C-18	Grt-C-19	Grt-C-20	Grt-C-21	Grt-C-22	Grt-C-23	Grt-C-24	Grt-C-25	Grt-C-27	Grt-C-28	Grt-C-29	Grt-C-30
Location	50um Rim	70um Rim	90um Rim	110um Rim	130um Rim	170um Rim	195um Rim	220um Rim	300um Rim	310um Rim	320um Rim	325um Rim
SiO2	38.74	39.49	38.98	39.56	39.46	39.43	39.35	39.48	39.67	39.60	39.33	39.69
Al2O3	22.14	21.67	21.96	21.97	22.08	22.17	21.79	22.00	21.99	21.81	22.05	21.95
TiO2	0.00	0.00	0.00	0.00	0.00	0.00	0.00	0.00	0.00	0.00	0.00	0.00
FeO	30.58	30.15	30.05	30.95	31.02	30.87	30.02	30.32	29.98	30.03	30.64	29.88
MgO	4.16	4.19	4.12	4.18	4.28	4.14	4.14	4.13	4.05	4.13	4.25	4.33
MnO	1.48	1.58	1.52	1.60	1.76	1.84	1.90	1.99	2.13	2.06	2.18	2.20
CaO	2.73	2.82	2.76	2.54	2.25	2.54	2.54	2.71	2.52	2.55	2.52	2.47
Cr2O3	0.11	0.00	0.00	0.01	0.00	0.00	0.00	0.00	0.09	0.00	0.00	0.10
ZnO	0.01	0.00	0.01	0.00	0.01	0.00	0.00	0.03	0.00	0.01	0.01	0.00
Total	99.94	99.89	99.39	100.81	100.86	100.98	99.74	100.66	100.44	100.18	100.99	100.63

Sample	91-136	91-136	91-136	91-136	91-136	91-136	91-136	91-136	91-136	91-136	91-136	91-136
Phase	Grt	Grt	Grt	Grt	Grt	Grt	Grt	Grt	Grt	Grt	Grt	Grt
Phase Pt.	Grt-C-31	Grt-C-33	Grt-C-34	Grt-C-35	Grt-C-36	Grt-C-37	Grt-C-38	Grt-C-39	Grt-C-40	Grt-C-41	Grt-C-42	Grt-C-43
Location	380um Rim	430um Rim	450um Rim	490um Rim	540um Rim	600um Rim	650um Rim	700um Rim	750um Rim	800um Rim	850um Rim	900um Rim
SiO2	39.22	39.22	39.73	38.81	39.45	39.44	39.27	39.74	39.76	39.14	39.52	39.48
Al2O3	21.35	21.95	22.02	21.92	21.85	21.90	22.04	21.90	21.76	21.67	22.02	21.95
TiO2	0.00	0.00	0.00	0.00	0.00	0.00	0.00	0.00	0.00	0.00	0.01	0.00
FeO	30.22	30.23	30.66	29.50	30.86	30.18	29.84	30.83	30.64	30.33	31.11	30.90
MgO	4.30	4.31	4.22	4.45	4.28	4.24	4.27	4.25	4.25	4.22	4.19	4.24
MnO	2.01	2.29	2.05	2.01	2.14	2.12	2.15	2.16	2.01	2.09	2.18	2.03
CaO	2.52	2.49	2.61	2.49	2.42	2.55	2.51	2.40	2.42	2.52	2.62	2.51
Cr2O3	0.00	0.07	0.00	0.03	0.06	0.00	0.00	0.11	0.09	0.04	0.00	0.00
ZnO	0.00	0.03	0.01	0.01	0.00	0.00	0.00	0.00	0.00	0.03	0.01	0.00
Total	99.64	100.58	101.29	99.22	101.06	100.42	100.08	101.38	100.92	100.04	101.67	101.12

Sample	91-136	91-136	91-136	91-136	91-136	91-136	91-136	91-136	91-136	91-136	91-136	91-136
Phase	Grt	Grt	Grt	Grt	Grt	Grt	Grt	Grt	Grt	Grt	Grt	Grt
Phase Pt.	Grt-C-44	Grt-C-45	Grt-C-46	Grt-C-47	Grt-C-48	Grt-C-49	Grt-C-50	Grt-C-51	Grt-C-52	Grt-D-1	Grt-D-2	Grt-D-3
Location	950um Rim	1050um Rim	1075um Rim	1100um Rim	1150um Rim	1200um Rim	1225um Rim	1240um Rim	1260um Rim	Rim	10um Rim	23um Rim
SiO2	39.58	39.39	39.88	39.00	39.62	39.30	39.63	39.20	39.61	40.13	39.56	39.39
Al2O3	21.85	21.98	21.94	21.89	22.22	21.91	22.17	21.96	22.40	21.50	21.82	22.01
TiO2	0.00	0.00	0.00	0.00	0.00	0.00	0.01	0.00	0.00	0.00	0.00	0.00
FeO	30.70	30.11	30.67	30.46	30.77	30.82	30.95	31.64	31.47	30.78	31.10	31.31
MgO	4.23	4.22	4.18	4.25	4.25	4.00	4.06	3.91	3.79	3.86	3.97	4.13
MnO	2.02	1.96	1.91	1.81	1.61	1.53	1.31	1.32	1.22	1.33	1.25	1.34
CaO	2.52	2.56	2.59	2.62	2.38	2.83	2.92	2.74	2.75	2.71	2.72	2.78
Cr2O3	0.04	0.07	0.00	0.02	0.07	0.00	0.00	0.17	0.05	0.00	0.00	0.02
ZnO	0.01	0.02	0.00	0.01	0.00	0.00	0.00	0.00	0.02	0.01	0.03	0.00
Total	100.95	100.30	101.18	100.05	100.92	100.39	101.06	100.94	101.31	100.32	100.45	100.98

Sample	91-136	91-136	91-136	91-136	91-136	91-136	91-136	91-136	91-136
Phase	Grt	Grt	Grt	Grt	Grt	Grt	Grt	Grt	Grt
Phase Pt.	Grt-D-4	Grt-D-5	Grt-D-6	Grt-D-7	Grt-D-8	Grt-D-9	Grt-D-10	Grt-D-11	Grt-D-12
Location	100um Rim	155um Rim	250um Rim	350um Rim	400um Rim	500um Rim	600um Rim	700um Rim	750um Rim
SiO2	39.79	37.60	39.48	38.76	39.36	39.40	39.61	39.29	39.63
Al2O3	22.20	21.42	21.91	22.02	21.69	22.27	22.13	22.14	21.89
TiO2	0.00	0.00	0.00	0.01	0.00	0.00	0.00	0.00	0.00
FeO	31.72	30.33	31.38	31.13	30.51	30.94	31.35	31.33	31.73
MgO	4.15	4.31	4.49	4.44	4.36	4.41	4.60	4.46	4.07
MnO	1.38	1.45	1.61	1.71	1.83	1.72	1.79	1.58	1.31
CaO	2.81	2.44	2.56	2.63	2.59	2.47	2.12	2.45	2.62
Cr2O3	0.00	0.00	0.10	0.18	0.00	0.00	0.06	0.00	0.00
ZnO	0.00	0.01	0.00	0.01	0.00	0.00	0.00	0.00	0.01
Total	102.05	97.56	101.52	100.89	100.34	101.22	101.66	101.24	101.26

Analysis from Sample 91-176

Sample	91-176	91-176	91-176	91-176	Sample	91-176	91-176	91-176	91-176	91-176	91-176	91-176
Phase	Grt	Grt	Grt	Grt	Phase	Bt	Bt	Hbl	Hbl	Hbl	Hbl	Hbl
Phase Pt.	Grt-A-1	Grt-A-2	Grt-B-1	Grt-B-2	Phase Pt.	Bt-A-1	Bt-A-2	Hbl-A-1	Hbl-A-2	Hbl-A-3	Hbl-B-1	Hbl-B-2
Location	Center	Rim	Center	Edge	Location	Edge	Edge	Edge	Edge	Interior	Edge	Edge
Cl	0.02	0.02	0.00	0.00	Cl	0.00	0.03	0.03	0.00	0.05	0.00	0.00
F	0.00	0.00	0.00	0.00	F	0.00	0.00	0.26	0.29	0.34	1.12	0.00
SiO2	37.65	37.51	37.83	37.46	SiO2	34.55	34.61	38.29	38.98	38.44	38.74	39.25
Al2O3	21.04	21.07	21.18	20.99	Al2O3	17.75	17.85	14.07	14.21	14.59	13.97	14.99
TiO2	0.50	0.04	0.18	0.04	TiO2	1.44	1.36	1.02	1.08	0.93	0.76	0.83
MnO	2.96	2.93	2.83	2.75	MnO	0.19	0.21	0.33	0.27	0.27	0.24	0.25
MgO	0.56	0.53	0.54	0.50	MgO	4.22	4.18	2.78	2.76	2.47	2.97	2.85
FeO	25.21	25.17	25.20	25.60	FeO	28.35	27.85	26.18	26.49	26.30	26.22	26.13
CaO	11.59	10.77	11.35	10.90	CaO	0.05	0.02	11.27	11.16	10.98	11.41	11.04
K2O	0.00	0.00	0.00	0.00	K2O	8.90	8.92	1.81	1.70	1.65	1.77	1.71
Na2O	0.00	0.00	0.00	0.00	Na2O	0.00	0.00	1.27	1.19	1.03	1.14	1.26
Total	99.54	98.04	99.11	98.25	Total	95.45	95.03	97.30	98.13	97.04	98.35	98.31

Analysis from Sample GB-8

Sample	GB-8	GB-8	GB-8	GB-8	GB-8	GB-8	GB-8	Sample	GB-8
Phase	Grt	Grt	Grt	Grt	Grt	Grt	Grt	Phase	CPX
Phase Pt.	Grt-A-1	Grt-A-2	Grt-A-3	Grt-A-4	Grt-A-5	Grt-B-1	Grt-B-4	Phase Pt.	CPX-A-5
Location	Rim	Rim	Rim	Core	Core	Rim	Center	Location	Edge
SiO2	37.81	37.82	38.42	37.76	38.02	38.03	38.08	SiO2	50.84
Al2O3	21.61	21.00	21.70	21.15	21.31	21.97	21.18	Al2O3	0.57
TiO2	0.00	0.19	0.00	0.18	0.19	0.19	0.00	TiO2	0.08
MnO	3.00	2.86	2.92	2.83	3.35	3.57	3.61	FeO	15.59
CaO	16.45	16.81	17.26	18.29	18.84	17.51	13.41	MgO	9.25
FeO	21.50	21.50	21.70	20.00	19.22	19.47	23.34	MnO	0.26
MgO	0.68	0.67	0.65	0.49	0.50	0.59	0.86	CaO	23.29
								Na2O	0.25
Total	101.04	100.84	101.65	100.70	101.23	101.35	100.48	Total	100.13

Analysis from Sample 91-70

Sample	91-70	91-70	91-70	91-70	91-70
Phase	Bt	Bt	Bt	Bt	Bt
Phase Pt.	Bt-A-1	Bt-A-2	Bt-A-3	Bt-B-1	Bt-C-2
Location	Center	Center	Edge	Center	Edge
F	0.65	0.44	0.25	0.31	0.14
SiO2	36.42	35.84	36.56	36.09	36.20
Al2O3	18.81	18.71	19.02	18.56	19.03
TiO2	2.37	2.39	1.87	2.29	2.62
MnO	0.16	0.11	0.19	0.11	0.16
MgO	11.73	11.48	11.41	11.20	11.06
FeO	18.34	17.95	18.20	17.58	18.25
CaO	0.00	0.00	0.03	0.00	0.00
K2O	0.21	0.25	0.16	0.18	0.16
Na2O	9.82	9.82	9.96	9.31	9.60
Total	98.51	96.99	97.65	95.64	97.22

Sample	91-70	91-70	91-70
Phase	Grt	Grt	St
Phase Pt.	Grt-B-1	Grt-B-2	St-A-3
Location	Rim	Rim	Center
SiO2	37.40	36.39	27.36
Al2O3	22.10	22.24	53.53
TiO2	0.16	0.15	0.69
FeO	32.72	33.11	1.63
MgO	3.97	3.93	11.24
MnO	4.45	4.40	0.28
CaO	0.64	0.69	1.60
Total	101.44	101.20	96.32

Sample	91-70	91-70	91-70
Phase	Grt	Grt	Grt
Phase Pt.	Grt-B-1	Grt-C-1	Grt-C-2
Location	Core	Rim	Rim
SiO2	36.77	36.06	35.62
Al2O3	21.64	20.87	21.14
TiO2	0.05	0.06	0.07
FeO	32.43	33.30	32.82
MgO	4.36	4.11	3.89
MnO	4.40	4.44	4.44
CaO	0.64	0.67	0.63
Total	100.29	99.49	98.61

Sample	91-70
Phase	Pl
Phase Pt.	Pl-A-1
Location	Rim
SiO2	65.36
Al2O3	21.34
TiO2	0.08
MgO	2.11
FeO	0.09
MnO	10.13
ZnO	
Total	99.10

Sample	91-70	91-70
Phase	St	St
Phase Pt.	St-A-1	St-A-2
Location	Center	Center
SiO2	27.39	27.39
Al2O3	53.86	53.91
TiO2	0.74	0.75
MgO	1.65	1.64
FeO	11.80	11.38
MnO	0.28	0.30
ZnO	1.60	1.53
Total	97.31	96.91

Analysis from Sample 91-80

Sample	91-80	91-80	91-80	91-80	91-80	91-80	91-80
Phase	Grt	Grt	Grt	Grt	Grt	Grt	Grt
Phase Pt.	Grt-A-1	Grt-A-2	Grt-A-3	Grt-A-4	Grt-A-5	Grt-A-19	Grt-A-20
Location	Rim	5um Rim	10um Rim	20um Rim	30um Rim	Center	Center
Cl	0.00	0.00	0.01	0.02	0.02	0.00	0.00
F	0.00	0.00	0.09	0.00	0.00	0.11	0.00
SiO2	37.53	37.53	37.64	38.04	37.52	37.34	37.57
Al2O3	21.63	21.87	21.74	21.74	21.50	21.83	21.66
TiO2	0.19	0.13	0.23	0.17	0.04	0.08	0.03
MnO	1.57	1.65	1.73	1.65	1.91	2.21	2.19
MgO	3.43	3.54	3.67	3.75	3.79	4.20	4.07
FeO	33.41	32.96	33.68	32.64	33.10	31.80	31.87
CaO	1.86	1.87	1.85	1.83	1.79	1.69	1.69
K2O	0.00	0.00	0.00	0.00	0.00	0.00	0.00
Na2O	0.00	0.00	0.00	0.00	0.00	0.04	0.00
Total	99.61	99.54	100.64	99.84	99.67	98.84	99.08

Sample	91-80	91-80	91-80	91-80	91-80	91-80	91-80
Phase	Pl	Pl	Pl	Pl	Pl	Pl	Pl
Phase Pt.	Pl-A-2	Pl-A-3	Pl-A-4	Pl-C-1	Pl-C-2	Pl-C-3	Pl-C-4
Location	5um Rim	Center	Rim	Center	Center	5um Rim	Rim
SiO2	61.46	61.52	61.80	61.24	60.48	61.74	61.20
Al2O3	24.18	25.34	24.40	25.04	24.88	24.49	24.74
FeO	0.04	0.02	0.00	0.00	0.00	0.03	0.02
CaO	5.26	6.02	4.93	5.77	5.71	5.23	5.25
K2O	0.40	0.46	0.29	0.04	0.41	0.12	0.16
Na2O	7.97	7.61	8.02	7.27	7.41	7.81	8.13
Total	99.31	100.96	99.44	99.36	98.89	99.41	99.49

Sample	91-80	91-80	91-80	91-80	91-80
Phase	St	St	St	St	St
Phase Pt.	St-A-1	St-A-2	St-A-3	St-B-1	St-C-1
Location	Rim	Center	Rim	Bleb	Bleb
SiO2	28.04	27.38	27.67	27.38	27.50
Al2O3	54.66	53.49	55.41	53.45	54.05
TiO2	0.61	0.66	0.70	0.71	0.69
MgO	1.15	1.29	1.12	1.35	1.38
FeO	12.17	12.76	12.08	12.28	12.14
MnO	0.17	0.11	0.11	0.14	0.12
ZnO	1.29	1.21	1.34	1.64	1.37
Total	98.08	96.89	98.44	96.94	97.25

Sample	91-80	91-80
Phase	Bt	Bt
Phase Pt.	Bt-B-1	Bt-B-2
Location	Center	Center
F	0.43	0.77
SiO2	35.07	35.32
Al2O3	18.73	18.55
TiO2	2.66	2.49
MnO	0.07	0.05
MgO	9.67	10.10
FeO	19.57	18.93
CaO	0.00	0.00
K2O	8.91	8.90
Na2O	0.32	0.28
Total	95.42	95.38

Sample	91-80	91-80
Phase	Bt	Bt
Phase Pt.	Bt-B-3	Bt-C-1
Location	Edge	Edge
F	0.23	0.00
SiO2	35.23	35.28
Al2O3	17.27	19.10
TiO2	2.58	2.74
MnO	0.07	0.08
MgO	9.90	9.64
FeO	19.70	19.49
CaO	0.00	0.04
K2O	9.12	8.84
Na2O	0.18	0.30
Total	94.29	95.51

Sample	91-167	91-167	91-167
Phase	Grt	Bt	Bt
Phase Pt.	Grt-A-1	Bt-A-1	Bt-A-2
Location	Rim	Rim	Rim
Cl	0.02	0.00	0.00
F	0.00	0.22	0.59
SiO2	37.65	36.16	36.53
Al2O3	21.49	17.57	19.96
TiO2	0.09	1.93	2.06
MnO	3.12	0.24	0.24
MgO	2.38	10.29	10.48
FeO	28.21	20.22	19.89
CaO	5.11	0.00	0.06
K2O	0.00	9.45	9.35
Na2O	0.00	0.07	0.06
Total	98.06	96.15	97.22

Analysis from Sample 91-80

Sample	91-84	91-84	91-84	91-84	91-84	91-84	91-84	91-84	91-84	91-84	Sample	91-84
Phase	Grt	Grt	Grt	Grt	Grt	Grt	Grt	Grt	Grt	Grt	Phase	Pl
Phase Pt.	Grt-A-1	Grt-A-2	Grt-A-3	Grt-A-4	Grt-A-5	Grt-B-1	Grt-B-2	Grt-B-3	Grt-B-4	Grt-B-5	Phase Pt.	Pl-A-1
Location	Geo. Center	Geo. Center	Rim	Rim	Rim	Geo. Center	Geo. Center	Rim	Rim	Rim	Location	Geo. Center
SiO2	38.84	39.05	38.42	38.73	38.92	39.01	38.50	39.03	38.80	38.80	SiO2	62.06
Al2O3	21.59	21.82	21.35	21.57	21.37	21.89	21.41	21.47	21.45	21.67	Al2O3	24.70
TiO2	0.14	0.11	0.07	0.00	0.00	0.13	0.05	0.08	0.18	0.04	FeO	0.00
FeO	18.89	19.40	19.51	19.30	19.36	19.04	19.33	19.81	20.10	19.58	CaO	5.36
MnO	5.96	5.28	7.23	7.15	6.83	6.26	5.89	7.12	7.04	7.04	Na2O	8.03
MgO	1.43	1.40	1.42	1.50	1.52	1.42	1.37	1.53	1.52	1.51	K2O	0.10
CaO	13.85	14.03	12.24	12.00	12.40	13.79	13.58	12.17	12.29	12.27		
											Total	100.25
Total	100.70	101.09	100.24	100.24	100.40	101.55	100.14	101.20	101.38	100.91		

Sample	91-84	91-84	91-84	91-84	Sample	91-84	91-84	91-84	91-84	91-84	91-84	91-84
Phase	Pl	Pl	Pl	Pl	Phase	Hbl	Hbl	Hbl	Hbl	Hbl	Hbl	Hbl
Phase Pt.	Pl-A-2	Pl-A-4	Pl-C-6	Pl-C-7	Phase Pt.	Hbl-A-1	Hbl-A-2	Hbl-A-3	Hbl-A-4	Hbl-B-2	Hbl-B-3	Hbl-B-4
Location	Geo. Center	Rim	Rim	Rim	Location	Interior	Interior	Rim	Rim	Interior	Rim	Rim
SiO2	63.00	63.31	61.97	61.66	SiO2	43.01	42.92	41.70	41.22	42.44	42.82	42.96
Al2O3	25.38	25.07	24.62	25.03	Al2O3	10.72	11.16	12.48	13.11	11.39	11.40	11.49
FeO	0.00	0.00	0.00	0.00	TiO2	0.80	0.80	0.66	0.68	0.78	0.79	0.81
CaO	5.48	5.36	5.01	5.45	FeO	19.66	20.36	20.92	21.10	20.67	20.46	20.18
Na2O	8.10	8.11	7.74	7.32	MnO	0.62	0.60	0.59	0.59	0.56	0.56	0.57
K2O	0.09	0.09	0.07	0.05	MgO	8.54	8.74	7.77	7.44	8.54	8.71	8.52
					CaO	11.11	11.21	11.14	11.29	11.33	11.51	11.25
Total	102.05	101.95	99.41	99.80	Na2O	1.89	1.57	1.46	2.03	1.33	1.63	1.84
					K2O	0.32	0.28	0.43	0.46	0.33	0.32	0.35
					Total	96.67	97.63	97.15	97.92	97.38	98.20	97.97

Sample	91-84	91-84	91-84	91-84	91-84	91-84	91-84
Phase	CPX	CPX	CPX	CPX	CPX	CPX	CPX
Phase Pt.	CPX-A-1	CPX-A-2	CPX-A-3	CPX-A-4	CPX-A-5	CPX-A-6	CPX-B-1
Location	Core	Core	Core	Rim	Rim	Rim	Rim
SiO2	49.40	49.65	50.20	51.45	51.13	51.53	51.68
Al2O3	1.76	1.76	1.81	1.81	1.77	1.73	1.91
Cr2O3	0.07	0.00	0.00	0.00	0.00	0.00	0.00
TiO2	0.07	0.15	0.14	0.12	0.14	0.13	0.15
MnO	0.94	0.91	0.92	0.92	0.88	0.89	0.92
FeO	15.76	15.33	15.50	14.20	14.11	13.58	14.30
MgO	9.27	8.95	8.99	10.05	10.04	10.15	9.77
CaO	21.36	21.07	21.40	21.01	21.15	21.17	20.67
Na2O	0.41	0.56	0.37	0.91	0.61	0.88	0.40
Total	99.03	98.39	99.35	100.47	99.82	100.07	99.80

Analysis from Sample 92-5D

Sample	92-5D	92-5D	92-5D	92-5D	92-5D	92-5D	92-5D	92-5D	92-5D	92-5D	92-5D	92-5D
Phase	PL	PI	PI	PI	PI	PI	PI	PI	PI	PI	PI	PI
Phase Pt.	PI-A-1	PI-A-2	PI-A-3	PI-A-4	PI-A-5	PI-A-6	PI-A-7	PI-A-8	PI-B-1	PI-B-2	PI-B-3	PI-B-5
Location	Rim	Rim	Rim	Rim5um	from Rim	Center	Center	Center	Rim	Rim	Rim	Center
SiO2	61.64	61.87	62.31	63.28	62.89	62.83	61.98	62.49	61.82	61.43	60.65	61.49
Al2O3	23.76	23.75	24.30	24.16	24.25	24.69	24.67	24.41	24.27	24.26	23.90	23.72
CaO	4.26	4.46	4.61	4.48	4.63	4.67	4.70	4.64	4.89	4.81	4.77	4.75
Na2O	8.25	8.05	8.14	8.05	8.15	8.41	8.36	8.23	8.34	8.32	8.15	8.30
K2O	0.23	0.03	0.05	0.02	0.07	0.01	0.04	0.10	0.00	0.00	0.03	0.07
Total	98.13	98.16	99.42	99.98	99.99	100.61	99.75	99.93	99.31	98.82	97.50	98.33

Sample	92-5D	92-5D	92-5D	92-5D	92-5D	92-5D
Phase	PI	PI	PI	PI	PI	PI
Phase Pt.	PI-C-1	PI-C-2	PI-C-3	PI-C-4	PI-C-5	PI-C-6
Location	Rim	Rim	10um Rim	Center	Center	Center
SiO2	61.89	62.96	62.75	62.02	62.50	62.15
Al2O3	24.69	23.81	24.46	24.94	24.63	24.52
CaO	4.91	4.47	4.77	4.87	4.95	4.85
Na2O	8.14	8.05	8.19	8.08	8.08	8.21
K2O	0.00	0.09	0.04	0.12	0.16	0.15
Total	99.64	99.39	100.21	100.02	100.32	99.87

Sample	92-5D	92-5D	92-5D	92-5D	92-5D
Phase	Ilm	Ilm	Ilm	Ilm	Ilm
Phase Pt.	Ilm-A-1	Ilm-A-3	Ilm-A-4	Ilm-A-5	Ilm-A-6
Location	Center	Center	Rim	Rim	Rim
SiO2	0.56	1.46	1.16	1.35	0.85
Al2O3	0.16	0.07	0.10	0.11	0.08
TiO2	50.01	50.36	50.49	50.44	50.31
MnO	0.78	0.81	0.84	0.81	0.81
MgO	0.16	0.09	0.06	0.04	0.09
FeO	46.32	46.40	45.60	45.26	46.73
CaO	0.03	0.00	0.03	0.00	0.05
Cr2O3	0.10	0.22	0.24	0.24	0.30
Total	98.12	99.41	98.53	98.25	99.23

Sample	92-5D	92-5D	92-5D	Sample	92-5D	92-5D	92-5D	92-5D	92-5D	Sample	92-5D	92-5D
Phase	Ilm	Ilm	Ilm	Phase	Rt	Rt	Rt	Rt	Rt	Phase	Grt	Grt
Phase Pt.	Ilm-C-1	Ilm-C-2	Ilm-C-3	Phase Pt.	Rt-1-1	Rt-1-2	Rt-2-2	Rt-3-1	Rt-4-1	Phase Pt.	Grt-A-1	Grt-A-1b
Location	Center	Center	Center	Location	Matrix	Matrix	At Grt edge	Rt in Grt	Rt in Ky	Location	Rim	Rim
SiO2	1.01	1.51	1.01	SiO2	0.00	0.00	0.00	0.00	0.48	SiO2	36.73	37.29
Al2O3	0.09	0.09	0.13	Al2O3	0.04	0.02	0.00	0.06	0.02	Al2O3	21.74	22.11
TiO2	49.70	50.05	49.68	TiO2	96.07	98.00	97.54	96.38	98.26	TiO2	0.08	0.08
MnO	0.76	0.76	0.73	MnO	0.00	0.01	0.05	0.01	0.00	MnO	1.84	1.76
MgO	0.07	0.00	0.00	MgO	0.00	0.00	0.00	0.01	0.02	CaO	1.63	1.61
FeO	46.66	46.50	45.13	FeO	0.87	0.99	0.71	1.54	0.68	FeO	31.92	32.43
CaO	0.00	0.00	0.02	CaO	0.04	0.00	0.00	0.00	0.00	MgO	4.49	4.40
Cr2O3	0.28	0.31	0.27	Cr2O3	0.04	0.04	0.19	0.18	0.05			
										Total	98.13	99.66
Total	98.58	99.23	96.97	Total	97.07	99.10	98.50	98.17	99.50			

Sample	92-5D	92-5D	92-5D	92-5D	92-5D	92-5D	92-5D	92-5D	92-5D	92-5D	92-5D	92-5D
Phase	Grt	Grt	Grt	Grt	Grt	Grt	Grt	Grt	Grt	Grt	Grt	Grt
Phase Pt.	Grt-A-1c	Grt-A-2	Grt-A-3	Grt-A-4	Grt-A-5	Grt-A-6	Grt-A-7	Grt-A-8	Grt-A-9	Grt-A-10	Grt-A-11	Grt-A-12
Location	Rim	10um Rim	20um Rim	40um Rim	50um Rim	60um Rim	70um Rim	80um Rim	110um Rim	120um Rim	130um Rim	140um Rim
SiO2	36.96	37.24	36.75	36.37	36.42	37.25	35.90	36.29	36.17	37.52	36.23	36.96
Al2O3	21.63	22.53	21.57	22.63	22.00	22.12	21.36	21.98	21.15	22.04	21.19	21.92
TiO2	0.15	0.00	0.00	0.00	0.01	0.00	0.00	0.13	0.08	0.00	0.30	0.00
MnO	1.70	1.77	1.70	1.78	1.69	1.66	1.74	1.80	1.84	1.82	1.77	1.80
CaO	1.65	1.69	1.71	1.64	1.65	1.72	1.73	1.61	1.80	1.77	1.75	1.73
FeO	33.13	32.67	32.07	33.19	33.10	32.13	32.36	32.10	32.93	31.87	32.22	32.59
MgO	4.36	4.84	4.85	5.08	5.18	4.60	5.02	5.03	4.83	5.05	4.92	5.01
Total	99.58	100.43	98.64	100.70	100.05	99.48	98.11	98.94	98.79	100.06	98.38	100.00

Sample	92-5D	92-5D	92-5D	92-5D	92-5D	92-5D	92-5D	92-5D	92-5D	92-5D	92-5D	92-5D
Phase	Grt	Grt	Grt	Grt	Grt	Grt	Grt	Grt	Grt	Grt	Grt	Grt
Phase Pt.	Grt-A-13	Grt-A-14	Grt-A-16	Grt-A-17	Grt-A-18	Grt-A-19	Grt-A-20	Grt-A-21	Grt-A-22	Grt-A-23	Grt-A-24	Grt-A-25
Location	150um Rim	160um Rim	180um Rim	190um Rim	200um Rim	210um Rim	220um Rim	230um Rim	240um Rim-C	260um Rim-C	280um Rim	290um Rim
SiO2	36.31	36.52	36.33	35.73	37.09	36.67	37.05	35.87	36.92	36.57	38.73	36.32
Al2O3	21.22	21.97	21.22	21.32	21.44	21.03	21.37	21.10	21.60	21.19	21.93	21.16
TiO2	0.18	0.00	0.00	0.08	0.08	0.31	0.00	0.00	0.19	0.08	0.09	0.08
MnO	1.86	1.78	1.87	1.71	1.84	1.88	2.05	1.96	1.91	1.90	1.79	1.94
CaO	1.74	1.72	1.71	1.76	1.72	1.72	1.69	1.74	1.76	1.68	1.65	1.74
FeO	32.16	32.56	32.39	33.06	32.41	32.22	31.51	31.98	31.91	32.35	31.05	32.87
MgO	4.97	4.65	4.62	5.03	4.98	4.97	4.99	4.94	5.18	5.11	4.67	5.05
Total	98.45	99.20	98.13	98.68	99.57	98.81	98.66	97.59	99.46	98.87	99.90	99.16

Sample	92-5D	92-5D	92-5D	92-5D	92-5D	92-5D	92-5D	92-5D	92-5D	92-5D	92-5D	92-5D
Phase	Grt	Grt	Grt	Grt	Grt	Grt	Grt	Grt	Grt	Grt	Grt	Grt
Phase Pt.	Grt-A-26	Grt-A-27	Grt-A-28	Grt-A-29	Grt-A-30	Grt-A-31	Grt-A-32	Grt-A-33	Grt-A-34	Grt-B-4	Grt-B-5	Grt-B-6
Location	300um Rim	310um Rim	330um Rim	350um Rim	360um Rim	370um Rim	380um rim	390um Rim	400um Rim-R	Rim	Rim	Rim
SiO2	36.95	35.93	36.89	36.17	37.40	37.12	36.54	36.60	37.41	36.87	36.89	37.25
Al2O3	21.62	20.88	21.87	21.12	21.97	21.05	20.95	20.73	22.04	21.70	20.72	22.02
TiO2	0.00	0.39	0.00	0.15	0.15	0.08	0.00	0.15	0.14	0.15	0.07	0.22
MnO	1.87	1.89	1.89	1.79	1.86	1.90	1.96	1.84	2.09	1.54	1.46	1.53
CaO	1.73	1.68	1.76	1.66	1.61	1.68	1.71	1.55	1.50	1.58	1.50	1.58
FeO	31.85	31.41	32.01	32.50	31.58	32.04	31.95	32.14	33.08	34.21	34.12	33.65
MgO	4.93	5.11	5.15	5.37	5.12	5.25	5.09	5.20	4.41	3.86	4.33	4.15
Total	98.95	97.28	99.57	98.77	99.69	99.13	98.19	98.20	100.66	99.90	99.10	100.41

Sample	92-5D	92-5D	92-5D	92-5D	92-5D	92-5D	92-5D	92-5D	92-5D	92-5D	92-5D	92-5D
Phase	Grt	Grt	Grt	Grt	Grt	Grt	Grt	Grt	Grt	Grt	Grt	Grt
Phase Pt.	Grt-B-7	Grt-B-8	Grt-B-9	Grt-C-1b	Grt-C-2b	Grt-C-2	Grt-C-3	Grt-C-4	Grt-C-5	Grt-C-6	Grt-C-7	Grt-C-9
Location	Center	Center	Center	Rim	10um Rim	Center	Center	Rim	30um Rim	60um Rim	100um Rim	200um Rim
SiO2	37.03	37.23	36.71	37.07	36.60	37.48	37.05	37.21	36.02	37.03	37.15	36.44
Al2O3	21.08	21.91	21.58	21.98	22.02	21.23	21.72	20.91	21.73	21.00	21.69	21.71
TiO2	0.00	0.15	0.00	0.14	0.00	0.05	0.00	0.00	0.07	0.00	0.00	0.00
MnO	1.79	1.85	1.89	1.35	1.22	1.85	1.65	1.51	1.34	1.45	1.40	1.57
CaO	1.63	1.74	1.85	1.58	1.54	1.84	1.81	1.50	1.50	1.47	1.43	1.42
FeO	32.65	32.08	31.75	33.85	33.49	32.20	32.14	33.70	33.73	33.33	33.52	33.14
MgO	5.26	5.16	5.01	4.28	1.41	5.16	5.01	4.26	4.53	4.87	4.80	5.13
Total	99.45	100.13	98.79	100.27	99.27	99.84	99.39	99.09	98.97	99.14	100.00	99.41

Sample	92-5D	92-5D	Sample	92-5D	92-5D	92-5D	92-5D	92-5D	92-5D	92-5D	92-5D	92-5D
Phase	Grt	Grt	Phase	St	St	St	St	St	St	St	St	St
Phase Pt.	Grt-C-10	Grt-C-13	Phase Pt.	St-A-1	St-A-2	St-A-3	St-A-4	St-B2-1	St-B2-2	St-B2-3	St-B2-4	St-B2-5
Location	250um Rim	Rim	Location	Bleb-C	Bleb-C	Bleb-C	Bleb-R	Center	100um Center	200um Center	400um Center	500um Center
SiO2	36.40	36.81	ZnO	0.50	0.54	0.50	0.55	0.41	0.38	0.31	0.39	0.38
Al2O3	20.81	21.45	SiO2	28.28	28.37	28.33	28.09	28.31	28.12	27.99	27.97	27.94
TiO2	0.11	0.06	Al2O3	56.92	55.31	56.12	57.03	55.87	55.65	55.54	55.98	55.68
MnO	1.61	1.77	TiO2	0.81	0.85	0.77	0.79	0.78	0.75	0.76	0.74	0.77
CaO	1.41	1.86	MnO	0.08	0.10	0.07	0.05	0.08	0.06	0.09	0.12	0.04
FeO	33.27	32.57	FeO	12.67	12.59	12.77	12.60	13.43	13.58	13.39	13.36	13.49
MgO	5.17	5.00	MgO	1.71	1.74	1.61	1.53	1.94	1.98	2.06	1.97	1.93
Total	98.79	99.51	Total	100.96	99.49	100.17	100.64	100.81	100.52	100.14	100.52	100.23

Sample	92-5D	92-5D	92-5D
Phase	St	St	St
Phase Pt.	St-B2-6	St-B2-7	St-B2-8
Location	600um Center	800um Center	Rim
ZnO	0.32	0.26	0.50
SiO2	28.10	27.67	28.13
Al2O3	55.83	56.36	56.86
TiO2	0.77	0.80	0.89
MnO	0.06	0.11	0.09
FeO	13.76	13.62	13.18
MgO	1.55	1.42	1.33
Total	100.38	100.25	100.98

Sample	92-5D	92-5D	92-5D	92-5D	92-5D	92-5D	92-5D	92-5D	92-5D
Phase	Bt	Bt	Bt	Bt	Bt	Bt	Bt	Bt	Bt
Phase Pt.	Bt-A-1	Bt-A-1	Bt-A-1	Bt-A-1	Bt-A-1	Bt-A-1	Bt-B-1	Bt-B-1	Bt-B-1
Location	Center	Center	Center	Edge	Edge	Edge	Center	Center	Center
SiO2	35.72	34.64	36.60	36.68	36.65	36.23	35.76	36.62	36.78
Al2O3	19.55	20.20	20.12	19.94	20.26	20.67	19.98	20.26	20.26
TiO2	2.80	2.33	2.74	2.45	2.80	2.57	2.64	2.54	2.60
FeO	17.72	17.63	17.03	18.02	17.67	17.15	18.31	18.46	17.62
MnO	0.03	0.00	0.03	0.01	0.03	0.08	0.04	0.03	0.00
MgO	11.72	12.23	11.65	11.51	11.45	11.19	12.44	12.38	12.00
Cao	0.00	0.00	0.00	0.00	0.00	0.00	0.00	0.28	0.30
Na2O	0.25	0.19	0.18	0.33	0.29	0.30	0.21	0.28	0.51
K2O	8.83	9.13	9.18	8.64	7.99	8.87	8.79	8.80	8.68
Total	96.62	96.36	97.85	97.59	97.15	97.06	98.17	99.64	98.76

Sample	92-5D	92-5D	92-5D
Phase	Bt	Bt	Bt
Phase Pt.	Bt-B-1	Bt-B-2	Bt-B-2
Location	Center	Edge	Edge
SiO2	36.78	36.82	36.33
Al2O3	20.26	20.19	20.55
TiO2	2.60	2.57	2.49
FeO	17.62	17.51	17.73
MnO	0.00	0.06	0.02
MgO	12.00	11.69	11.82
Cao	0.30	0.00	0.74
Na2O	0.51	0.36	0.50
K2O	8.68	9.16	8.72
Total	98.76	98.36	98.90

Analysis from Sample 92-87

Sample	92-87	92-87	92-87	92-87	92-87	92-87	92-87	92-87	92-87	92-87	92-87	92-87
Phase	Pl	Pl	Pl	Pl	Pl	Pl	Pl	Pl	Pl	Pl	Pl	Pl
Phase Pt.	Pl-A-1	Pl-A-2	Pl-A-4	Pl-B-1	Pl-B-2	Pl-B-4	Pl-B-5	Pl-C-1	Pl-C-2	Pl-C-3	Pl-C-4	Pl-C-5
Location	Inc. in Grt	Inc. in Grt	Inc. in Grt-E	Center	Center	Edge	Edge	Center	Center	Center	Edge	Edge
FeO	0.00	0.02	0.40	0.05	0.05	0.34	0.27	0.03	0.06	0.04	0.05	0.05
SiO2	58.30	58.94	57.93	57.65	57.99	58.48	58.68	57.98	58.66	58.38	58.58	57.54
Al2O3	27.25	26.23	27.70	27.37	27.44	27.41	27.13	26.50	26.85	26.90	27.09	27.31
CaO	7.88	6.54	7.91	7.92	8.01	7.66	6.70	7.97	7.37	7.83	7.98	7.89
Na2O	6.43	6.68	6.39	6.23	6.33	6.45	6.65	6.51	6.74	6.71	6.60	6.52
K2O	0.13	0.33	0.06	0.06	0.06	0.06	0.47	0.08	0.07	0.09	0.06	0.04
Total	99.99	98.75	100.42	99.28	99.88	100.40	99.89	99.06	99.76	99.94	100.35	99.36

Sample	92-87	92-87	92-87	Sample	92-87	92-87	92-87	92-87	92-87	92-87	92-87	92-87
Phase	Pl	Pl	Pl	Phase	Grt	Grt	Grt	Grt	Grt	Grt	Grt	Grt
Phase Pt.	Pl-C-6	Pl-D-1	Pl-D-2	Phase Pt.	Grt-A-1	Grt-A-2	Grt-A-3	Grt-A-4	Grt-A-5	Grt-A-6	Grt-A-7	Grt-A-8
Location	Edge	Edge	Center	Location	Rim	Rim	Rim	10um rim	25um Rim	40um Rim	80um Rim	100um Rim
FeO	0.00	0.06	0.04	SiO2	35.25	36.91	36.70	37.56	37.85	37.94	37.60	37.84
SiO2	58.24	58.38	57.79	Al2O3	20.84	22.05	21.06	21.59	21.76	22.39	22.51	22.11
Al2O3	27.20	26.95	26.79	TiO2	0.40	0.00	0.26	0.12	0.23	0.00	0.03	0.23
CaO	7.97	7.56	7.71	MnO	3.56	3.51	3.54	3.26	3.18	3.09	3.01	2.67
Na2O	6.47	6.30	6.16	CaO	4.68	4.78	4.99	4.88	4.90	4.96	5.04	5.17
K2O	0.00	0.06	0.06	FeO	29.72	30.01	29.86	28.94	29.60	29.06	29.39	29.92
				MgO	2.86	3.15	3.41	3.61	3.74	3.89	4.09	4.15
Total	99.89	99.29	98.56	Total	97.32	100.42	99.82	99.96	101.26	101.33	101.67	102.10

Sample	92-87	92-87	92-87	92-87	92-87	92-87	92-87	92-87	92-87	92-87	92-87	92-87
Phase	Grt	Grt	Grt	Grt	Grt	Grt	Grt	Grt	Grt	Grt	Grt	Grt
Phase Pt.	Grt-A-9	Grt-A-10	Grt-A-11	Grt-A-12	Grt-A-13	Grt-A-14	Grt-A-15	Grt-A-16	Grt-A-17	Grt-A-18	Grt-A-19	Grt-A-20
Location	135um Rim	170um Rim	225um Rim	450um Rim	500um Rim	550um Rim	650um Rim	750um Rim	850um Rim	950um Rim	1050um Rim	1150um Rim
SiO2	37.66	37.56	38.77	37.66	37.11	37.80	38.10	38.02	38.26	38.13	38.05	37.14
Al2O3	22.23	22.37	2.22	22.68	22.41	22.69	22.07	22.77	22.45	22.18	22.26	22.52
TiO2	0.23	0.00	0.00	0.15	0.00	0.00	0.30	0.59	0.00	0.22	0.45	0.39
MnO	2.70	2.83	2.78	2.82	3.06	2.97	2.99	3.07	3.04	3.08	3.10	3.32
CaO	5.09	5.09	5.01	5.05	4.88	5.05	5.37	5.01	4.94	4.89	4.48	4.85
FeO	29.46	29.36	28.90	28.70	29.39	29.74	28.82	28.69	28.73	27.73	29.04	29.20
MgO	4.25	4.26	4.23	4.37	4.37	4.46	4.30	4.28	4.40	4.42	4.42	4.45
Total	101.62	101.48	101.90	101.44	101.22	102.72	101.97	102.43	101.85	100.64	101.80	101.87

Sample	92-87	92-87	92-87	92-87	92-87	92-87	92-87	92-87	92-87	92-87	92-87	92-87
Phase	Grt	Grt	Grt	Grt	Grt	Grt	Grt	Grt	Grt	Grt	Grt	Grt
Phase Pt.	Grt-A-21	Grt-A-22	Grt-A-23	Grt-A-24	Grt-A-25	Grt-A-26	Grt-A-28	Grt-A-29	Grt-A-30	Grt-A-31	Grt-A-32	Grt-A-33
Location	1250um Rim	1350um Rim	1450um Rim	1550um Rim	1650um Rim	1750um Rim	2000um Rim	2100um Rim	2200um Rim	2300um Rim	2400um Rim	2500um Rim
SiO2	37.90	37.90	38.40	38.20	38.03	38.09	37.61	38.41	37.60	38.07	37.57	37.75
Al2O3	22.43	22.10	22.25	22.44	22.80	22.23	22.58	22.28	22.02	22.43	22.57	22.68
TiO2	0.11	0.00	0.00	0.05	0.00	0.16	0.16	0.14	0.11	0.00	0.38	0.29
MnO	3.19	3.30	3.44	3.42	3.34	3.43	3.55	3.52	3.69	3.69	3.72	3.96
CaO	4.94	4.94	4.90	5.01	4.95	5.04	4.93	4.97	4.88	4.81	5.08	5.29
FeO	28.72	28.80	28.05	28.31	22.76	28.52	28.44	28.47	27.89	28.36	28.04	28.31
MgO	4.48	4.46	4.50	4.53	4.45	4.49	4.49	4.47	4.45	4.43	4.46	4.32
Total	101.77	101.49	101.54	101.96	102.32	101.97	101.76	102.27	100.63	101.79	101.82	102.60

Sample	92-87	92-87	92-87	92-87	92-87	92-87	92-87	92-87	92-87	92-87	92-87
Phase	Grt	Grt	Grt	Grt	Grt	Grt	Grt	Grt	Grt	Grt	Grt
Phase Pt.	Grt-A-34	Grt-A-35	Grt-A-36	Grt-A-37	Grt-A-38	Grt-A-39	Grt-A-40	Grt-A-41	Grt-A-42	Grt-A-43	Grt-A-45
Location	2600um Rim	2700um Rim	2850um Rim	2950um Rim	3050um Rim	3150um Rim	3250um Rim	3400um Rim	3600um Rim	3800um Rim	Rim
SiO2	37.24	37.95	37.46	38.29	37.69	37.75	37.56	37.69	37.89	38.10	37.05
Al2O3	22.00	22.23	21.76	22.69	22.18	22.17	21.82	22.15	21.92	21.86	22.39
TiO2	0.12	0.35	0.53	0.39	0.35	0.43	0.14	0.12	0.43	0.23	0.00
MnO	3.86	3.73	3.80	3.65	3.81	4.03	3.99	3.84	3.85	3.84	3.00
CaO	4.47	4.70	4.81	5.02	4.82	4.74	5.13	5.13	5.25	5.11	5.08
FeO	28.10	27.89	27.67	28.03	28.12	28.34	28.06	28.34	28.24	27.55	28.78
MgO	4.45	4.41	4.40	4.33	4.47	4.45	4.39	4.41	4.37	4.35	4.06
Total	100.23	101.26	100.44	102.39	101.44	101.92	101.09	101.66	101.96	101.04	100.36

Sample	92-87	92-87	92-87	92-87	92-87	92-87	92-87	92-87	92-87	92-87	92-87	92-87
Phase	Hbl	Hbl	Hbl	Hbl	Hbl	Hbl	Hbl	Hbl	Hbl	Hbl	Hbl	Hbl
Phase Pt.	Hbl-A-1	Hbl-A-2	Hbl-A-4	Hbl-A-5	Hbl-A-6	Hbl-B-1	Hbl-B-2	Hbl-B-3	Hbl-B-5	Hbl-C-1	Hbl-C-3	Hbl-C-4
Location	Center	Center	Rim	Rim	Rim	Center	Center	Edge	Edge	Center	Center	Edge
SiO2	41.60	41.43	41.40	41.71	41.51	41.49	41.49	41.71	41.54	41.23	41.17	41.79
TiO2	0.55	0.53	0.58	0.55	0.45	0.58	0.47	0.45	0.41	0.51	0.51	0.52
Al2O3	16.38	16.17	16.84	16.87	16.70	16.21	16.15	16.70	16.58	16.51	16.45	16.79
FeO	17.42	17.39	17.09	17.21	17.38	17.25	17.60	17.07	17.18	17.69	17.37	17.40
MnO	0.23	0.25	0.18	0.24	0.23	0.23	0.27	0.22	0.21	0.22	0.23	0.19
MgO	8.31	8.36	7.97	7.94	8.00	8.49	8.46	8.25	8.21	8.41	8.24	8.16
CaO	10.97	11.23	11.00	11.13	10.98	11.01	10.83	11.04	10.99	10.77	11.08	11.00
Na2O	1.19	1.19	1.32	1.32	1.26	1.25	1.25	1.31	1.34	1.35	1.40	1.39
K2O	0.00	0.08	0.01	0.00	0.02	0.00	0.03	0.00	0.00	0.02	0.01	0.00
F	0.00	0.00	0.00	0.33	0.00	0.00	0.00	0.00	0.00	0.00	0.00	0.00
Cl	0.00	0.04	0.01	0.06	0.00	0.00	0.00	0.00	0.00	0.00	0.00	0.00
Total	96.65	96.67	96.39	97.35	96.54	96.49	96.55	96.74	96.45	96.77	96.46	97.24

92-87
Hbl
Hbl-C-5
Edge
41.34
0.48
16.60
17.42
0.24
8.19
10.87
1.35
0.07
0.00
0.00
96.57

Analysis from Sample 92-97

Sample	92-97	92-97	92-97	92-97	92-97	92-97	92-97	92-97	92-97	92-97	92-97	92-97
Phase	Grt	Grt	Grt	Grt	Grt	Grt	Grt	Grt	Grt	Grt	Grt	Grt
Phase Pt.	Grt-A-1	Grt-A-2	Grt-A-3	Grt-A-4	Grt-B-1	Grt-B-2	Grt-B-3	Grt-B-4	Grt-B-5	Grt-B-6	Grt-C-1	Grt-C-3
Location	Center	Rim	Rim	Rim	Center	Center	Center	Rim	Rim	Rim	Center	Rim
SiO2	38.84	38.34	38.11	37.69	38.34	38.42	38.39	38.24	38.31	38.21	38.31	38.47
Al2O3	22.51	22.49	22.49	22.51	22.82	22.70	22.55	22.31	22.33	22.53	22.24	22.45
TiO2	0.00	0.03	0.00	0.00	0.01	0.03	0.00	0.02	0.09	0.00	0.05	0.02
MnO	2.00	1.66	1.71	1.85	1.73	1.70	1.86	1.89	1.78	1.76	2.35	1.65
CaO	4.81	5.31	5.50	5.54	4.96	5.09	4.94	4.85	4.54	5.05	4.87	5.08
FeO	27.22	27.36	27.01	27.77	27.86	27.14	27.53	28.27	27.77	28.00	27.07	27.43
MgO	4.76	4.74	4.54	4.52	5.08	5.05	5.06	4.85	4.74	4.79	4.82	4.82
Total	100.13	99.93	99.36	99.88	100.79	100.14	100.34	100.43	99.56	100.34	99.71	99.92

Sample	92-97	Sample	92-97	92-97	92-97	92-97	92-97	92-97	92-97	Sample	92-97	92-97
Phase	Grt	Phase	Hbl	Hbl	Hbl	Grt	Hbl	Hbl	Hbl	Phase	Pl	Pl
Phase Pt.	Grt-C-4	Phase Pt.	Hbl-A-1	Hbl-A-2	Hbl-A-3	Hbl-A-4	Hbl-B-1	Hbl-B-4	Hbl-B-5	Phase Pt.	Pl-A-1	Pl-A-2
Location	Rim	Location	Interior	Interior	Rim	Rim	Interior	Rim	Rim	Location	Core	Core
SiO2	38.81	SiO2	42.41	41.78	42.13	41.85	40.63	42.57	42.44	SiO2	57.43	58.17
Al2O3	22.71	Al2O3	16.44	16.15	16.69	16.22	15.86	16.32	16.41	Al2O3	27.26	29.08
TiO2	0.02	TiO2	0.65	0.63	0.61	0.59	0.51	0.65	0.70	CaO	8.80	8.64
MnO	1.81	MnO	0.04	0.06	0.10	0.03	0.04	0.00	0.07	Na2O	5.86	6.00
CaO	5.10	MgO	9.83	9.68	9.59	9.60	8.69	9.38	9.46	K2O	0.09	0.03
FeO	27.81	FeO	16.72	16.48	16.59	16.82	16.53	16.33	16.58			
MgO	4.66	CaO	11.34	11.42	11.61	11.52	10.97	11.36	11.34	Total	99.45	100.92
		Na2O	1.63	1.20	1.32	1.19	1.28	1.36	1.23			
Total	100.92	K2O	0.54	0.54	0.51	0.52	0.52	0.51	0.55			
		Total	99.58	97.92	99.16	98.34	95.03	98.49	98.77			

Sample	92-97	92-97	92-97	92-97
Phase	Pl	Pl	Pl	Pl
Phase Pt.	Pl-A-3	Pl-A-4	Pl-B-1	Pl-B-4
Location	Rim	Rim	Center	Rim
SiO2	57.76	57.35	57.52	56.11
Al2O3	28.03	27.90	26.95	27.51
CaO	8.80	9.03	8.37	9.42
Na2O	5.98	5.79	6.05	5.44
K2O	0.02	0.03	0.07	0.04
Total	100.58	100.10	99.17	98.52

Appendix 6 $^{40}Ar/^{39}Ar$ Mineral Release Spectra

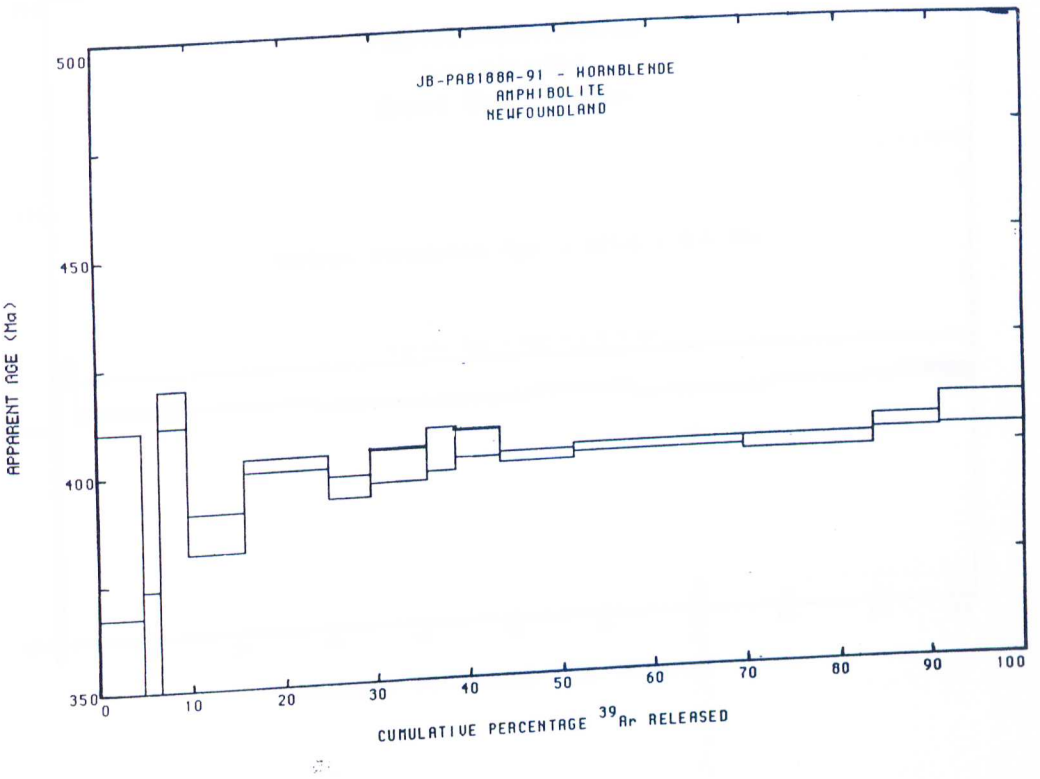

Figure 18a. $^{40}Ar/^{39}Ar$ spectra diagrams.

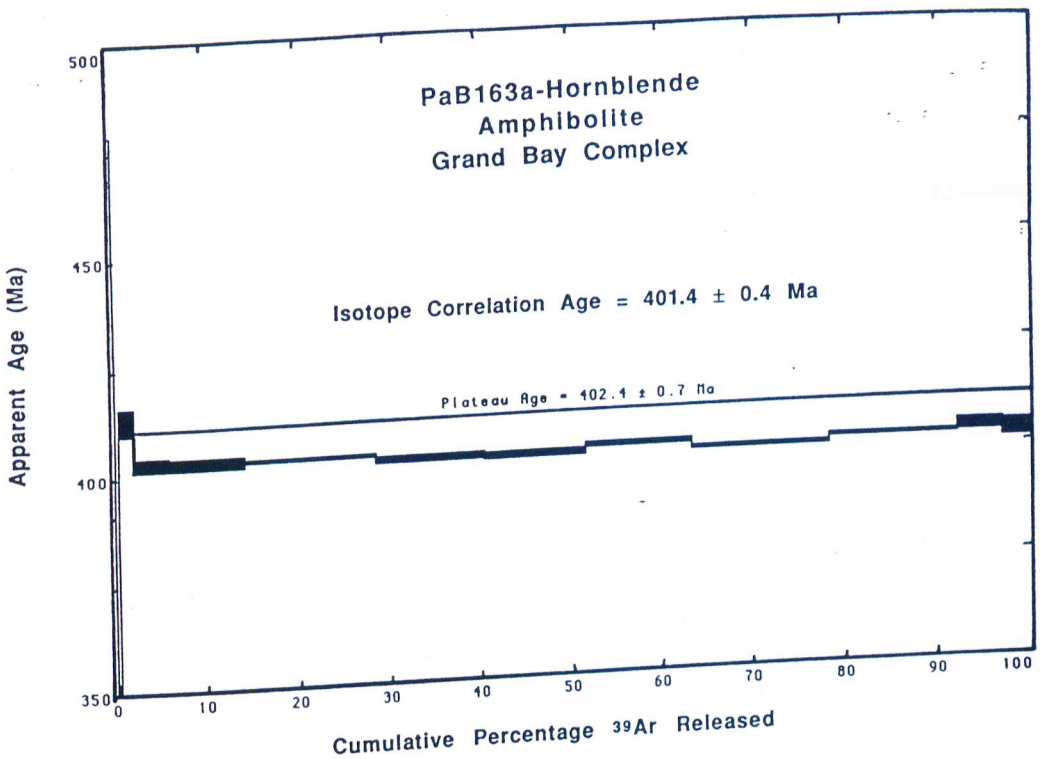

Figure 18b. $^{40}Ar/^{39}Ar$ spectra diagrams showing the apparent age, plateau age and isotope correlation age as a function of cumulative percentage of ^{39}Ar released.

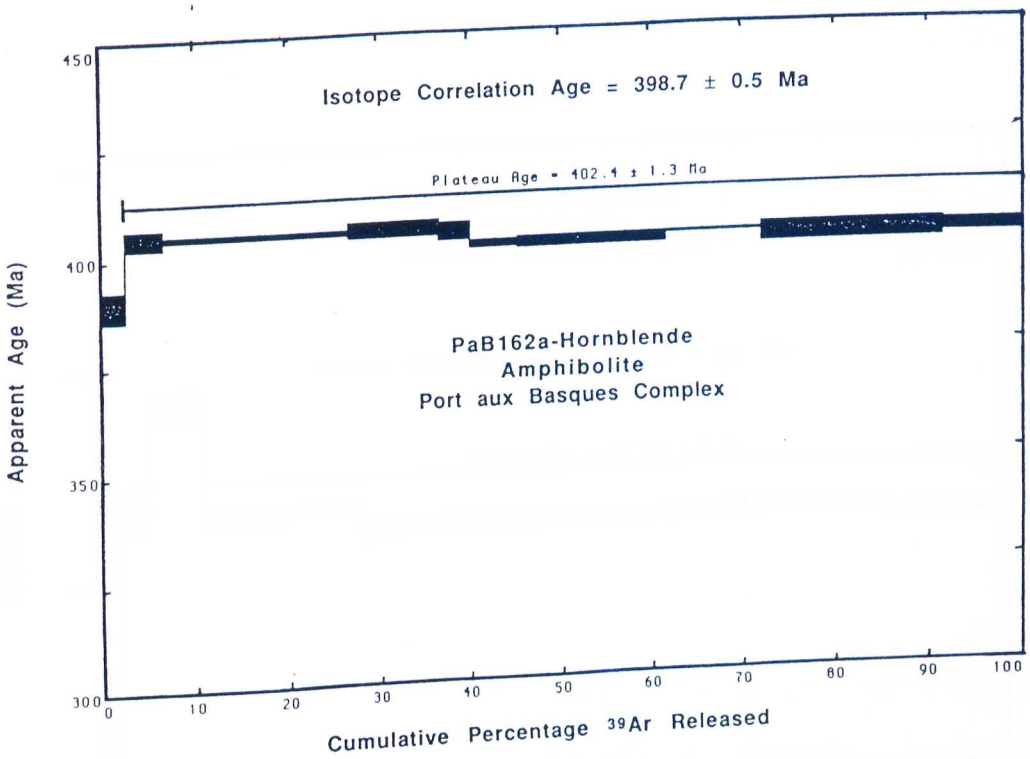

Figure 18c. $^{40}Ar/^{39}Ar$ spectra diagrams showing the apparent age, plateau age and isotope correlation age as a function of cumulative percentage of ^{39}Ar released.

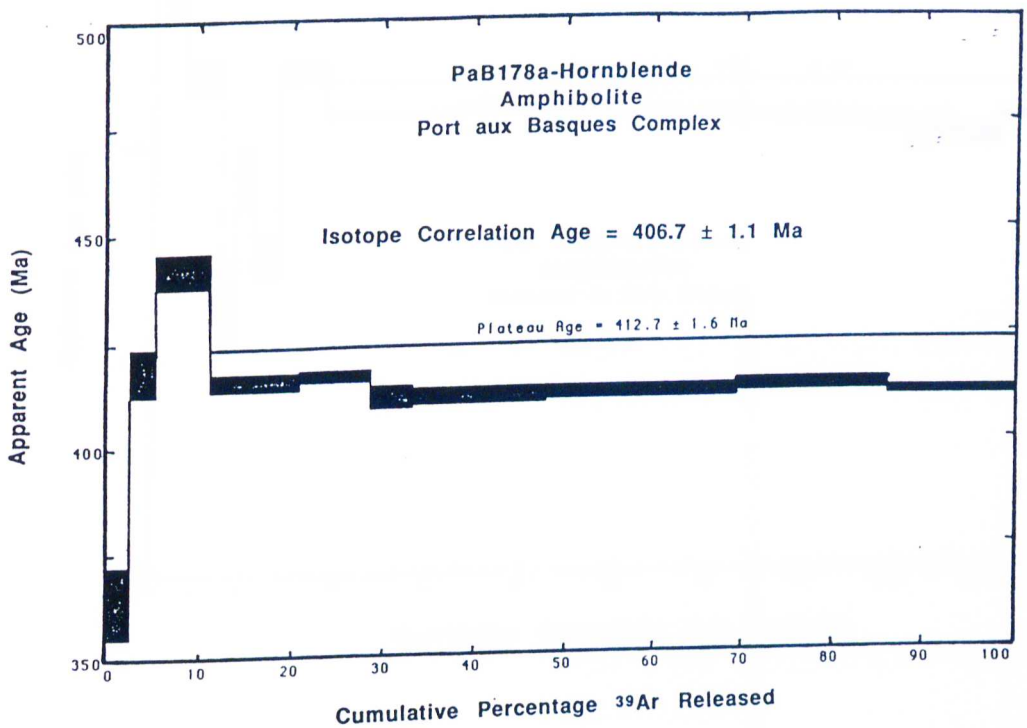

Figure 18d. $^{40}Ar/^{39}Ar$ spectra diagrams showing the apparent age, plateau age and isotope correlation age as a function of cumulative percentage of ^{39}Ar released.

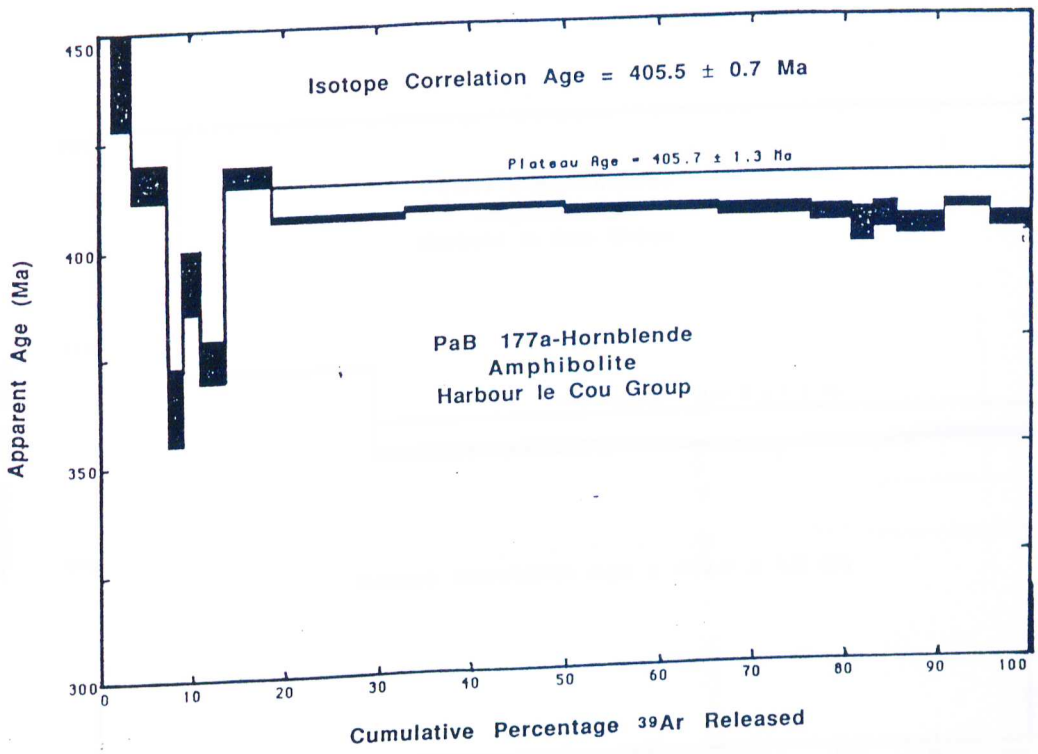

Figure 18e. $^{40}Ar/^{39}Ar$ spectra diagrams showing the apparent age, plateau age and isotope correlation age as a function of cumulative percentage of ^{39}Ar released.

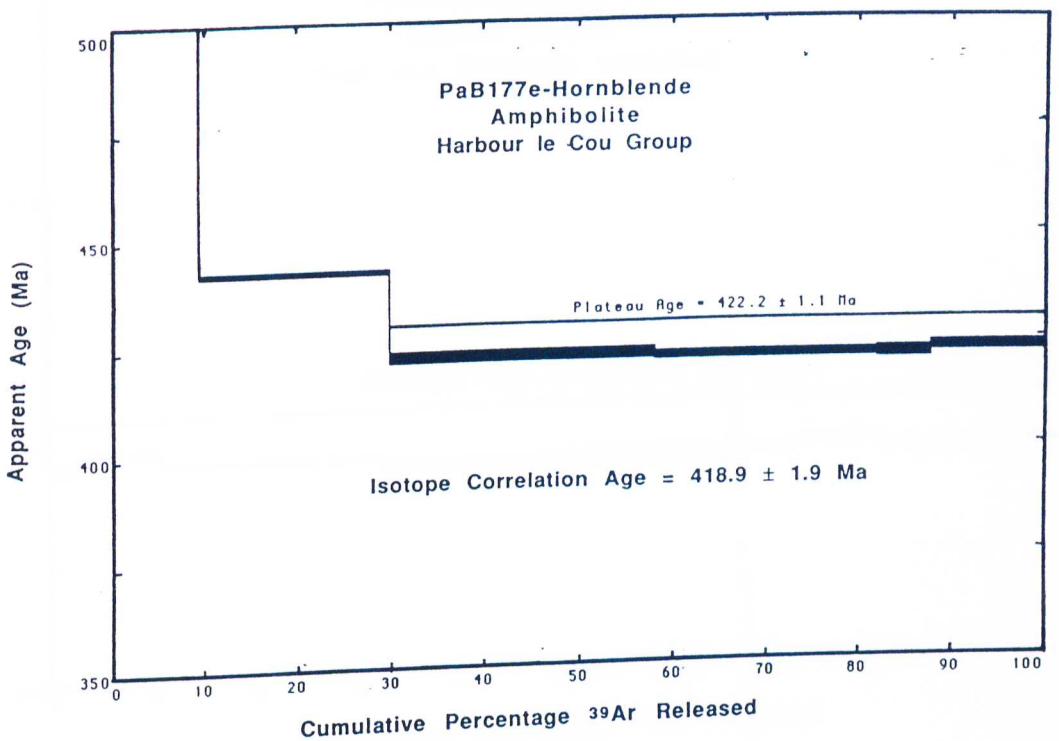

Figure 18f. $^{40}Ar/^{39}Ar$ spectra diagrams showing the apparent age, plateau age and isotope correlation age as a function of cumulative percentage of ^{39}Ar released.

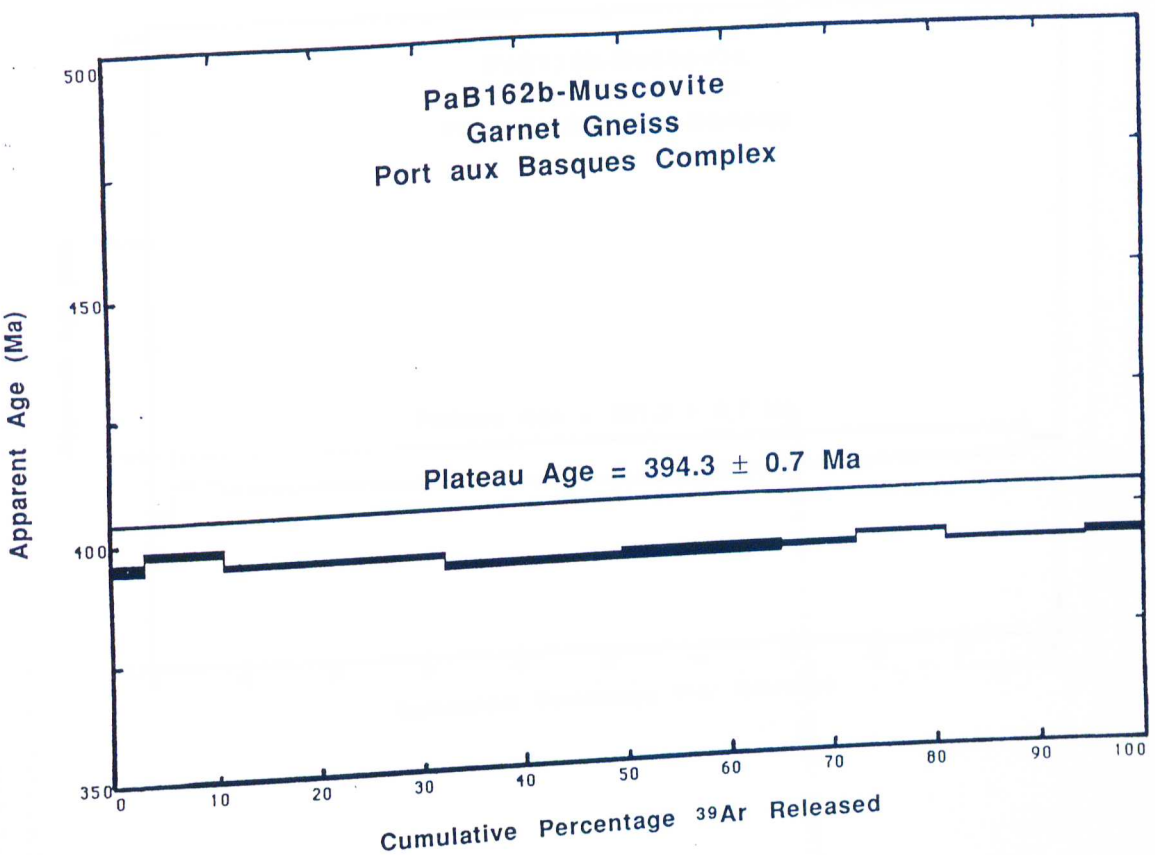

Figure 18g. $^{40}Ar/^{39}Ar$ spectra diagram showing the apparent age and plateau age as a function of cumulative percentage of ^{39}Ar released.

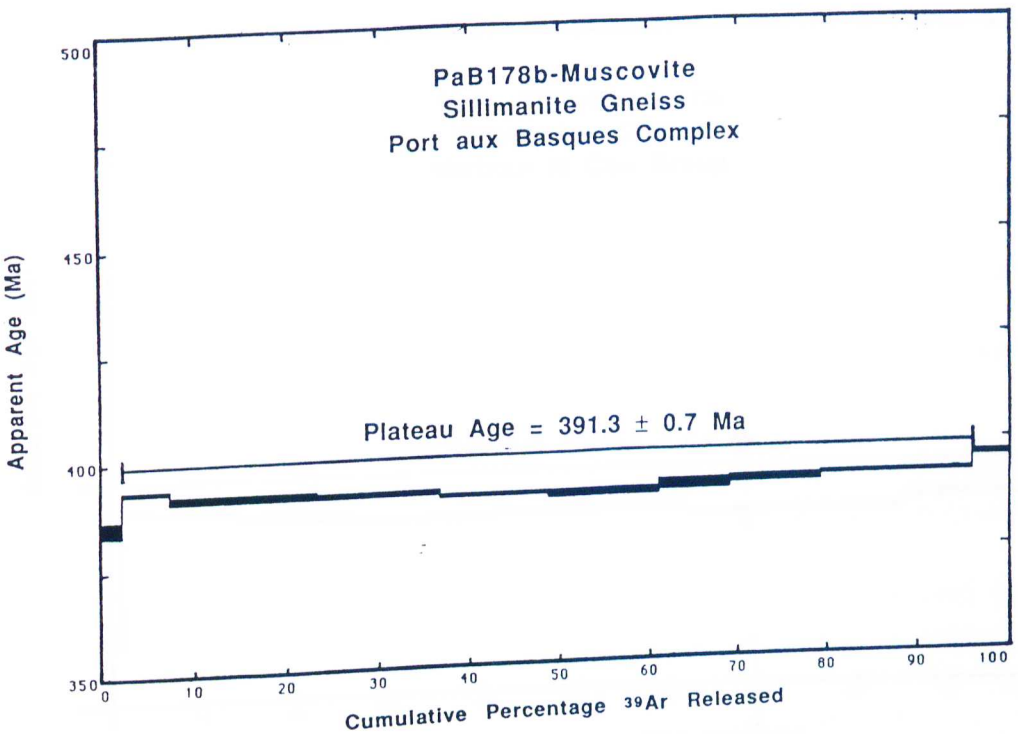

Figure 18h. $^{40}Ar/^{39}Ar$ spectra diagram showing the apparent age and plateau age as a function of cumulative percentage of ^{39}Ar released.

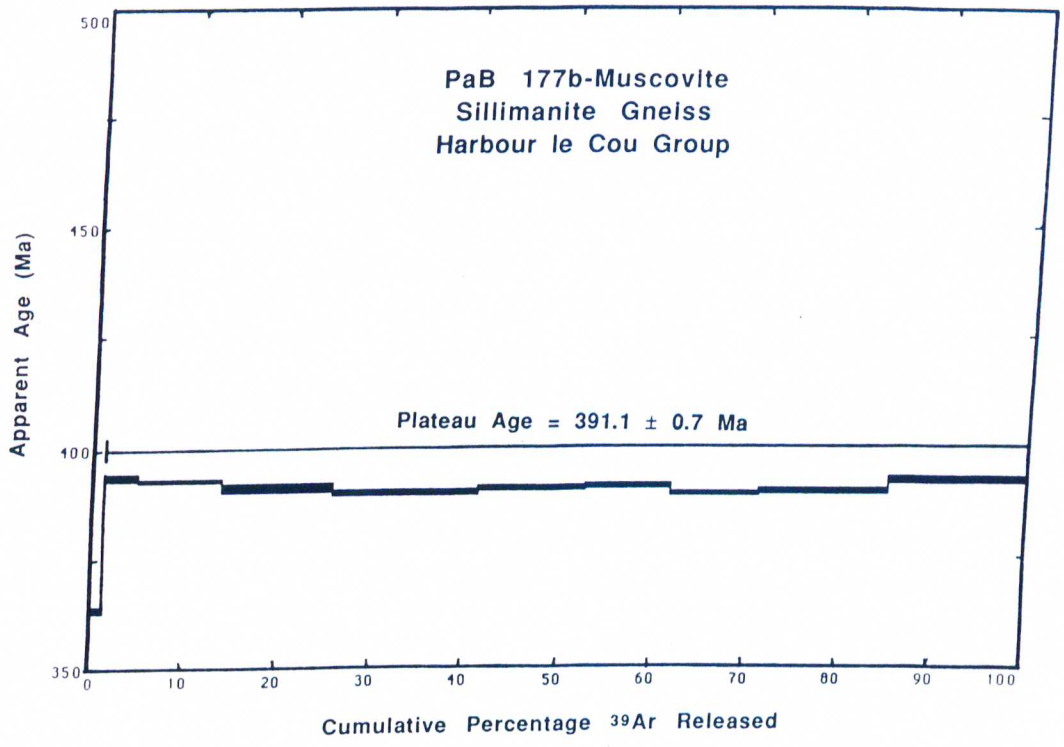

Figure i. $^{40}Ar/^{39}Ar$ spectra diagram showing the apparent age and plateau age as a function of cumulative percentage of ^{39}Ar released.

References

Barr, S.M., Jamieson, R.A., Raeside, R.P. and McMullen, D.W., 1992. The Newfoundland-Cape Breton Island connection; *in GAC/MAC joint annual meeting* abstracts 17, p6.

Barr, S.M. and Jamieson, R.A., 1991. Tectonic setting and regional correlation of Ordovician-Silurian rocks of the Aspy terrane, Cape Breton Island, Nova Scotia; *Canadian Journal of Earth Science*, 28, 1769-1779.

Barr, S.M. and Raeside R.P., 1989. Tectonostratigraphic terranes in Cape Breton Island, Nova Scotia; implications for the configuration of the Northern Appalachian orogen; *Geology*, 17, 822-825.

Bégin, N.L., 1992. Contrasting mineral isograd sequences in metabasites of the Cape Smith Belt, northern Québec, Canada: three new bathograds for mafic rocks. *Journal of Metamorphic Geology*, 10, 685-704.

Bell, T.H., 1985. Deformation partitioning and porphyroblast rotation in metamorphic rocks: a radical interpretation; *Journal of Metamorphic Geology*, 3, 109-118.

Bell, T.H., 1986. Foliation development and refraction in metamorphic rocks: reactivation of earlier foliations and decrenulation due to shifting patterns of deformation partitioning; *Journal of Metamorphic Geology*, 4, 421-444.

Bell, T.H. and Rubenach, M.J., 1983. Sequential porphyroblast growth and crenulation cleavage development during progressive deformation; *Tectonophysics*, 92, 171-194.

Bence, A.E. and Albee, A.L., 1968. Empirical correction factors for the microanalysis of silicates and oxides. *Journal of Geology*, 76, 382-403.

Bickle, M.J. and Archibald, N.J., 1984. Chloritoid and staurolite stability: implications for metamorphism in the Archaean Yilgarn Block, Western Austrilia. *Journal of Metamorphic Geology*, 2, 179-203.

Bohlen, S.R., Montana, A. L. and Kerrick, D.M., 1991. Precise determinations of the equilibria kyanite = sillimanite and kyanite = andalusite and a revised triple point for Al_2SiO_5 polymorphs. *American Mineralogist*, 76, 677-680.

Bohlen, S.R., Wall, V.J. and Boettcher, A.L., 1983a. Experimantal investigations and geological applications of equilibria in the system FeO-TiO_2-Al_2O_3-SiO_2-H_2O. *American Mineralogist*, 68, 1049-1058.

Bohlen, S.R., Wall, V.J. and Boettcher, A.L., 1983b. Experimental investigation and application of garnet granulite equilibria; *Contributions to Mineralogy and Petrology*, 83, 52-61.

Boucot, A.J., 1962. Appalachian Siluro-Devonian, *in* Coe, K., ed., Some aspects of the Variscan fold belt: 9th Inter-Univ. Geol. Cong., Manchester, UK, Manchester University Press, 155-163.

Brown, Michael, 1973. The definition of metatexis, diatexis and migmatite; *Proceedings of the Geologists' Association*; 84, 371-382.

Brown, Michael, 1993. P-T-t evolution of orogenic belts and the causes of regional metamorphism: *Journal of the Geological Society, London*, 150, 227-241.

Brown, P, A., 1973. The structural and metamorphic history of the Port aux Basques region, Newfoundland; M.Sc. thesis, Department of Geology, Memorial University of Newfoundland, St. John's, Newfoundland.

Brown, P, A., 1976. Geology of the Rose Blanche map area (110/10), Newfoundland *Department of Mines, Report* 76-5, 16 p.

Brown, P, A., 1977. Geology of the Port aux Basques map area (110/10): *Newfoundland Department of Mines Report* 77-2, 11p.

Burgess, J.L., Brown, M. and van Staal, C.R., 1992. Preliminary report on the metamorphic geology of the Port aux Basques Complex, southwestern Newfoundland; *in Current Research, Part D; Geological Survey of Canada, Paper* 92-1D, 145-154.

Burgess, J.L., Brown, M. and van Staal, C.R., 1993. Pressure-temperature conditions and a P-T path for the Port aux Basques area, southwest Newfoundland; *in Current Research, Part D; Geological Survey of Canada, Paper* 93-1D, 47-55.

Cameron, A.E., Smith, D.H. and Walker, R.L., 1967. Mass spectrometry of nanogram-sized samples of lead; *Analytical Chemistry*, 41, 525-526.

Carmichael, D.M., 1969. On the mechanism of prograde metamorphic reactions in quartz-bearing pelitic rocks; *Contributions to Mineralogy and Petrology,* 20, 244-267.

Carmichael, D.M., 1978. Metamorphic bathozones and bathograds: a measure of the depth of post-metamorphic uplift and erosion on the regional scale. *American Journal of Science,* 278, 769-797.

Carmichael, D.M., 1990. Metamorphism and geodynamics of the southwestern Grenville Province, Ontario, *in* IGCP Project 235-304, Field Trip 1 Guidebook, 27.

Cawood, P.A., Dunning, G.R., Lux, D. and van Gool, J.A.M., 1994. Timing of peak metamorphism and deformation along the Appalachina margin of Laurentia in Newfoundland: Silurian, not Ordovician. *Geology*, 22, 399-402.

Chorlton, L.B. and Dallmeyer, R.D., 1986. Geochronology of Early to middle Paleozoic tectonic development in the southwest Newfoundland Gander Zone; *Journal of Geology*, 94, 67-89.

Cliff, R.A. and Cohen, A., 1980. Uranium-lead isotope systematics in a regionally metamorphosed tonolite from the Eastern Alps, *Earth and Planetary Science Letters,* 50, 211-218.

Dallmeyer, R.D. and Gil-Ibarguchi, J.I., 1990. Age of amphibolitic metamorphism in the ophiolitic unit of the Morais allochthon (Portugal): Implications for early Hercynian orogenesis in the Iberian Massif; *Journal of the Geological Society of London,* 147, 873-878.

Dallmeyer, R.D. and Nance R.D, 1992. Tectonic implications of $^{40}Ar/^{39}Ar$ mineral ages from late Precambrian-Cambrian plutons, Avalon composite terrane, southern New Brunswick, Canada *Canadian Journal of Earth Science*, 29, 2445-2462.

Dallmeyer, R.D. and Keppie, 1993. $^{40}Ar/^{39}Ar$ mineral ages from the southern Cape Breton Highlands and Creignish Hills, Cape Breton Island, Nova Scotia, Canada; evidence for a polyphase tectonothermal evolution; *Journal of Geology*, 101, 467-482.

Dalrymple, G.B., Alexander, E.C., Lanphere, M.A. and Kraker, G.P., 1981. Irradiation of samples for $^{40}Ar/^{39}Ar$ dating using the Geological Survey TRIGA ractor; *U.S. Geological Survey, Professional Paper 1176*, 55 p.

Dodson, M.H., 1973. Closure temperatures in cooling geochronological and petrological systems; *Contributions to Mineralogy and Petrology,* 40, 259-274.

Dubé, B., Lauzière, K. and Tremblay, A., 1991. Observations on the structural control and tectonic setting of gold mineralization in the Cape Ray fault zone, southwestern Newfoundland; *in Current Research, Part D, Geological Survey of Canada, Paper 91-1D,* 135-145.

Dubé, B. and Lauzière, K., 1993. Along strike kinematics variation of the Cape Ray Fault in SW Newfoundland and its structural significance; Abstract, Northeast Section, *Geological Society of America* , p 123.

Dunning, G.R., O'Brian, S.J., Colman-Sadd, S.P., Blackwood, R.F., Dickson, W.L., O'Niel, P.P. and Krogh, T.E., 1990a. Silurian orogeny in the Newfoundland Appalachians. *Journal of Petrology,* 98, 895-913.

Dunning, G.R., Barr, S.M., Raeside, R.P. and Jamieson, R.A., 1990b. U-Pb zircon, titanite and monazite ages in the Bras d'Or and Aspy terranes of Cape Breton Island, Nova Scotia: implications for magmatic and metamorphic history: *Geological Society of America Bulletin,* 102, 322-330.

Ellis, D.J. and Green, E.H., 1979. An experimental study of the effect of Ca upon garnet-clinopyroxene Fe-Mg exchange equilibria. *Contributions to Mineralogy and Petrology,* 71, 13-22.

Ferry, J.M. and Spear, F.S., 1978. Experimental calibration of the partitioning of Fe and Mg between biotite and garnet. *Contributions to Mineralogy and Petrology,* 66, 113-117.

Graham, C.M. and Powell, R., 1984. A garnet-hornblende geothermometer: calibration, testing and application to the Pelona Schist, Southern California; *Journal of Metamorphic Geology,* 2, 13-21.

Greenough, J. D. and Krogh, T. E. and Kamo S. L., 1993. A Silurian U-Pb age for the Cape St. Mary's sills, Avalon Penisula, Newfoundland Canada: implications for Silurian orogenesis in the Avalon Zone; *Canadian Journal of Earth Science,* 30, 1607-1612.

Hall, L., van Staal, C.R., and Williams, H., 1994. Ordovician strucutral evolution of southwest Newfoundland; *in Geological Association of Canada/Mineralogical Association of Canada joint annual meeting* abstracts 19, p. 46.

Harrison, T.M., 1981. Diffusion of ^{40}Ar in hornblende; *Contributions to Mineralogy and Petrology,* 78, 324-331.

Hodges, K.V. and Crowley, D.H., 1985. Error estimation and empirical geothermobarometry for pelitic systems. *American Mineralogist*, 70, 702-709.

Hodges, K.V. and Spear, F.S., 1982. Geothermometry, geobarometry and the Al_2SiO_5 triple point at Mt. Moosilauke, New Hampshire; *American Mineralogist*, 67, 1118-1134.

Holdaway, M.J., Dutrow, B.L. and Hinton, R.W., 1988. Devonian and Carboniferous metamorphism in west-central Maine: The muscovite-almandine geobarometer and the staurolite problem revisited; *American Mineralogist*, 73, 20-47.

Jamieson, R.A., Tallman, P.C., Plint, H.E. and Conners, K.A., 1990. Regional geological setting of pre-Carboniferous mineral deposits in the western Cape Breton Highlands, Nova Scotia; *Geological Survey of Canada, Paper 90-8*, 77-100.

Kennedy, W.Q., 1949. Zones of progressive regional metamorphism in the Moine Schists of the Western Highlands of Scotland; *Geological Magazine*, 86, 43-56.

Keppie, J.D., 1989. $^{40}Ar/^{39}Ar$ mineral ages from Kellys Mountain, Cape Breton Island, Nova Scotia Implications for the tectonothermal evolution of the Avalon Composite Terrane; *Canadian Journal of Earth Sciences* 26, 1509-1516.

Keppie, J.D., Dallmeyer, R.D., and Krogh, T.E., 1992. U-Pb and $^{40}Ar/^{39}Ar$ mineral ages from Cape North, northern Cape Breton Island: implications for accretion of the Avalon Composite Terrane; *Canadian Journal of Earth Science*, 29, 277-295.

Kerrick, D.M., 1974. Review of metamorphic mixed volatile (H_2O-CO_2) equilibria; *American Mineralogist,* 59, 729-762.

Kohn, M.J. and Spear, F.S., 1991. Error propogation for barometers: 2. Applications to rocks; *American Minaralogist*, 76, 138-147.

Koziol, A.M., 1989. Recalibration of the garnet-plagioclase-Al_2SiO_5-quartz geobarometer and applications to natural parageneses; *EOS*, 70, 493.

Koziol, A.M., and Newton, R.C., 1988. Redetermination of the anorthite breakdown reaction and improvement of the plagioclase-garnet-Al_2SiO_5-quartz barometer;*American Mineralogist,* 73, 216-223.

Kretz, R., 1983. Symbols for rock-forming minerals; *American Mineralogist*, 68, 277-279.

LeMaitre, R.W., 1979. A new generalised petrological mixing model; *Contributions to Mineralogy and Petrology*, 71, 133-137.

Lin, S., van Staal, C.R. and Lee, C., 1993. The Harbour le Cou Group and its correlation with the Bay du Nord Group, southwestern Newfoundland; *in Current Research, Part D; Geological Survey of Canada, Paper 93-1D*, 57-64.

Lin, S., van Staal, C.R., Barr, S.M. and Chen Y., 1994a. Candidates for rocks of the Appalachian Central Mobile Belt in the Aspy Terrane of Cape Breton Island, Nova Scotia; *Atlantic Geoscience Society. annual meeting,* p. 34.

Lin, S., van Staal, C.R. and Dubé, B., 1994b. Promontory-promontory collision in the Canadian Appalachians; *Geology*, 22, 897-900.

Lowdon, J.A., Stockwell, C.H., Tipper, H.W., and Wanless, R.K., 1962. Age determinations and geological studies: *Geol. Survey of Canada Paper* 62-17, 140 p.

Ludwig, K.R., 1980. Calculation of uncertainties of U-Pb isotope data. *Earth and Planetary Science Letters*, 46, 212-220.

Ludwig, K.R., 1982. A computer program to convert raw U-Th-Pb isotope ratios to blank-corrected isotope ratios and concentrations with associated error correlations; *U.S. Geological Survey Open File Report* 82-820, 24 p.

Luth, W.D., Jahns, R.H. and Tuttle, O.F., 1964. The granite system at pressures of 4 to 10 kilobars. *Journal of Geophysical Research,* 69, 659-773.

Mattinson, J.M., 1986. Geochronology of high pressure-low temperature Franciscan metabasites: a new approach using the U-Pb system; *Geological Society of America Memoirs,* 164, 95-105.

Mezger, K., 1994. Sphene: a versatile mineral for high precision geochronology; *in Fall Meeting, American Geophysical Union* abstracts with programs, p 692.

Mezger, K., Rawnsley, C.M., Bohlen, S.R., and Hanson G.N., 1991. U-Pb garnet, sphene, monozite and rutile ages: implications for the duration of high-grade metamorphism and cooling histories, Adirondak Mts., New York; *Journal of Geology*, 99, 415-428.

Mezger, K., Essene, E.J., van der Pluijm, B.A., and Halliday A.N., 1993. U-Pb geochronology of the Glenville orogen of Ontario and New York: constraints on ancient crustal tectonics; *Contributions to Mineralogy and Petrology*, 114, 13-26.

Nance, R.D. and Dallmeyer, R.D.D., 1993. $^{40}Ar/^{39}Ar$ amphibole ages from the Kingston Complex, New Brunswick; evidence for Silurian-Devonian tectonothermal activity and implications for accretion of the Avalon composite terrane; *Journal of Geology*, 101, 375-388.

Newton, R.C., and Perkins, D. III., 1982. Thermodynamic calibration of geobarmeters based on the assemblages garnet-plagioclase-orthopyroxene (clinopyroxene)-quartz; *American Mineralogist*, 67, 203-222.

O'Brien, S.J., O'Brien, B.H. and Dunning, G.R., 1986. Geology of the central portion of the Hermitage Flexure area, Newfoundland; *Newfoundland Department of Miners and Energy Mineral Development Division, Report 86-1*, 189-208.

O'Brien, B.H., O'Brien, S.J., Dunning, G.R. and Tucker, R.D., 1993. Episodic reactivation of a late Precambrian mylonite zone on the Gondwana margin of the Appalachians, southern Newfoundland; *Tectonics*, 12, 1043-1055.

Paterson, S.R. and Tobisch, O.T., 1992. Rates of processes in magmatic arcs: implications for the timing and nature of pluton emplacement and wall rock deformation: *Journal of Structural Geology,* 14, 291-300.

Perchuk, L. L. 1991. Derivation of a thermodynamically consistent set of geothermometers and geobarometers for metamorphic and magmatic rocks. In Perchuk, L. L., ed. *Progress in metamorphic and magmatic petrology; a memorial volume in honor of D. S. Korzhinskiy*: University Press, Cambridge UK, 503p.

Perchuk, L.L. and Lavrent'eva, I.V., 1981. Experimental investigation of exchange equilibria in the system cordierite-garnet-biotite. In Saxena, S.K., ed. *Kinetics and Equilibrium in Mineral Reactions*; Springer Verlag, 199-240.

Phinney, W.C., 1963. Phase equilibria in the metamorphic rocks of St. Paul Island and Cape North, Nova Scotia; *Journal of Petrology,* 4, 90-130.

Plint, H.E. and Jamieson, R.A., 1989. Microstructure, metamorphism and tectonics of the western Cape Breton Highlands, Nova Scotia; *Journal of Metamorphic Geology,* 7, 407-424.

Powell, R., 1985. Regression diagnostics and robust regression in geothermometer/ geobarometer calibration: the garnet-clinopyroxene geothermometer revisited; *Journal of Metamorphic Geology*, 3, 231-243.

Powell, R. and Holland, T.J.B., 1988. An internally consistent thermodynamic dataset with uncertainties and correlations: 3. Applications to geobarometry, worked examples and a computer program; *Journal of Metamorphic Geology*, 6, 173-204.

Purdy, J. and Jäger, E., 1976. K-Ar ages on rock forming minerals from the Central Alps; *Memoirie degli Instituti di Geologia e Mineralogia dell'Universita di Padova*, 30, 1-31.

Reynolds, P.H., Jamieson, R.A., Barr, S.M. and Raeside, R.P., 1989. An $^{40}Ar/^{39}Ar$ study of the Cape Breton Highlands, Nova Scotia; thermal histories and tectonic implications; *Canadian Journal of Earth Sciences*, 26, 2081-2091.

Robins, G.A., 1972. Radiogenic argon diffusion in muscovite under hydrothermal conditions. M.S.c. thesis, Brown University, Providence, RI.

Rumble, D., 1978. Mineralogy, petrology, and oxygen isotope geochemistry of the Clough Formation, Black Mountain, western New Hampshire, USA, *Journal of Petrology,* 19, 317-340.

Selverstone, J., Spear, F.S., Franz, G. and Morteani, G., 1984. High-pressure metamorphism in the SW Tauern Window, Austria: P-T paths from hornblende-kyanite-staurolite schists, *Journal of Petrology*, 25, 501-531.

Sevigny, J.H. and Hanson, G.N., 1993. Orogenic evolution of the New England Appalachians of southwestern Connecticut; *Geological Society of Americal Bulletin*, 105, 1591-1605.

Schumacher, J., 1991. Empirical ferric iron corrections: necessity, assumptions, and effects on selected geothermobarometers; *Mineralogical Magazine*, 55, 3-18.

Soper, N.S. and Woodcock, N.H., 1990. Silurian collision and sediment dispersal patterns in southern Britain; *Geological Magazine*, 127, 527-542.

Soper, N.J. and Hutton, D.H.W., 1984. Late Caledonian sinistral displacements in Britain; implications for a three-plate collision model; *Tectonics*, 3, 781-794.

Spear, F.S. and Cheney, J.T., 1989. A petrogenetic grid for pelitic schists in the system SiO_2-Al_2O_3-FeO-MgO-K_2O-H_2O. *Contributions to Mineralogy and Petrology*, 101, 149-164.

Thompson, A.B., 1982. Dehydration melting of pelitic rocks and the generation of H_2O-undersaturated granitic liquids. *American Journal of Science*, 282, 1567-95.

Thompson, A.B., 1976. Mineral reactions in pelitic rocks: I. Prediction of P- T-X (Fe-Mg) phase relations. *American Journal of Science,* 276, 401-424.

Thompson, A.B. and Tracy, R.J., 1979. Model systems for anatexis of pelitic rocks. II. Facies series melting and reactions in the system CaO-$KAlO_2$-$NaAlO_2$-Al_2O_3-SiO_2-H_2O. *Contributions to Mineralogy and Petrology*, 70, 429-438.

Thompson, J.B., 1957. The graphical analysis of mineral assemblages in pelitic schists. *American Mineralogist*, 42,842-858.

Thompson, P.H. and Leclair, A.D., 1987. Chloritoid-hornblende assemblages in quartz-muscovite pelitic rocks of the Central Metasedimentary Belt, Grenville Province, Canada, *Journal of Metamorphic Geology*, 5, 415-436.

Thompson, A.B. and Tracy, R.J., 1979. Model systems for anatexis of pelitic rocks. II. Facies series melting and reactions in the system CaO-$KAlO_2$-$NaAl_2$-Al_2O_3-SiO_2-H_2O; *Contributions to Mineralogy and Petrology*, 70, 429-438.

Tilton, G. RT., 1973. Isotopic lead ages of chondritic meteorites; *Earth and Planetary Science Letters*, 19, 321-329.

Van Gool, J.A.M. and Cawood, P.A., 1994. Frontal vs. basal accretion and contrasting particle paths in metamorphic belts; *Geology*, 22, 51-54.

Van Staal, C.R., 1987. Tectonic setting of the Tetagouche Group in northern New Brunswick: implications for plate tectonic models of the northern Appalachians. *Canadian Journal of Earth Sciences*, 24, 1329-1351.

Van Staal, C.R., 1994. Brunswick subduction complex in the Canadian Appalachians: Record of the late Ordovician to late Silurian collision between Laurentia and the Gander margin of Avalon; *Tectonics*, in press.

Van Staal, C.R. and Fyffe, L.R., 1991. Dunnage and Gander Zones, New Brunswick:Canadian Appalachian Region: *New Brunswick Natural Resources and Energy Geoscience Report 91-2*, 39p.

Van Staal, C.R. and Williams, H., 1991. Dunnage Zone-Gander Zone relationships in the Canadian Appalachians; *in GSA Northeastern Section/Southeastern Section joint meeting*, abstracts with program, 23, 143.

Van Staal, C.R., Winchester, J.A., Brown, M. and Burgess, J.L., 1992a. A reconnaissance geotraverse through southwestern Newfoundland. *in Current Research, Part D; GeologicalSurvey of Canada, Paper 92-1D*, 133-143.

Van Staal, C.R, Burgess, J.L., Lee, C., Lin, S. and Schofield, D., 1992b. Geology of the Port aux Basques-Rose Blanch area (NTS 11-0/10 & 11-0/11. *Report of Activities, Geological Survey Branch of Mines and Energy Government of Newfoundland and Labrador*, 41-43.

Vernon, R.H., 1987. Growth and concentration of fibrous sillimanite related heterogeneous deformation in K-feldspar-sillimanite metapelites. *Journal of Metamorphic Geology*, 5, 51-68.

Vernon, R.H., 1975. Microstructures of high-grade metamorphic rocks at Broken Hill, Australia. *Journal of Petrology*, 9, 1-22.

Vielzeuf, D. and Holloway, J.R., 1988. Experimental determination of the fluid-absent melting relations in the pelitic system, *Contributions to Mineralogy and Petrology*, 98, 257-276.

Vielzeuf, D. and Holloway, J.R., 1988. Experimental determination of the fluid-absent melting relations in the pelitic system; *Contributions to Mineralogy and Petrology*, 98, 257-276.

Wanless, R.K., Stevens, R.D., Lachance, G.R. and Rimsaite, R.Y.H., 1965. Age determinations and geological studies: Geol. Survey of Canada Paper 64-17, 126 p.

Williams, H., 1970. The Hermitage Flexure, the Cabot Fault and the disappearance of the Newfoundland Central Mobile Belt: *Geological Society of America Bulletin*, 81, 1563-1568.

Williams, H., 1979. Appalachian Orogen in Canada, *Canadian Journal of Earth Science*, 14, 987-1003.

Williams, H., Colman-Sadd, S.P., and Swindon, H.S., 1988. Tectonic-stratigraphic subdivisions of central Newfoundland; *in Current Research, Part B, Geological Survey of Canada, Paper 88-1B*, 91-98.

Wilton, D.H.C., 1983. The geology and structural history of the Cape Ray fault zone in southwester Newfoundland: *Canadian Journal of Earth Science*, 20, 1119-1133.

Yardley, B.W.D., 1989. An introduction to metamorphic petrology. *Longman Scientific and Technical Group*, Essex, England.